Study and Control of turbulent transport in the Boundary Plasma region of the TJ-II stellarator and the JET tokamak

Ulises Losada Rodríguez

Licenciado en Física

en cumplimiento parcial de los requisitos para el grado de Doctor en

Plasmas y Fusión Nuclear

Universidad Carlos III de Madrid

Directores:

Dr. Carlos Hidalgo Vera

Dr. Eduardo de la Cal Heusch

Tutor:

Dr. Luis García Gonzalo

Marzo de 2019

GOBIERNO DE ESPAÑA MINISTERIO DE CIENCIA, INNOVACIÓN Y UNIVERSIDADES

Laboratorio Nacional de Fusión Ciemat

Infraestructuras Científicas y Técnicas Singulares

UNIÓN EUROPEA
Fondo Europeo de Desarrollo Regional

Dedico este trabajo a mi familia.

Cuando creíamos que teníamos todas las respuestas, de pronto, cambiaron todas las preguntas

Mario Benedetti

Hay gente que porque sabe leer y escribir, cree que sabe leer y escribir

Poeta Reinaldo Arenas

CONTENTS

Acknowledgements/Agradecimentos

Este trabajo se ha realizado en el marco del proyecto ENE2012-38620-C02-01 (referencia BES-2013-065215), del Ministerio de Ciencia, Innovación y Universidades (MICINN). Agradezco encarecidamente al MICINN, al Instituto Nacional de Empleo (INEM), y por ende al Reino de España, por concederme el privilegio de disfrutar de un contrato predoctoral financiado durante el período 2014 – 2018, que me ha permitido realizar los estudios de doctorado, accediendo a un nivel de formación profesional y de crecimiento personal que, bajo cualquier otra circunstancia, habrían sido inalcanzables para mí.

Agradezco profundamente al Laboratorio Nacional de Fusión y al Centro de Investigaciones Energéticas, Medioambientales y Tecnológicas (Ciemat) por haberme acogido y puesto a mi disposición tanto las herramientas físicas y el conocimiento necesario para llevar a cabo mi trabajo, así como por la labor de ayuda prestada por mis compañeros en todo momento y su actitud positiva y constructiva hacia mí y hacia mi trabajo.

Estoy especialmente agradecido al Dr. Carlos Hidalgo Vera, director de esta tesis doctoral. Tanto por su guía y sus enseñanzas sobre física de plasmas como por su apoyo constante en los ámbitos personal y profesional, así como por su persuasión hasta el último día de trabajo y por su pasión por el trabajo científico y la puesta en práctica de la investigación de ideas innovadoras, pasión que comparto estrechamente. Especialmente por su confianza en mí desde el primer momento y hasta hoy, así como por su constante atención tanto personal como profesional. Así mismo, al Dr. Eduardo de la Cal, que me ha ayudado a entender una parte importantísima de la física de plasmas, y a quién considero un científico de primer nivel y una persona honesta y confiable en el terreno personal. Con especial cariño y agradecimiento recuerdo mi estancia en JET (Oxford), que tiene un valor altísimo profesionalmente para mí y que fue posible gracias a la confianza depositada en mí por ambos. Especial recuerdo guardo también de María Ángeles Pedrosa y Arturo Alonso, quienes me enseñaron, durante mis dos primeros años, todo lo referente a la interpretación de datos y operación de sondas de Langmuir, junto con Boudewijn van Milligen, con su ayuda inestimable en el análisis de datos.

Finalmente, me siento complacido por haber compartido con mis compañeros de trabajo científico, especialmente Gregorio Martín, Lolo, Raúl, Nerea, Adriana, Fran, Alfonso de Castro, Raul Gerrú, François, Álvaro Cappa, Alfonso Ros, Jose, Marian, Mamen, Ignacio, Bernardo Zurro, etc.

I would like to show my warmest gratitude to Dr. Bing Liu, in whom I have seen a great professional and a very humble person. I will never forget the time we spent together learning from each other. I am happy to have met Ridhima Sharma, Gustavo Grenfell, Ting Wu and Philip Khavanov, who are now my friends. I also appreciate the opportunity that was given to me to interact with undergraduate and Master students: François Guilleaotot and Raúl Gerrú, who contributed to my own expertise and to this PhD thesis.

Finally, I have to thank Prof. Tsviako Popov for his lessons on Langmuir Probe theory and Dr. Alexander V. Melnikov for his contribution to my knowledge about plasma potential profiles. I was lucky to have known Alexander Zhezhera, who is not with us and Dr. Ludmila Krupnik, Leonid Eliseev, Alexander Kozachek, Vitaly Zenin and Mikola Dreval, from the Ukraine Academy of Sciences and from Kurchatov Institute (Russian Federation).

It was a tremendous pleasure to work with Dr. Alexander Huber, at JET as well as with Valentina and Gennady Sergienko. I thank also my partners from IPP-Greifswald, Adrian, Arturo, Mathias, Francesco, Andrea, Tulio, Priyangena, etc.

Finalmente, gracias a todos los amigos que hice durante mi doctorado: Luis Esteban, Alvaró, Luis Alfonso, Fernando Martín, Grego, Alfonso de Castro, José Luis de Pablos y a toda la gente que me apoyó: mis amigos Eric, Patricio, Antonio González y Carlos Raúl. También Marga, Teresita, Idelsa, Isabel, etc. Gracias a Karen Velázquez por haber sido una cercana compañía en mi vida y en los momentos finales de esta tesis. Especialmente gracias una persona que es como mi hermano de sangre, Juan Carlos Arias Valdes.

Pero sobre todo, gracias á miña familia, meus pais, Ramón e Pura, o meu irmau Jorge, os meus avós Manolo, Celeste, Avelino e Pura. Os meus bisavós Eudosia e José. As miñas tías Avelina, Manuela, María, meu tío Pepe e meus primos Brais e María. Meus tíos Amaro e Carmen. Gardo un espacio privilexiado para os meus amigos de sempre de Cenlle: Dani e Diego, por quenes teño un profundo amor e respecto, xa que non tuveron as mesmas oportunidades que min nin unha vida tan sinxela. Gracias a todas esas persoas que conocín xogando ó fútbol en Galicia, especialmente a Manuel Iglesias (Fleitas), así como a Marcos, Borja, Miguel Freire, Fran, Hugo García, entre outros. Gracias a Carolina Méndez, por ser unha persoa tan importante para min e por apoiarme desde o principio, habendo estado ó meu lado durante os momentos críticos.

Non podo esquecerme dos meus compañeiros da Universidade de Vigo, que me acompañaron durante a Licenciatura en Física, por 5 anos. Especial recordo teño para Javi, Hugo e Miguel. Imposible sería esquecer todo o tempo que pasamos xuntos estudanto Física e apoiándonos, que acabou resultando en sendos fermosos percorridos profesionais no ámbito da física. Esta tesis tamén vai adicada a eles, así como a os meus profesores durante o pre-universitario, Margarita Aller, Alberto Viso, Jorge Casalderrei e Aurelio.

Tambem para as pessoas especiais que estão agora no belo país de São Tomé e Principe.

Para todos eles e outros companheiros com quem naveguei pelos mares mais bravos e dos quais extraí as mais valiosas sabedorias, este trabalho é dedicado. Moito Obrigado.

Abstract

Thermonuclear fusion has been proposed as a sustainable, clean and safe energy source to meet the energy demands of the future. There are, however, still several challenges that need to be overcome in order to realize a viable fusion power plant. One of the great challenges is the integration of physics and technology optimization.

Performance of magnetic fusion reactors is limited by heat and particle losses. The heat and particle losses are understood to be governed by the non-linear interplay of turbulence and plasma flows but uncertainty remains on e.g. physics of the sudden transitions between confinement regimes, isotopic scaling of confinement, non-linear saturation mechanisms of plasma turbulence, power exhausts and plasma-wall interaction.

This thesis investigates the interplay of flows and turbulence in the TJ-II stellarator and the influence of magnetic configuration on plasma-wall interaction in the JET tokamak.

A deep understanding of the mechanisms leading to turbulence self-regulation via Zonal Flows (ZFs) is of paramount importance. In this sense, the assessment of Long Range Correlations (LRC) in the plasma edge, by the use of Langmuir probe systems, have been proven to be a powerful strategy to study the interaction between ZFs and turbulence. Improvements in the experimental strategy to characterize LRC have been applied to study the interplay between neoclassical radial electric fields and ZFs and the transition to improved confinement regimes in the TJ-II stellarator.

Experimental studies reveal the role of neoclassical radial electric fields to control the amplitude of Zonal Flows resulting in the development of both long (neoclassical) and short (due to Zonal Flows) radial electric field scales with important implication in the physics understanding of transport self-regulation mechanisms. A comprehensive description of the influence of plasma scenarios on the radial width of ZFs is given here, with a special focus on its dependence with heating and isotope scaling.

For the first time, the characterization of low frequency fluctuating ZFs and mean radial electric fields has been experimentally studied during the L-H transition in Hydrogen and Deuterium plasmas in the stellarator TJ-II. No evidence of isotope effect on the L-H transition dynamics was observed. These observations emphasize the critical role of both zero frequency (equilibrium) and low frequency varying large-scale flows for stabilizing turbulence during the triggering of the L-H transition in magnetically confined toroidal plasmas and show that there are different paths to reach the L-H transition with impact on the conditions to access the H-mode regime.

In addition to the relevance of studies carried out in stellarators, experimental validation of relevant plasma scenarios in large tokamaks constitute the fundamental test bench for future

burning fusion reactors such as ITER. For example in the last years it has been shown that, in the JET tokamak, with the new ITER-like wall, global plasma confinement is strongly linked to the divertor magnetic topology, which influences the Boundary Plasma and the Plasma Wall Interaction. In this Thesis we show a study on how the neutral fluxes are affected by the divertor magnetic configuration and, as a consequence, how the SOL plasma changes. We also present a detailed preliminary analysis of the dynamic behavior of Ion and Neutral fluxes during the ELM-cycle. The results point to the Recycling coefficient, which varies significantly within this short time-scale, something that could have important implications in the understanding of the H-mode performance.

Resumen

El aprovechamiento de la energía de la fusión termonuclear se ha propuesto como un método limpio y sostenible para hacer frente a las demandas energéticas futuras. Sin embargo, actualmente todavía se deben superar retos científicos y técnicos para hacer viable la operación de un reactor nuclear de fusión. Uno de los mayores retos es el entendimiento de la física del plasma que tiene lugar en los reactores de fusión así como la optimización tecnológica de los propios reactores.

El rendimiento de los futuros reactores de fusión está limitado por las pérdidas de partículas y de calor. Ambos fenómenos están gobernados por la interacción no lineal entre la turbulencia del plasma y los flujos a gran escala, conocidos como Flujos Zonales. Por otra parte, la física de las transiciones espontáneas entre regímenes de diferente nivel de confinamiento, el efecto isotópico y sus implicaciones, los mecanismos de saturación no lineal de la turbulencia así como la evacuación de los flujos de calor y la física de la interacción entre el plasma y la pared necesita todavía ser entendida.

Esta tesis describe la investigación empírica de la interacción entre las diferentes escalas de turbulencia de plasma en el stellarator TJ-II y la influencia de la configuración magnética en la física de la interacción plasma-pared en el tokamak JET. A este efecto, se han utilizado dos diagnósticos: las sondas electrostáticas (conocidas como sondas de Langmuir) y espectroscopía rápida en el espectro visible.

Es de suma importancia la comprensión profunda de los mecanismos que conducen a la autorregulación de la turbulencia por la acción de los Flujos Zonales (ZF). En este sentido, se ha demostrado que la evaluación de las correlaciones de largo alcance (LRC) en el borde del plasma, mediante el uso de los sistemas de sondas de Langmuir, es una estrategia poderosa para estudiar la interacción entre ZF y la turbulencia. Las mejoras en la estrategia experimental para caracterizar LRC se han aplicado para estudiar la interacción entre los campos eléctricos radiales neoclásicos ZF durante la transición a regímenes de confinamiento mejorados en el stellarator TJ-II.

Los estudios experimentales llevados a cabo revelan el papel de los campos eléctricos radiales neoclásicos en el control de la amplitud de los flujos zonales que resultan en el desarrollo de escalas de campos eléctricos radiales largos (neoclásicos) y cortos (debidos a los flujos zonales), con una importante implicación en la comprensión física de los mecanismos de auto-regulación transporte radial. Aquí se proporciona una descripción completa de la influencia de los escenarios de plasma en el ancho radial de las ZF, con un enfoque especial en su dependencia con el calentamiento y la masa isotópica.

Por primera vez, la caracterización de estas fluctuaciones globales de baja frecuencia y campos eléctricos radiales se ha estudiado experimentalmente durante la transición L-H en plasmas de hidrógeno y deuterio en el stellarador TJ-II. No se observó evidencia de efecto isótopo en la

dinámica de transición L-H. Estas observaciones enfatizan el papel crítico del campo eléctrico neoclásico (o de equilibrio) y los flujos a gran escala de baja frecuencia para estabilizar la turbulencia durante el inicio de la transición L-H en plasmas toroidales confinados magnéticamente. Esto muestra que existen diferentes caminos para alcanzar la transición de LH con impacto sobre las condiciones de acceso al régimen de confinamiento mejorado.

Además de la relevancia de los estudios realizados en stellarators, la validación experimental de escenarios relevantes de plasma en grandes tokamaks constituye el banco de pruebas fundamental para futuros reactores de fusión como ITER. Por ejemplo, en los últimos años se ha demostrado que, en el tokamak JET, con la nueva pared, que es idéntica a la que estará instalada en ITER, el confinamiento global del plasma está fuertemente vinculado a la topología del divertor, lo que influye en la física y en las características del borde del plasma y de la interacción plasma-pared. En esta tesis, mostramos un estudio sobre cómo los flujos de partículas neutras se ven afectados por la configuración magnética del divertor y, en consecuencia, cómo cambia la parte más externa del plasma, en la que las líneas de campo no están cerradas sobre sí mismas, sino que se cierran a través de los elementos metálicos del dispositivo, conocida como “Scrape-Off Layer”. También presentamos un análisis preliminar detallado del comportamiento dinámico de los flujos de iones y neutros durante las inestabilidades de tipo ELM. Los resultados apuntan al coeficiente de reciclado, que varía significativamente dentro de esta breve escala de tiempo, algo que podría tener implicaciones importantes en la comprensión del rendimiento en modo de alto confinamiento.

Published & Submitted Content

Articles or other contributions (co)-authored by the Doctoral candidate that are included as part of the thesis and that have been published:

- U. Losada, A. Alonso, B. Ph. van Milligen, C. Hidalgo, B. Liu, M. A. Pedrosa, C. Silva and the TJ-II team (2016) *Influence of long-scale length radial electric field components on zonal-flow like structures in the TJ-II stellarator*. Plasma Physics and Controlled Fusion **58**, 084005
  https://doi.org/10.1088/0741-3335/58/8/084005
  This item is partly included in Chapter III and is also mentioned in the introduction of the section III.1. The material from this source that is included in this thesis has not been signed out with typographic means; appropriate references are made. Reproduced with permission of the copyright owner: *Institute of Physics.*

- U. Losada, T. Estrada, B. Liu, B. Ph. van Milligen, J. Cheng, C. Silva, I. Pastor, J. M. Fontdecaba, C. Hidalgo and the TJ-II team (2018) *Role of isotope mass and evidence of fluctuating zonal flows during the L–H transition in the TJ-II stellarator*. Plasma Physics and Controlled Fusion **60**, 074002
  https://doi.org/10.1088/1361-6587/aac069
  This item is partly included in Chapter III and is also mentioned in the introduction of the section III.2. The material from this source that is included in this thesis has not been signed out with typographic means; appropriate references are made. Reproduced with permission of the copyright owner: *Institute of Physics.*

- T. Kobayashi, U. Losada, B. Liu, T. Estrada, B. Ph. van Milligen, R. Gerrú, M. Sasaki and C. Hidalgo (2018) *Frequency and plasma condition dependent spatial structure of low frequency global potential oscillations in TJ-II stellarator.* Nuclear Fusion 2019 (in press)
  https://doi.org/10.1088/1741-4326/ab0122
  This item is partly included in Chapter III and is also mentioned in the introduction of the section III.3. The material from this source that is included in this thesis has not been signed out with typographic means; appropriate references are made. Reproduced with permission of the copyright owner: *Institute of Physics.*

Other Research Merits

Articles or other contributions (co)-authored by the Doctoral candidate that are not included in this thesis:

- B. Liu, C. Silva, H. Figueiredo, M. A. Pedrosa, B. Ph. van Milligen, T. Pereira, U. Losada, and C. Hidalgo (2016) *Multi-scale study of the isotope effect in ISTTOK* Nuclear Fusion **56**, 056012

- B. Ph. van Milligen, J. H. Nicolau, B. Liu, G. Grenfell, U. Losada, C. Hidalgo and the TJ-team (2018) *Filaments in the edge confinement region of TJ-II* Nuclear Fusion **58**, 026030

- G. Grenfell, B. Ph. van Milligen, U. Losada, T. Wu, B. Liu, C. Silva, M. Spolaore and C. Hidalgo (2018) *Measurement and control of turbulence spreading in the Scrape-Off Layer of TJ-II* Nuclear Fusion **59** 016018

- S. Wiesen, S. Brezinsek, M. Wischmeier, E. de la Luna, M. Groth, A. E. Jaervinen, E. de la Cal, U. Losada, A. M. de Aguilera, L. Frassinetti, Y. Gao, C. Guillemaut, D. Harting, A. Meigs, K. Schmid, G. Sergienko and JET contributors (2017) *Impact of the JET ITER-like wall on H-mode plasma fueling* Nuclear Fusion **57** 066024

- X. Litaudon et al. (2017) *Overview of the JET results in support to ITER* Nuclear Fusion **57** 102001

- F. Castejón et al. (2017) *3D effects on transport and plasma control in the TJ-II stellarator Nuclear Fusion* **57** (10)

- U. Losada, B. A. Carreras, B. Ph. van Milligen, A. Alonso, E. Sánchez, B. Liu, J. Cheng, L. García, C. Silva C. Hidalgo and the TJ-II team *Experimental study of the relation between neoclassical and turbulent mechanisms in stellarators* Congress: 43rd Conference on Plasma Physics **Poster presentation** Leuven, Belgium, (2016) 2/10 July

- U. Losada, S. Oshima, F. Guilleaotot, B. Zurro, B. López, B. van Milligen, C. Hidalgo and the TJ-II team *Characterization of Zonal Flows in the TJ-II stellarator: Role of plasma heating, NC radial electric field and ion mass* Congress: 21st International Stellaror Helliotron Workshop, **Poster presentation** Kioto, Japan, (2017) 2/8 October

- U. Losada, T. Estrada, B. Liu, B. van Milligen, J. Cheng, I. Pastor, J. M. Fontdecaba, C. Hidalgo and the TJ-II team *Evidence of fluctuating Zonal Flows during the L-H transition and role of isotope mass in the TJ-II stellarator* Congress: 21st International Stellaror Helliotron Workshop, **Oral presentation** Kioto, Japan, (2017) 2/8 October

- U. Losada, T. Estrada, B. Liu, B. van Milligen, A. Alonso, J. Cheng, I. Pastor, J. M. Fontdecaba, C. Hidalgo and the TJ-II team *L-H transition and isotope effect in TJ-II: role of pressure gradients and Zonal Flows* Coordinated Group Work Meeting on turbulence and H-mode: **Oral presentation** Madrid, January 2017

- U. Losada and TJ-II team *Uso de sondas electrostáticas en el estudio de Plasmas para fusión nuclear* Jornadas de jóvenes investigadores en Física atómica y molecular **Oral presentation** Barcelona, April 2018

List of figures

List of tables

NOMENCLATURE and SYMBOLS

a: Minor radius.

ADAS: Atomic Data and Analysis Structure.

B: Magnetic field.

CCD: Charged Coupled Device.

DAI3: Label for the spectroscopic line looking at the JET divertor tile I.

DRS: Doppler reflectometry system.

E_r: Radial electric field.

ELM: Edge Localized Mode.

ECRH: Electron Cyclotron Resonance Heating.

I_p: Plasma current

I_{sat}: Ion saturation current.

GAM: Geodesic Acoustic Mode

HFS: High Field Side.

ILW: ITER-Like Wall.

II: Image intensifier.

ISP: Inner Strike Point.

JET: Joint European Torus.

JPN: Jet Pulse Number.

LCFS: Last Closed Flux surface.

LCO: Limit Cycle Oscillation.

L^{D_α}: Visible emission radiance.

LP: Langmuir probes.

LRC: Long Range Correlation.

LR-coherence: Long Range Coherence.

L_r: Radial correlation length of turbulence.

LFS: Low Field Side

NBI: Neutral Beam Injection.

n_e: Electron density.

ρ: Normalized minor plasma radius.

SOL: Scrape-Off Layer

SP: Strike point.

S/XB: Atomic physics factor

T_e: Electron temperature.

T_i: Ion temperature.

τ_e: Energy confinement time.

TJ-II: T-J-II stellarator.

V_f: Floating potential.

ZF: Zonal Flow.

Φ_f: Floating potential.

CONTENTS

I. INTRODUCTION

I.1. General motivation: Fusion at the energy crossroad

At the beginning of the 21st century the population of the planet Earth has increased until reaching the number of more than 7 thousand millions people [1]. Population level is estimated to reach 9 billion people for the end of this century [2]. We are facing an energy transition phase driven by climate change and globalization. Consequently, a huge effort is being made in search for energy production, conversion, distribution and saving technologies with the aim of protecting the security of energy supply.

Both the generation and consumption of energy have a strong impact on the environment in all its stages, from its extraction to its use, being the effects on climate change its most disturbing threat. Climate change is related to the increase in the proportion of green-house gases in the atmosphere. The most important green-house gas is Carbon Dioxide (CO_2), which results from burning fossil fuels to produce energy. Then, the energy transition is proposed as the promotion of an energy system that does not depend on a predominantly fossil source. In 2015, during the United Nations Conference on Climate Change (Paris) an important agreement was reached seeking to limit global CO_2 emissions with the aim of preventing Earth's temperature to exceed two degrees Celsius with respect to the pre-industrial temperature.

On the other hand, the level of energy and resources consumption per capita presents a high level of inequalities worldwide [3] (including primary energy consumption [4, 5] and importation of energy resources [6]). The amount of energy consumed in developing countries is considerably lower than the quantity of energy consumed by developed countries [7, 8]. Also the type of consumed energy in the poorest societies is hazardous [9, 10, 11]. Nonetheless, in the last 30 years, the globalization of the world economy has led to a less unequal distribution of the consumed energy due to the global interchange of work and resources. The cumulative distribution of CO_2 emissions follows the same exponential feature as the relation Energy/population per country [12]. At the present, around 1.5 billion people do not have access to electricity and around 3 billion people use biomass for basic needs. In addition, the connection between energy sources and climate change has strong political, social and ethical consequences: accepting the necessity of energy to sustain the imposed economic growing, access to energy should be considered as a human right. Assuming also the impossibility of extending the energy consumption model of developed countries to developing countries (fig. 1.1), the former have a clear responsibility in the development model of the later.

Our society is based on the paradigm of a continuously growing model, which is only possible because it is sustained by a global worldwide economic system, reinforced by a political structure [13] and fed by the harnessing of natural resources. It requires a huge and increasing amount of available energy sources which leads to the generation of wastes. In addition, the increasingly high energetic and economic costs of primary energy extraction processes from natural resources augment the society´s physical dependence on the nature [14]. This inevitably compromises the future energetic performance and economical profitability of accessing primary energy sources in an equitable way for all the Earth inhabitants [14].

The previously explained facts have taken our society to the search for new strategies on electrical energy production and storage in order to keep economical growing in a cleaner and still profitable way. However, the mentioned concerns and contradictions on the sustainability of the current imposed economic growing paradigm should make us to consider new alternatives such as reduction in the level of consumption as important as the search for new forms of energy [15, 16] in order to protect people and Earth.

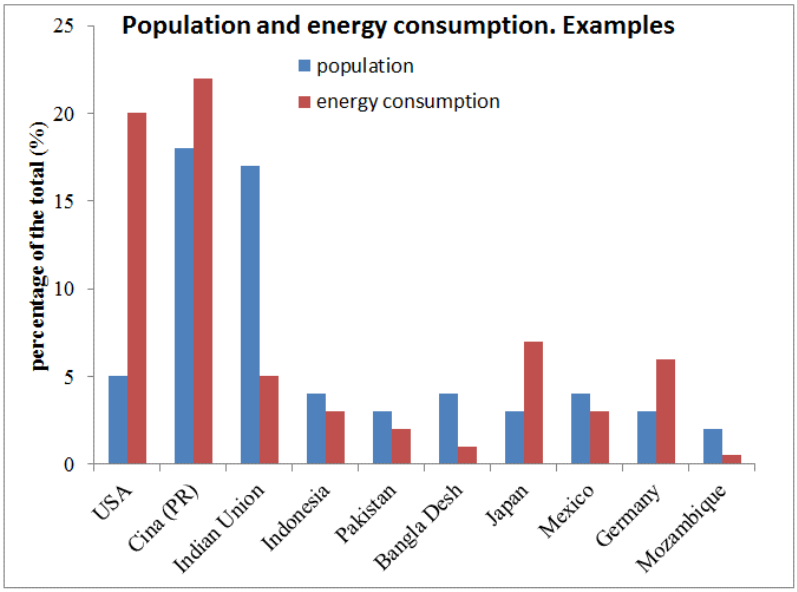

Figure 1.1 The figure shows comparison of the ratio between the population and the energy consumption for different countries.

Renewable energy is the energy obtained from virtually inexhaustible natural sources, either because of the immense amount of energy they contain or because they are capable of regeneration by natural means. Among others, the most important renewable energies are solar (which uses electromagnetic radiation from the sun) and wind (obtained from the wind). Of more limited importance are, among others, hydroelectric (which uses the potential and kinetic energy of water currents) and biomass (which uses organic matter). Pending challenges in the

field of renewable energy are the development of storage systems (hydrogen, chemical storage, hydraulic energy) and the optimization of intelligent distribution networks [17, 18]. Renewable energies are spread over wide areas and countries [19] and its cost is continuously dropping [20]. Given the challenges posed by nuclear fission energy, we can ask ourselves some questions about the technical feasibility of the process, the social acceptability of this energy and the management of the generated wastes.

The pending challenges in the transformation of fossil fuel-based energies include several aspects such as the development of strategies to reduce emissions from fossil fuel plants and the implementation of strategies to sequester CO2 emissions and improve energy efficiency [21, 22, 23].

The fusion reactions are those that release the energy that feeds the sun and the stars. For fusion to occur, nuclei must overcome the electrostatic repulsion and get close enough to allow the attractive nuclear force to come into play. The international scientific community works on different alternatives (inertial and magnetic confinement), with different degrees of development, towards the practical realization of fusion energy. In the case of the strategy based on magnetic confinement, it is required to heat the reactive nuclei at temperatures 15 times greater than the center of the Sun (estimated at around 15 million degrees) and thermally isolate them from the surrounding environment by means of an intense magnetic field (of the order of 5-7 T, that is, about 100,000 times the Earth's magnetic field). Matter at these extreme temperatures consists of a highly ionized gas called plasma. The realization of viable nuclear fusion energy requires solutions for a series of scientific and technological problems of enormous magnitude as described in the EU Fusion Roadmap [24].

The main pending challenges in nuclear fusion include the integration and optimization of physics and technology criteria. From the point of view of plasma physics it is required to efficiently confine a plasma in ignition; that is, reactive enough to produce substantially more energy than that consumed in the plasma generation process. From the technological point of view, it is necessary to demonstrate self-sufficiency in the generation of tritium and to develop materials that are resistant to the intense and very energetic nuclear fusion neutron fluxes.

I.2.Nuclear Fusion plasmas

I.2.1. Principles of Nuclear Fusion

There are nuclear binding forces that keep together the subatomic particles in the atom [25]. Figure 1.2 shows the average binding energy as a function of mass number for different elements. The lightest and heaviest nuclei have lower average binding energy. The energy can be obtained by dividing heavy nucleus (fission) or by joining light nuclei (fusion). The union of two protons (p - p) is the most common fusion reaction that takes place in the stars, leading

to the conversion of Hydrogen into Helium [26]. The global balance of *p-p* process is equivalent to join four protons to create an atom of Helium-4 (^4_2He), as described in the expression (1.1).

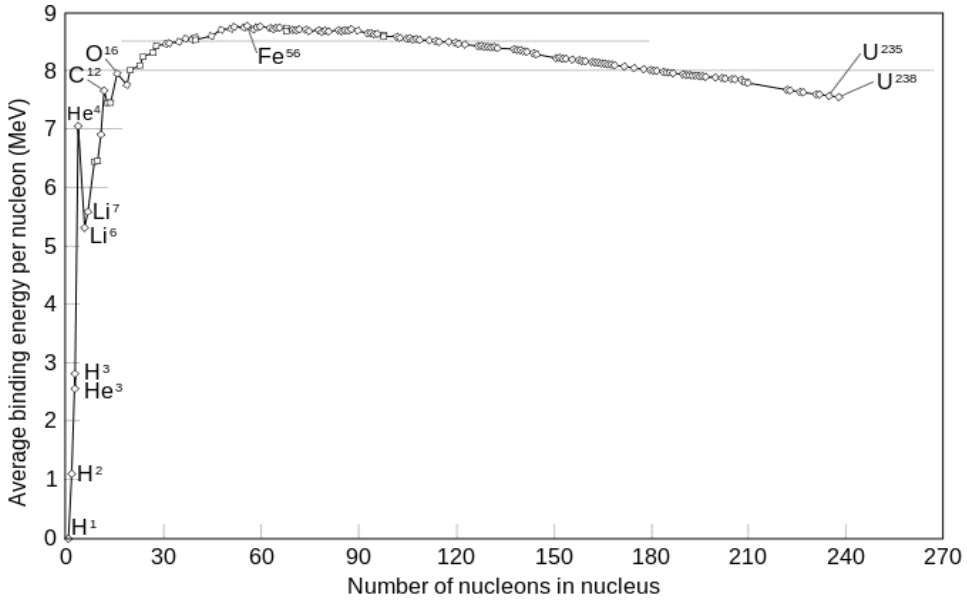

Figure 1.2 This figure shows the nuclear binding energy for different elements. Source: Wikipedia.

$$\left.\begin{array}{l} p + p \rightarrow {}^2_1D + e^+ + \nu_e \\ 4p \rightarrow {}^4_2He + 2e^+ + 2\nu_e + \gamma \\ {}^3_2He + {}^3_2He \rightarrow {}^4_2He + 2p \end{array}\right\} \quad (1.1)$$

where p represents proton, ^2_1D the Deuteron (heavy isotope of Hydrogen), ^3_2He and ^4_2He are isotopes of Helium, γ is a high energy photon, e^+ is a positron and ν_e represents the neutrino. Following the Einstein relation, $E = mc^2$, the difference in mass (m) is liberated in form of energy. After some indications, the first experimental observation of p-p neutrinos was obtained in 1992 [27].

On Earth, the most convenient reaction, due to its high cross-section at achievable temperatures, is the D-T reaction [28], shown in figure 1.3. In the reaction (equation 1.2) is described how an amount of 17.58 MeV are released in the D-T reaction, 14.06 MeV of which linked to the neutron as kinetic energy:

$$^2_1D + {}^3_1T \rightarrow {}^4_2He(+3.52\ MeV) + {}^1_0n(+14.06\ MeV) \quad (1.2)$$

While the Deuterium is an abundant and stable element in the Earth (30 grams per cubical meter of water), tritium is a radioactive isotope with half-life in the order of 12 years and therefore it is not present in the nature, which means that it should be produced by artificial means [29, 30]. It is possible also to obtain Tritium from Lithium:

$$^{1}_{0}n + {}^{6}_{3}Li \rightarrow {}^{3}_{1}T + {}^{4}_{2}He \qquad (+4.80\ MeV) \tag{1.3}$$
$$^{1}_{0}n + {}^{7}_{3}Li \rightarrow {}^{3}_{1}T + {}^{4}_{2}He + {}^{1}_{0}n \qquad (-2.47\ MeV) \tag{1.4}$$

where (1.4) is typical for the case of thermal neutrons and (1.5) has a high cross section for fast neutrons [31]. Lithium is found in nature (7.5 % of $^{6}_{3}Li$ and 92.5% of $^{7}_{3}Li$). Then, the neutrons produced on the fusion reaction can be used to produce more tritium in situ.

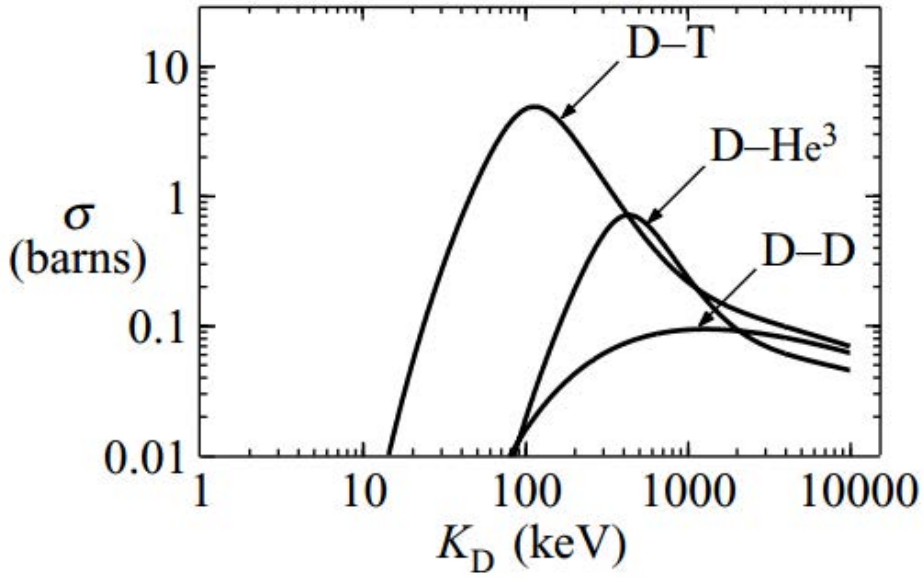

Figure 1.3 Cross-section for different nuclear fusion reactions. As seen in the figure, the most probable reaction is the one by which Tritium and Deuterium are joint.

In the stars, with temperatures in the order of $10^7\ K$ and densities of about $10^{30}\ particles/m^3$, the time of the reaction (1.1) is of about 10^7 years. This reaction rhythm is very slow but is enough to sustain the stars due to the high quantity of Hydrogen stored in its nucleus and to the huge amount of energy released [32].

In order for a fusion power plant to be viable, it needs to produce more energy than it consumes. A criterion for such a power producing fusion reactor was derived by Lawson [33]:

$$nT\tau_E > 5 \cdot 10^{21} m^{-3} keVs \tag{1.5}$$

What this triple product states is that in order to enter the ignition regime, the plasma should have a high enough density (n), at a high enough temperature (T) and should be confined during a sufficiently large period of time (τ_E).

I.2.2. Confining plasmas

I.2.2.1. Plasma

Plasma is defined as an ionized quasi-neutral gas whose behavior is dominated by collective effects. When a gas is heated high enough the electrons scape from the atoms due to collisions, which leads to a separation of charges. While in most of neutral fluids the dynamics of motion is determined by forces between near-neighbor regions, the charge separation in plasmas gives to electric fields and magnetic fields, implying a wide range of complex phenomena. The solar corona is a plasma and the solar wind in the solar system is a plasma as well. Plasma is present in many aspects of our life, from industrial processes as welding to the Earth's ionosphere. In table 1.1 are shown some examples of the main natural and laboratory plasmas as well as its parameters (temperature, density and magnetic field). Then some basic concepts are explained:

	Length scale (m)	Particle density (m^{-3})	Temperature (eV)	Magnetic field (T)
Interstellar gas	10^{16}	10^{6}	1	10^{-10}
Solar wind	10^{10}	10^{7}	10	10^{-8}
Van Allen belts	10^{6}	10^{9}	10^{2}	10^{-6}
Earth's ionosphere	10^{5}	10^{11}	10^{-1}	10^{-5}
Solar corona	10^{8}	10^{13}	10^{2}	10^{-9}
Gas discharges	10^{-2}	10^{18}	2	No field
Process plasmas	10^{-1}	10^{18}	10^{2}	10^{-1}
Fusion experiment	1	$10^{19} - 10^{20}$	$10^{3} - 10^{4}$	1
Fusion reactor	2	10^{20}	10^{4}	5

Table 1.1 Plasma parameters for different cases of natural and human-made plasmas.

Plasma frequency: The plasma frequency is one of the most fundamental time scales in plasmas. The charge separation existing in plasmas is the responsible of electrostatic oscillations for both species, ions and electrons. However, the big difference in mass results in an effectively electrostatic movement of electrons around the background ions. The electron plasma frequency, which corresponds to the electron oscillation frequency in response to a small charge separation, is given by:

$$\omega_p^2 = \frac{ne^2}{\varepsilon_0 m} \tag{1.6}$$

For a typical fusion plasma conditions ($n_e \approx 10^{19} m^{-3}$) the plasma frequency is in the range of 100 GHz, whereas in the ionosphere ($n_e \approx 10^{12} m^{-3}$) the plasma frequency is of about 10 MHz. In particular, the ionosphere acts like a very good mirror for radio waves well below ω_p and allows the waves to 'bounce' over the horizon. For radio waves well above this cutoff frequency, the ionosphere is virtually transparent and the signals continue out into space. On the other hand, high frequency radiation is needed to heat the core plasma of magnetic fusion devices.

Debye's Screening: Quasi-neutrality basically means the apparent charge neutrality of a plasma overall, while at lower space scales, there can be charged regions, leading to electric fields. In addition, quasi neutrality explains how plasma itself shields any charge or electric potential that is introduced on it by creating a sphere beyond which the global neutrality of the plasma is kept. The radius of this sphere is known as Debye's length, and it quantifies the distance from the perturbing electric potential at which there is not net charge. The Debye length λ_D depends on plasma density and temperature:

$$\lambda_D = \left(\frac{\epsilon_0 kT}{n_0 e^2}\right)^{0.5} \tag{1.7}$$

where n and T are the electron density and temperature, respectively; ϵ_0 is the electric permittivity and k is the Boltzman constant. It follows that, for example, the Debye length takes values of $\lambda_D \approx 7 \cdot 10^{-5} m$ for a fusion plasma with $T_e \approx 1\ keV$ and $n \approx 10^{19} m^{-3}$. The plasma parameter (N_D) is the typical number of particles contained in the Debye sphere:

$$N_D = \frac{4\pi n \lambda_D^3}{3} \tag{1.8}$$

I.2.2.2. Magnetically confined plasmas

For an ionized gas to behave like a plasma, it is required a small Debye length in comparison with the macroscopic size of the gas (L >> λ_D) and $\omega\tau > 1$, being ω the frequency of typical plasma oscillations and τ the time between collisions with neutrals. Also it is required a large number of particles in a Debye sphere ($N_D \gg 1$) for the long-range collective effects characteristic of plasmas. Plasma should satisfy additional constraints to be considered fusion plasma.

Since fluids and plasmas are collections of particles, we can consider a collection of N particles and look at the different levels at which one may wish to develop dynamical theories for this system. These different levels are summarized in the table 1.2. At a very fundamental level, all particles may obey quantum mechanics. The state of the system at this level is given by the N-particle wave function, which evolves in time according the Schrödinger´s equation. In fusion plasmas quantum mechanical effects are negligible to describe the particle dynamics. At the next higher level, the system can be modelled as a collection of N classical particles described by Newton equations and by distribution functions. At the final level, we model the system as continuum (fluid model) by means of magneto-hydrodynamic equations.

Level	Description	Dynamical equilibrium
N quantum particles	$\Psi(x_1, x_2, \dots, x_N)$	Shrödinger equation
N classical particles	$(x_1, x_2, \dots, x_N; u_1, u_2, \dots, u_N)$	Newton's Law's
Distribution function	$f(\vec{x}, \vec{u}, t)$	Vlasov equation
One (Two)-Fluid model	$\phi(x), T(x), V(x), B(x)$	MHD equations

Table 1.2 Theory level in plasmas.

I.2.2.3. Single particle motion: orbits and drifts

In the case of the nuclear fusion strategy based on magnetic confinement, it is required to isolate the reactive nuclei from the surrounding environment by means of an intense magnetic field.

The movement of a charged particle with mass **m** and velocity **v** in the frame of electric, **E** = **E**(**r**, t), and magnetic, **B** = **B**(**r**, t), fields is governed by the combination of Lorentz and electrostatic forces. As the gravity represents a very small effect, it can be neglected:

$$\boldsymbol{F} = m\frac{dv}{dt} = q(\boldsymbol{E} + \boldsymbol{v} \times \boldsymbol{B}) \tag{1.9}$$

In these conditions the particles describe orbits spinning on the magnetic field lines with a given frequency, ω_c and characteristic radius, r_L, known as electron cyclotron frequency and gyro radius, respectively.

$$\omega_c = \frac{mv_\perp}{|q|B} \tag{1.10}$$

$$r_L = \frac{|q|B}{m} \tag{1.11}$$

Equation (1.9) can be solved for a wide variety of cases making use of the guiding center theory and assuming that the spatial variations of **E** = **E**(**r**, t) and **B** = **B**(**r**, t) must occur on a length scale long compared to the gyro radius and during slow time scales compared to the plasma frequency ω_p. In the absence of electric field and under constant uniform magnetic field **B** a charged particle describes parallel $v_\parallel$ and perpendicular $v_\perp$ trajectories to the magnetic field lines. Only the perpendicular component of the velocity interacts with the magnetic field, leading to a circular movement perpendicular to **B**. When an electric field is present in addition to the magnetic field, the charged particles will experience a force $\left(\vec{F} = q\vec{E}\right)$ that leads to the so-called $E \times B$drift:

$$\boldsymbol{v}_{E\times B} = \frac{\boldsymbol{E}\times\boldsymbol{B}}{qB^2} \tag{1.12}$$

It should be noted that the $E \times B$drift is independent of both the charge and mass of the particle.

In the presence of inhomogeneous magnetic fields new drifts should be considered: the so-called ∇B drift and curvature drift, where ions and electrons would drift in opposite directions.

Finally in order to understand particle orbits in magnetic fusion devices, the concept of magnetic mirror should be introduced. It relies on the conservation of energy and the invariant of the magnetic moment($\mu = mv_\perp^2/2B$). As a consequence of the conservation of the magnetic moment two main types of orbits appear; those corresponding to particle reflected by the magnetic mirror (trapped particles) and those which are not (passing particles).

I.2.2.4. Plasma as a fluid

Nuclear fusion plasmas are complex systems wich can be also described by a fluid model. Magnetohydrodynamics (MHD) is based on the consideration that plasma can be treated as an ensemble of charged particles acting as a fluid under strong magnetic field [34].

Continuity equation of plasma: Considering a differential element of volume, the rate of change of the number of particles in the cube due to the flow of particles across its surface is given by the continuity equation:

$$\frac{\partial n}{\partial t} + \nabla(n\boldsymbol{u}) = S \tag{1.13}$$

where S represents the source rate of particles in the volume element and **u** is the fluid velocity.

Momentum balance equation: The momentum balance equation equals the fluid acceleration to the sum of a number of forces due to electric (E) and magnetic (B) fields and pressure gradients $(\boldsymbol{\nabla P})$.

$$mn\frac{d\boldsymbol{u}}{dt} = nq(\boldsymbol{E} + \boldsymbol{u}\times\boldsymbol{B}) - \boldsymbol{\nabla}\cdot\boldsymbol{P} \tag{1.14}$$

The continuity equation can be applicable to both ions and electrons separately, but in the case of the momentum balance equation, the effect of collisions between particles of different species has to be considered. The momentum balance equation for the specie $\boldsymbol{\alpha}$ results as follows:

$$m_\alpha n_\alpha\left(\frac{\partial \boldsymbol{u_\alpha}}{\partial t} + (\boldsymbol{u_\alpha}\cdot\boldsymbol{\nabla})\boldsymbol{u_\alpha}\right) = n_\alpha q_\alpha(\boldsymbol{E} + \boldsymbol{u_\alpha}\times\boldsymbol{B}) - \boldsymbol{\nabla}\cdot\boldsymbol{P_\alpha} + \sum\nolimits_\beta R_{\alpha\beta} \tag{1.15}$$

where the summation is over all species β with which particles of species α can collide and $R_{\alpha\beta}$ is the term due to collisions.

Plasma resistivity: Electrical resistivity η limits the current that can be driven by an electric field, due to the collisions between ions and electrons. Assuming an applied electric field parallel to the magnetic field, the electrons are expected to reach an equilibrium state relatively fast due to their negligible inertia and very small mass, compared to ions.

$$E_{\parallel} = -\frac{m_e \nu_{ei}}{e}(u_{\parallel e} - u_{\parallel i}) = \frac{m_e \nu_{ei}}{n_e e^2} j_{\parallel} = \eta j_{\parallel} \tag{1.16}$$

Being ν_{ei} the collision frequency and $\eta = \frac{m_e \nu_{ei}}{n_e e^2}$ the resistivity, the constant of proportionality between the applied electric field **E** and the current density **j.** Then, the momentum gained by electrons due to collisions with ions is given by:

$$\boldsymbol{R}_{ei} = \eta n_e \boldsymbol{j} \tag{1.17}$$

For a typical fusion plasma of $T_e \approx 1\ keV$ and Z=1, resistivity has a value of about $10^{-8}\Omega$m, which is comparable to the resistivity of copper at room temperature. Then, very large currents are produced by very small voltage differences.

Diamagnetic drift: By using the one-fluid momentum balance equation (1.14), it follows that the perpendicular velocity is given by:

$$\boldsymbol{u}_{\perp} = \frac{\boldsymbol{E} \times \boldsymbol{B}}{B^2} + \frac{\boldsymbol{B} \times (\boldsymbol{\nabla} \cdot \boldsymbol{P})}{nqB^2} \tag{1.18}$$

The first term of the right-hand side is the $\boldsymbol{E} \times \boldsymbol{B}$ drift. The second term is known as diamagnetic drift. The diamagnetic drift gives rise to the currents that leads to a reduction of magnetic field inside the plasma. The diamagnetic current of ions and electrons is summed and leads to:

$$\boldsymbol{j}_d = \sum nq\boldsymbol{u}_{\perp} = \boldsymbol{B} \times [\boldsymbol{\nabla} \cdot (\boldsymbol{P}_i + \boldsymbol{P}_e)]/\boldsymbol{B}^2 \tag{1.19}$$

I.2.2.5. Properties and concepts of magnetic confinement fusion

MHD equilibrium: For a steady-state solution of the ideal MHD equations for the case of **u=0**, plasma pressure and magnetic field must satisfy:

$$\boldsymbol{J} \times \boldsymbol{B} = \boldsymbol{\nabla} p \tag{1.20}$$

which requires that the magnetic force balances the force due to plasma pressure.

Flux surfaces: The flux surface is the surface where B is everywhere perpendicular to its normal. The magnetic field lines lie in the surfaces of constant pressure, nested toroidal surface.

Rotational transform and safety factor: Curvature drift affects both ions and electrons contained in the plasma, inducing a vertical electric field that leads to an outwards $\boldsymbol{E} \times \boldsymbol{B}$ drift, which is against the desired confinement. Then, an additional component of the magnetic field in the poloidal direction, $\boldsymbol{B_\theta}$ is needed. This magnetic field component twists the magnetic field lines, preventing the particles from drifting outwards radially. The degree of the twisting is described by the rotational transform angle:

$$\frac{\iota}{2\pi} = \frac{d\Psi}{d\Phi} = \frac{R}{r}\frac{B_\theta}{B_\phi} \tag{1.21}$$

where R and r are the major and minor radius, B_θ and B_ϕ are the poloidal and toroidal components of the magnetic field and Ψ and Φ are the toroidal and poloidal magnetic fluxes. The inverse of $\frac{\iota}{2\pi}$ is called "safety factor.

Definition of plasma Beta: Plasma beta (β) is a coefficient to express plasma confinement performance. It is the ratio between the plasma thermal energy and the magnetic field energy:

$$\beta = \frac{<p>}{B^2/2\mu_0} = \frac{nk_BT}{B^2/2\mu_0} \tag{1.22}$$

Plasmas have reached empirical values of $\beta \approx 4\%$ in some fusion devices [35].

Energy confinement time:. One of the factors of the triple product which defines the Lawson criterion is the energy confinement time τ_E, which is defined as the rate at which the system loses energy:

$$\tau_E = \frac{W}{P} \tag{1.23}$$

where W is the plasma energy content and P is the total power input.

Scaling laws have received a renewed attention for two reasons. First, the nature of scaling laws provide useful information on the confinement underlying mechanisms. Second, this method provides in principle a reliable way to extrapolate present fusion devices performances towards a reactor. Global confinement scaling laws have been developed for tokamaks (e.g. ITER-93H scaling law for predicting the ITER base-line scenario) and stellarators (e.g. ISS04) [36].

$$\tau_E^{ISS04} = 0.465a^{2.28}R^{0.64}P^{-0.61}n_e^{0.54}B^{0.84}\iota^{0.41} \tag{1.24}$$

where R and a are the major and minor radius respectively, P is the absorbed power in MW, n_e is the line averaged electron density ($10^{19}m^{-3}$), B is the magnetic field (T) and ι is the rotational transform.

I.2.3. Magnetic confinement devices

I.2.3.1. Tokamaks

The tokamak is a device that uses magnetic fields, characterized by toroidal symmetry, to confine high temperature plasmas. Tokamak was thought by Oleg Lavrentiev and experimentally achieved by Ígor Tam and Andréi Sajarov in the decade of 1950, in the Kurchatov Institute for the Atomic Energy, placed in Moscow (USSR) [37].

Fig. 1.4 shows schematically the main elements of a tokamak. The toroidal magnetic field is generated by means of toroidal field (in yellow) and poloidal coils (in red). A central solenoid in the center of the device (in red) induces a current I_p (in yellow) in the plasma (in yellow) in the toroidal direction. The plasma current generates a magnetic field in the poloidal direction which then leads to helical magnetic field lines, needed to assure the confinement of the particles. The tokamak configuration gives axi-symmetry, which is the basic assumption in the calculation of tokamak equilibria and it allows to reduce the MHD equilibrium problem from three to two dimensions [38].

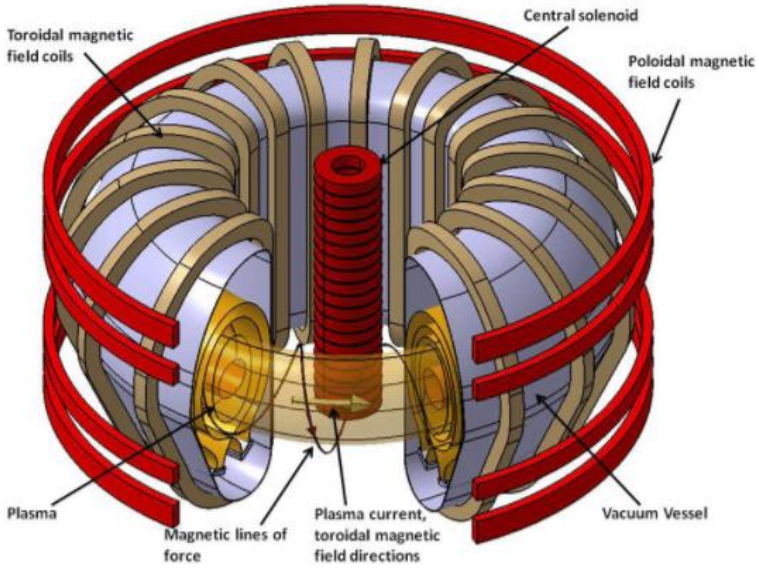

Figure 1.4 Schematics of TOKAMAK configuration. Courtesy of Ondrej Kudlacek.

The breakthrough into the peaceful use of fusion as an energy source began in Russia in 1968 when the tokamak magnetic confinement concept was tested showing an unseen capacity for containing high-temperature plasmas [39].The success of the tokamak prompted the construction of larger devices that started operation in the first half of the 1980s, such as the Joint European Torus (JET) in Europe, the Tokamak Fusion Test Reactor (TFTR) in USA and the Japanese Tokamak (JT-60) in Japan. Two tokamaks, JET and TFTR have achieved D-T fusion reactions. The JT-60U has achieved the record of the triple product in fusion energy [40].

At present Europe plays an important role in the preparation and exploitation of the tokamak JT60-SA that should start operation in 2021 in Japan. The next key research infrastructure is the ITER project, a worldwide endeavour, which should demonstrate the scientific and technological feasibility of fusion. ITER will generate ten times more fusion power than the power injected to sustain the fusion process.

I.2.3.1.1. JET Tokamak

JET (Joint European Torus), installed in Culham Centre for Fusion Energy (CCFE) is the world's largest device in operation. JET produced the first plasmas in the year 1983 and world record of fusion power (16 MW) 1997. In 1991, JET achieved first nuclear fusion reaction (D-T). JET also plays the important role of a useful test field for ITER. In figure 1.5 is shown an internal view of JET.

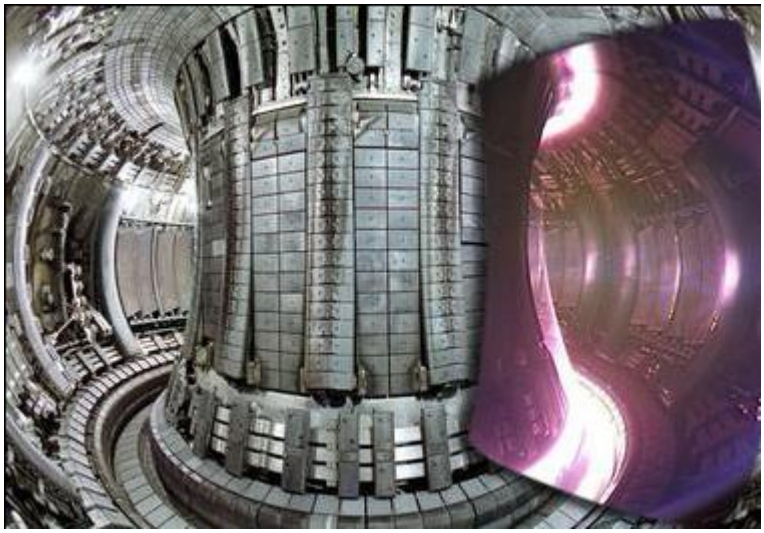

Figure 1.5 Internal view of the main chamber of the JET tokamak with a superimposed image of plasma obtained from visible spectrum video camera. Courtesy of Eduardo de la Cal.

Due to Tritium retention, the Carbon Fibre Composite (CFC) divertor was replaced by an alternative combination of materials: The divertor was made of tungsten and the first wall of Beryllium. PFC's have been installed at the divertor in order to manage the high power loads. Finally, in the main chamber, a beryllium first wall is installed. This is known as JET ITER like wall (ILW) and is currently in operation at JET (see figure 1.5).

I.2.3.2. Stellarators

The concept of stellarator was developed by Lyman Spitzer in 1950 in Princeton [41]. Like tokamaks, stellarators are toroidal confining devices but they show two fundamental differences: the confining magnetic field is generated by external coils and the lack of toroidal symmetry (fig. 1.6). The non-optimized magnetic configuration of earlier devices resulted in poor energy confinement and much better results were achieved using Tokamaks in the 1970s and 1980s. The main advantage of stellarator design is the ability of plasma operation in steady state, avoiding the current-drive instabilities as the poloidal magnetic field is not generated by plasma currents. However, as a consequence, the stellarator renounces to axisymmetry [42]. Extensive theory on stellarator design can be found in references [43, 44, 45].

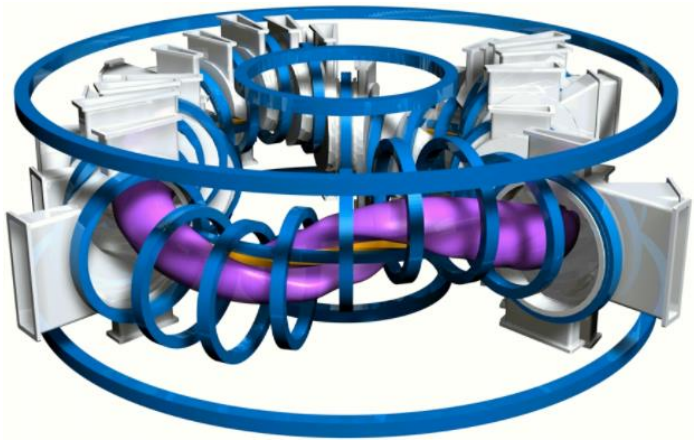

Figure 1.6 Schematics of stellarator configuration. From: http://www.fusion.ciemat.es/lnf/wp-content/blogs.dir/14/files/2013/10/TJII_model.jpg.

Stellarator diversity has been amplified with the development of improved concepts: quasi-toroidal symmetry [46], quasi-helical symmetry [47] and quasi-isodynamic symmetry [48]. When the magnetic field strength |B| is symmetric in magnetic coordinates (so-called quasi-symmetry), guiding-centre orbits and neoclassical confinement properties are equivalent to those in a tokamak. Within the family of optimized stellarators the quasi-isodynamic W7-X design is based on the minimization of all internal plasma current (i.e. Pfirsch-Schlüter and bootstrap currents).The successful start of the scientific exploitation of W7X is the first step towards bringing the stellarator to maturity as foreseen in the European Union roadmap.

I.2.3.2.1. TJ-II stellarator

The TJ-II stellarator is a four-period heliac stellarator which is located at Ciemat (fig. 1.7). TJ-II experiment started operation in 1997 and is still fully operative. TJ-II has an average major radius of $\langle R \rangle = 1.5\, m$ and a minor radius of $\langle a \rangle < 0.22\, m$. The magnetic configuration is obtained from a set of 32 magnetic coils which determine the magnetic configuration before the initiation of plasma. As a heliac, TJ-II disposes of twisted magnetic configuration which is generated by a helical central coil. The horizontal position of plasma is set by vertical field coils. The result is a bean-shaped vacuum magnetic surfaces. In figure 1.9 is shown a real view of TJ-II.

Figure 1.7 Image of TJ-II device. In the center of the image is placed the stellarator, which is surrounded by several access ports for diagnostics. Courtesy of: Laboratorio Nacional de Fusión.

The magnetic well of TJ-II is defined and widely modulated by the separately control of currents in the different coils. The magnetic field, which reaches values of up to 1 T, is produced by the action of the central coil (CC) and the toroidal field coils (TF) and the twisting effect is induced by the helical coil (HX). Finally the position of the magnetic axis is stablished by the action of the vertical coils (VF). The current flowing through central, helical and vertical coils is the parameter used to modulate the magnetic field.

Heating systems and fuelling in TJ-II

Electron Cyclotron Resonance Heating (ECRH) system is composed of two gyrotrons working at frequency 53.2 GHz under a power of 300 kW each one [49]. The power is transmitted to the plasma through quasi-optical transmission lines until the vacuum vessel [50].

Neutral Beam Injection heating (NBI) system consists of two beam injectors, placed at sector D8 and C1 of TJ-II, which is able to produce fast neutral hydrogen pulses. The acceleration of the pulse reaches 40 keV and can deposit up to 1.2 MW of heating power for a central electron density of $6 \cdot 10^{19} m^{-3}$ [51].

The TJ-II plasma in ECRH phase reaches densities of $n_e \approx 10^{19} m^{-3}$ and temperatures of $T_e \approx 1\ keV$ and during NBI heating phase the plasma can reach densities in the order of $n_e \approx 5 \cdot 10^{19} m^{-3}$ and temperatures of $T_e \approx 200 - 500\ eV$. In table 1.2 are described the most relevant parameters of TJ-II experiment.

TJ-II main parameters	
Major radius (R)	1.5
Magnetic field (B)	1
ECRH power (kW)	300 (× 2)
NBI power (kW)	600 (× 2)
Plasma relevant parameteres	
Minor radius (m)	0.1 to 0.25
Shear (%)	-1 to 10
Rotational transform at magnetic axis ($\iota/2\pi$)	0.96 to 2.5

Table 1.3 Main plasma and design parameters of TJ-II stellarator.

I.3. The Boundary Plasma, Plasma-Wall Interaction and Atomic Processes

The natural point of reference in the Boundary Plasma region of a tokamak or stellarator is determined by the Last Closed Flux Surface (LCFS) or magnetic separatrix. Radially inside the LCFS the magnetic surfaces are closed whereas radially outwards the magnetic field lines are opened intersecting surfaces. Inside the LCFS, the first layer ($\leq 5\ cm$) corresponds to the Edge Plasma that surrounds the core. In this outer region with closed flux surfaces steep gradients in electron density as well as in electron/ion temperature are developed. It is known that significant radial electric fields are present in the vicinity of the LCFS together with a wide range of atomic physics processes. In addition, one of the main challenges for the realization of a fusion power plant is the heat and power exhaust problem as well as the erosion of PFC and the control of impurities entering the plasma. The underlying physics is called Plasma-Wall interaction. The power and particle flux that cross the LCFS is diverted along the magnetic field lines to a remote region (the divertor) and, eventually, reaches the first wall. Therefore transport across the SOL is a key issue for the design and operation of future devices as it is crucial in determining the power loads both at the divertor and first wall of the machine. Another important function of the divertor and first-wall is the particle control, providing adequate pumping capability to exhaust the neutralized gas and particles as well as to retain impurity sources such that they will not enter the main plasma.

I.3.1. The Edge Plasma region

The Edge Plasma is the outer confined region placed between the core dense and hottest plasma and the SOL region where flux surfaces are not closed. The physics and characteristics of the Edge Plasma are different from those of the plasma core as it is governed by strong gradients in temperature, density and pressure. The relevance of the plasma edge is given by the transport processes affecting particles and energy, which, consequently, have strong implications on the bulk plasma confinement.

In TJ-II plasmas, for example, the Edge Plasma density is $10^{18} < n_e(m^{-3}) < 10^{19}$, typically and $10 < T_e(eV) < 100$. On the other hand, electron temperature can reach 1 keV in the plasma core. On the other hand, in the JET H-mode plasmas, the plasma temperature in the edge can surpass 1 keV while the density is sensibly larger than in the edge of TJ-II stellarator, as shown in the table 1.4. Interestingly, the width of the Edge plasma region is a few cm in both devices.

In the Edge Plasma during H-mode the plasma density and temperature profile gradients become enhanced because transport barriers are formed. Unlike the core plasma, the proximity of the edge region to the limiting walls makes the non-ambipolar particle fluxes appear, leading to the formation of the Neoclassical radial electric field, which is studied in this PhD thesis (see section I.4). Also, the interplay between different scales of turbulence and its self-organization and control take place in this region (see section I.4).

TJ-II stellarator	**Joint European Torus**
$10\ eV < T_e < 100\ eV$	$10\ eV < T_e < 1\ keV$
$10^{18} m^{-3} < n_e < 10^{19} m^{-3}$	$10^{19} m^{-3} < n_e < 5 \cdot 10^{19} m^{-3}$

Table 1.4: Electron density and temperature ranges in the Edge Plasma region of the TJ-II stellarator and the JET tokamak.

The Edge plasma is strongly influenced by the processes from the SOL region, which, at the same time are conditioned by the physics of the interaction between plasma and wall. In particular, the penetration of recycled neutrals from the wall into the edge plasma is not negligible and has strong influence on the stability of the pedestal, having consequences on the global plasma confinement. The intensity and characteristics of these processes are given by an extensive underlying physics, which is addressed in the next sections.

I.3.2. Scrape-off layer

The Scrape-off Layer (SOL) is defined as the outermost plasma region in where magnetic surfaces are no longer closed, since they intersect the plasma facing components. Particle and heat are transported mainly along magnetic flux surfaces and are gradually absorbed by plasma facing surfaces. The SOL is limited by limiter or divertor targets. In limiter and divertor tokamaks the scrape of layer is toroidally symmetric in a first approximation. Due to the mass difference and thereby higher mobility, electrons reach target surfaces more easily than ions. Consequently, the surface becomes negatively charged with respect to the plasma, and a thin sheath is formed that shields electrostatic potential. However, due to the thermal motion of both ions and electrons, the shielding is not perfect and the ions are attracted towards the target by the electric field in the region between sheath and plasma bulk, known as the pre-sheath (fig. 1.8).

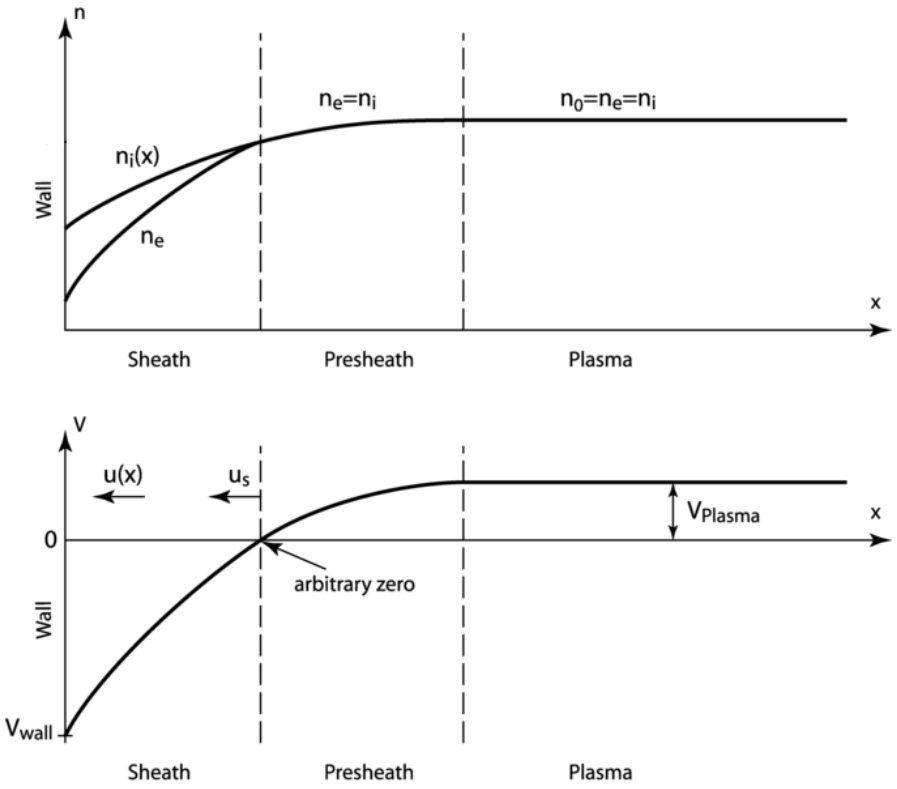

Figure 1.8 Above, ion and electron density in the sheath and pre-sheath. The bottom figure shows the potential close to the plasma wall. From https://commons.wikimedia.org/wiki/File:Collisionless_plasma_sheath.png

The distance along which magnetic field lines explore the SOL without crashing surfaces is known as the connection length L_c. This parameter is of the order of tens of meters in the JET tokamak while in the W7-X $L_c \approx 100 - 1000\ m$. In the TJ-II stellarator, $L_c \approx 1\ m$ [52].

In the SOL, $n_e(r)$ and $T_e(r)$ decay exponentially outwards with characteristic decay lengths λ of typically one to several centimetres ($e^{-r/\lambda}$). The perpendicular diffusion in the SOL, mainly due to turbulence, is characterized with its decay length and L_c. The plasma flows symmetrically towards both ends of the SOL, where the parallel flow velocity $v_\parallel$ equals the sound speed $v_s = \sqrt{k(T_e + T_i)/m_i}$, driven by the pressure gradient induced by the plasma sink action of the target surfaces.

The transport within the SOL can be treated as the summation of the flow along magnetic field lines and the dominant radial turbulent transport. At low density plasmas, ions and electrons enters the SOL from the confined plasma region by cross-field diffusion. No ionization of neutrals take place in the SOL in this case. The temperature and density gradients along the magnetic field lines are almost zero $(\nabla T_{e,i} \approx \nabla n_{e,i} \approx 0)$ then the heat transport is mainly convective in the SOL, in the form of an isothermal fluid flow (see figure 1.9) and parallel plasma flow is present throughout the entire SOL. This is the so-called Low recycling regime.

On the other hand, in scenarios where plasma is generated at the SOL by ionisation processes, a higher $\langle n_e \rangle$ region arises close to the target, in the divertor region, with the subsequent decrease of T_e. Then, a temperature gradient is developed ($\nabla T_{e,i} \neq 0$) within the SOL. As in the case of low plasma density, the heat sources are localised in the plasma core, but heat transport is dominantly conductive within the SOL. Volumetric heat sinks (radiation) become important, reducing the amount of heat reaching the target surfaces. In consequence, the parallel plasma flow appears only in the region close to the target, dominated by ionization reactions (fig. 1.9). In the case that $\langle n_e \rangle$ reaches even larger values in the divertor region (see section III.4) T_e could be reduced below 1eV. Under these conditions, a recombination volume is formed, which is an additional sink of particles. The following reference is recommended to have a more complete understanding of heat and particle transport in the SOL of tokamaks [53].

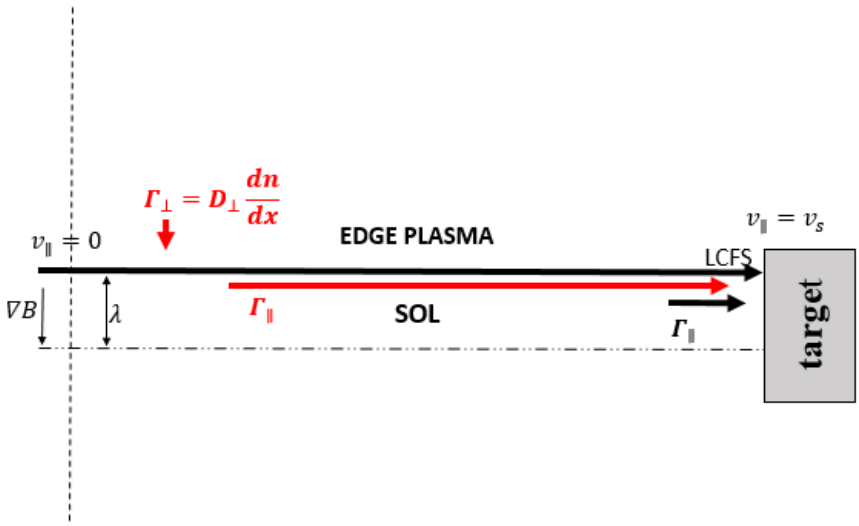

Figure 1.9 Scheme of parallel and perpendicular particle transport along the SOL and across the Last Closed Flux Surface. In red, low density plasmas. In black, high density tokamak plasmas.

The existing particle and heat transport into the plasma SOL from the edge is strongly influenced by the level of turbulence (anomalous transport) which dominates transport in the edge region (explained in section I.4).

I.3.3. Plasma-wall interaction

The interaction between the plasma and material surfaces that are in contact with it, known as Plasma Facing Components (PFC), is determinant in achieving high performance plasmas and safe operation of the magnetic confinement devices. The most relevant issues falling in the field of plasma-wall interaction are the following:

Recycling: Ions and electrons impact and penetrate through the surfaces of PCF and are neutralized. This process is followed by their releasing from the PFC back to the plasma. There are indications that the behaviour of the recycling affects the global plasma parameters (this is explained in detail in section III.4).

Particle exhaust by pumping: Magnetic plasma fusion devices use pumping systems to exhaust fuel (*H, D, T*) and impurities ($He, H_2O, Be, W \ldots$) to control the density and remove impurities. The exhaust of Helium ash is a challenge for the future nuclear fusion reactors operating with D-T reactions to avoid fuel dilution.

Power Control and Exhaust: The power loads against the PFC need to be controlled in order to avoid melting or sublimation of the materials. This is of special importance in the divertors and limiters, where these loads are concentrated. Following aspects must be dealt with when designing the PFC of fusion devices: Choose materials with high melting point, such as Carbon (C) or Tungsten (W), shape the geometry to minimize the power density and spread the heated area. In addition, taking in account the impact of impurities in the plasma contamination, for the case of devices with long plasma discharges ($> 10\ s$), active refrigeration with coolants is mandatory. This method has been used already in superconducting devices such as WEST tokamak and in the W7-X stellarator and is going to be employed in ITER.

Erosion: Material surfaces in contact with the plasma become eroded, due to Sputtering, Melting, Sublimation and Arching. Besides eroding the materials, these phenomena lead to the generation of impurities which may enter the confined plasma and contaminate it. The presence of impurities in the plasma leads to plasma cooling by radiation losses and when becoming sufficiently high, to disruptions (in Tokamak devices) and Radiative Collapse (in Stellarators).

Two main configurations for the magnetic field have been designed in order to control de plasma-wall interaction: divertor configuration and limiter configuration. In a limiter plasma the Last Closed Flux Surface (LCFS) is determined by the intersection of the magnetic field lines by a material object. On the other hand, in the divertor configuration the confined plasma region is isolated by a separatrix, which separates the closed from the open magnetic field lines to avoid Edge Plasma contact with PFC, decoupling it with the help of the SOL plasma.

Divertors have been introduced as one of the earliest theoretical concepts in the field of nuclear fusion. The function of the divertor itself is to extract the heat and ash produced by the fusion reactions, as well as minimize plasma contamination and protect the surrounding walls from the thermal and particle loads. The magnetic field lines carry out the high energy particles of the plasma and make them strike vertical targets which are positioned at the intersection between the field lines.

The power flux directed to the ITER divertor can be up to 10 MWm^2 in steady state conditions (and until 20 MWm^2 during transients). In principle, a Carbon-made divertor was though for ITER due to its promising plasma-wall control. However, the evidences showing that Carbon has a great capacity to retain a relevant fraction of Tritium led to the prediction that ITER would not fulfil the requirements concerning the maximum Tritium inventory [54]. After years of hard R&D work, configuration with W divertor and Be first wall has been chosen and tested as the future PFC combination for the First wall for ITER (see section III.4). Its main advantage is the low retention of Hydrogen species. However, the main disadvantage when using Tungsten is that high-Z impurity may enter the plasma producing huge radiation losses and thereby confinement degradation and even disruptions [55].

I.3.3.1. ELM instabilities

Edge Localised Modes (ELM´s) are instabilities which appear during H-mode in the Edge Plasma. ELM or ELM-like instabilities are characterized by the relaxation of pressure and density gradients in the pedestal with the consequent degradation of the edge transport barrier and the expulsion of particles and heat flux towards the divertor. This is followed by a recovering phase in which gradients steepen again and transport barrier is recovered [56]. Empirically, ELM's are seen as quasi-periodic emission of bursts of heat flux and wall emission with a given frequency. In figure 1.10 is shown the time evolution of D_α emission and I_{sat} in the inner divertor during a period of time which contains three ELMs.

ELMs are characterized by their frequency (f) and power load ΔW. ELMs frequencies are of 10 – 100 Hz, while the power loads are of $\Delta W \leq 10$ %. ELMs are originated by a MHD instability, which lead to the partial loss of the confinement of energetic ions and electrons in the Pedestal Edge Plasma region, which are directed towards the first wall and divertor. In contrast with electrons, which are mainly thermalized [111], ions arrive with their initial energy and become accelerated in the plasma sheath. For example, in JET H-mode plasma, $T_i \approx 1\ keV$ and the acceleration is a factor of about 4 [111].

Both types of ELMs are originated in a thin layer close to the plasma edge. ELMs can be classified, mainly, in type-I and type-III instabilities, in function of their frequency and mode structure. The type-III ELMs have a frequency of about 4-5 times higher than the type I ones. The type-III ELMs are more dependent on the edge pressure gradient. Concerning the mode numbers, *m* and *n*, type III ELMS have slightly larger values than for the case of type I [57].

ELM's represent a serious challenge for the future operation of ITER, due to the huge loads of power flux towards walls among other problems such as damaging tungsten sputtering and erosion.

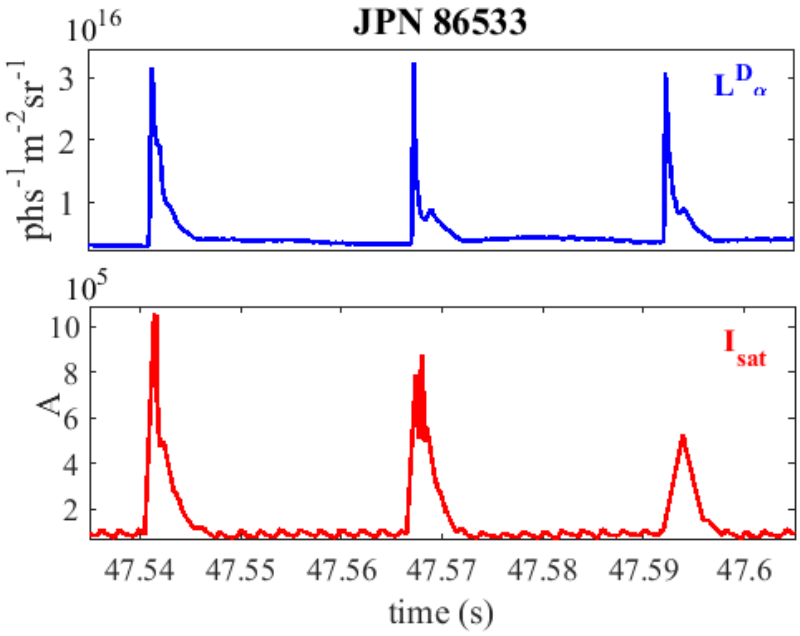

Figure 1.10. Time evolution of the D_α radiance and ion saturation current I_{sat} during three ELMs in a typical JET H-mode plasma.

I.3.4. Plasma Recycling

Plasma fuel is composed of ions (Hydrogen isotopes), electrons and neutral particles. Ions and electrons carry the convective power flux against the PFC's. Although in the future burning Fusion reactors the fuel will be a mixture of Deuterium (D) and Tritium (T) ($\approx 1:1$), experimental devices operate generally with H (e.g. TJ-II) or D (JET). It has to be pointed out that all the three Hydrogen isotopes have equivalent physical and chemical properties in many aspects. Deuterium (D) will be used in the present work in the sections I.3.3, II. 2 and III.4, referring thereby also to the other hydrogen isotopes: Hydrogen and Tritium.

Ions (and electrons) diffuse perpendicularly to the magnetic field lines towards the PFC's (Divertors, Limiters or the First Wall itself), where they are neutralized and are reemitted as neutral particles towards the plasma. The underlying physics of this process is known *as Plasma Recycling.*

The magnetically confined plasma in fusion devices is a system in which the walls act as a particle sink of charged particles. Two magnitudes are the key constituent elements of magnetically confined plasmas: energy and particle contents. Energy is supplied by heating

while the quantity of particles is sustained by a permanent flow of gas from the wall (and by external puffing as well as pellet injection). Under typical conditions taking place in the plasma Scrape-off layer, ions reaching solid surfaces experience the following processes: A first fraction of ions R_N are reflected once they hit the surface and maintain a significant fraction R_E of energy. R_E and R_N depend on the material composition and the ion mass and its energy (as seen in figure 1.11).

The other fraction of ions $(1 - R_N)$ penetrates the surface, and are mostly desorbed back to the plasma thermally as D_2 molecules (fig. 1.11). By "thermally" is meant that they are re-emitted to the plasma with the energy corresponding to the surface temperature ($\leq 0.1\ eV$). These are known as *low energy* neutrals.

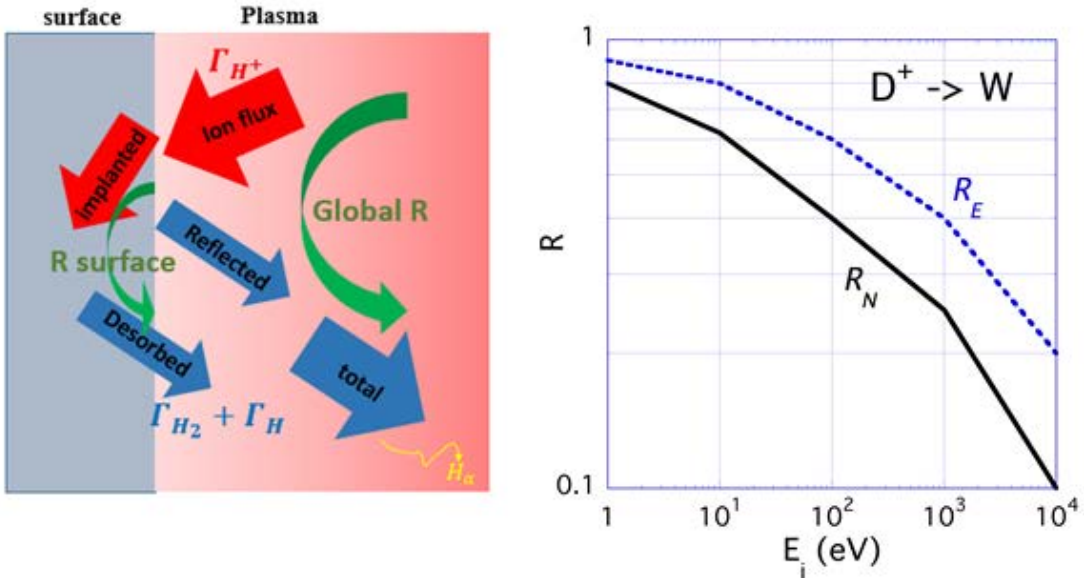

Figure 1.11 In the left hand side, overview of plasma fuel recycling processes. In the right hand side, the dependence of the reflection coefficient of ions on the ion energy. Courtesy of Eduardo de la Cal.

The fraction that remain implanted in the material (as represented in figure 1.11) depends on the so-called saturation level in the subsurface. This is, the capability of a material "X" to trap *D* and can be up to *1:1 (D:X)* for low Z materials such as Carbon. Once this level is reached in the subsurface region where the energetic *D* atoms from the plasma penetrate ($\approx 1\mu m$), the trapping capability falls and the *D* atoms diffuse out through the surface in the form of volatile D_2 molecules. The saturation level of a material depends strongly on its temperature. A coefficient can be stablished describing the ratio between the neutral *D* flux reemitted from the surface towards the plasma Γ^0 (reflected and desorbed) and the ion influx Γ^i impinging on the surface. This is known as the *Recycling coefficient* of the surface in contact with the plasma. Finally, it is important to consider that, since the reflected neutrals have much higher energy

than the thermally desorbed neutrals, the former will have a much higher penetration length in the plasma before being ionized.

I.3.5. Atomic Processes in the Boundary Plasma

Recycled neutral D and D_2 and also the externally injected fuel (puffing) will be subjected to many atomic processes when entering back into the plasma. A fraction of them will be ionized inside the Separatrix and will fuel the plasma in order to balance the ion and electron losses.

Let us define an atomic reaction or process as: $A + B \rightarrow C$, where *A, B and C* represent, in our case, any plasma species such as electrons, ions, atoms or molecules. The rate at which this process takes place in the plasma can be expressed as:

$$\frac{dn_c}{dt} = n_A \cdot n_B \cdot \langle \sigma v \rangle \tag{1.26}$$

where n_A and n_B are the densities of the species A and B, respectively and $\langle \sigma v \rangle$ defines the probability of the reaction to take place and is known as the Rate Coefficient of the reaction. The Rate Coefficient is obtained by integrating the product of the relative velocity v of the species *A* and *B* with the respective cross-section $\langle \sigma v \rangle$ and with the distribution function of the velocities, $f(v)$, which is well approximated by a Maxwellian distribution in the fusion Boundary plasma:

$$\langle \sigma v \rangle = \int v \sigma(v) f(v) dv \tag{1.27}$$

The main atomic processes and reactions involving neutral D and D_2taking place in the boundary plasma are high-lighted here [57]:

I) Electron reactions with D and D_2

I.1: $e^- + D \rightarrow 2e + D^+$ *Atomic ionization*

I.2: $e^- + D \rightarrow e^- + D^*$ *Atomic excitation*

I.3: $e^- + D_2 \rightarrow e^- + 2D$ *Dissociation*

I.4: $e^- + D_2 \rightarrow 2e^- + D_2^+$ *Molecular ionization*

I.5: $e^- + D_2 \rightarrow e^- + D + D^*$ *Molecular dissociation and excitation*

II) Electron reactions with D^+ and D_2^+

II.1: $e^- + D_2^+ \rightarrow e^- + D + D^+ + \upsilon$ *Molecular dissociation and excitation*

II.2: $e^- + D^+ \rightarrow D + \upsilon$ *Radiative recombination*

II.3: $2e^- + D^+ \rightarrow D + \upsilon$ $Radiative\ three-body\ recombination$

III) Reactions between D and D^+

III.1: $D + D^+ \rightarrow D + D^+$ $Charge\ Exchange$

The figure 1.12 shows the rate coefficients for some of the reactions above.

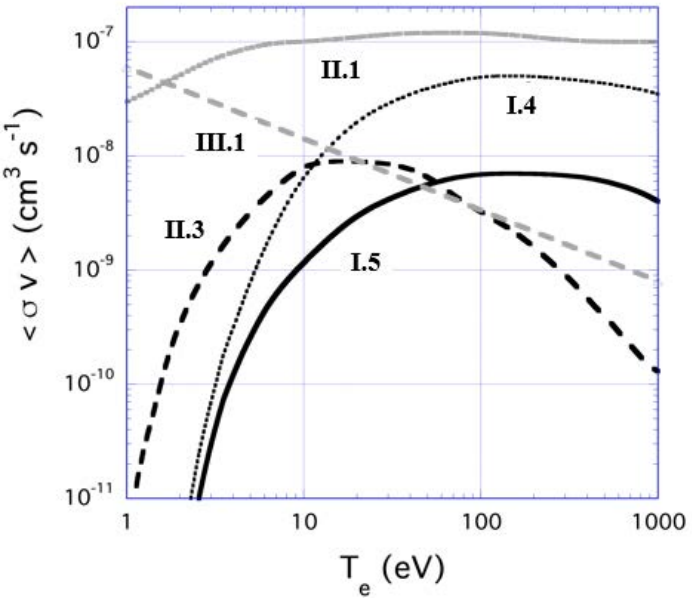

Figure 1.12 Cross-section of the most important atomic and molecular processes in the boundary [57].

In the boundary region of fusion plasmas the dissociation of molecular D into ground state has high probability for $10\ eV < T_e < 15\ eV$. At higher electron temperatures, the most probable process is the molecular ionization (I.4) previous to its dissociation (II.1). Finally, at intermediate electron temperature $T_e \approx 50 - 200\ e$, I.5 leads to the dissociation of the D_2 molecule to produce excited D in the level n=2 and competes with II.3 (also dissociation).

Many of the above Atomic reactions and processes that take place in the boundary plasma are radiative, i.e. photons are emitted. As will be shown later (section II.2), the Spectroscopic analysis of the plasma emission, together with the use of the proper atomic models allows us to understand the atomic physics taking place in Fusion devices and even to use this information to characterize the Boundary plasma itself.

I.4. Transport in plasmas

Transport is due to two different types of processes in magnetic fusion devices. The first is collisions between charged particles. This causes neoclassical transport (i.e. a branch of

collisional transport that takes into account the topology of the magnetic field), which is always present in fusion plasmas. Kinetic and random walk theories [58] are used to calculate transport coefficients. [59]. Reviews of the collisional transport theory can be found in [60] and [61].

The second process that causes transport is plasma turbulence and this gives rise to turbulent transport (sometimes called anomalous transport). In tokamak devices turbulent transport is the main cause determining the confinement time. Turbulence also contributes significantly to transport in stellarators, particularly in the outer region of the plasma. The turbulent transport is due to the turbulent movement of the magnetic field lines [62] when particles move radially outward following magnetic field lines, as well as to the presence of electrostatic turbulence.

I.4.1. Neoclassical transport: ambipolar radial electric field

Neoclassical Transport (NC) Model is one of the basic models to explain the physics of magnetically confined plasmas. NC transport is larger in non-optimized stellarators than in tokamaks. There are several different collisionality regimes for neoclassical transport in stellarators that have been reviewed in great detail elsewhere [60]. Assuming plasma in a quiescent state, NC models predict particle and heat transport due to collisions in complex 3D geometries.

Studies have shown both theoretically [63] and experimentally [171] that in stellarators the (long radial scale) radial electric field is set by neoclassical transport. The ambipolarity condition (i.e. the equality of ion and electron fluxes) determines the neoclassical radial electric field.

$$\Gamma_i(E_r) = \Gamma_e(E_r) \tag{1.28}$$

where Γ_i and Γ_e are the surface average transport fluxes of ions and electrons, respectively. There are two stable roots in stellarators: the ion root with typically negative E_r, usually achieved in high density plasmas, and the electron root with positive E_r that is typically realized when electrons are subject to strong heating. It is the neoclassical transport that determines the radial electric field on long (tens of gyroradius) length scales whereas turbulent mechanisms (e.g. Zonal Flows) can control short (few gyroradius) radial length scales.

I.4.2. Turbulent transport and Zonal Flows

In real plasma conditions transport exceeds neoclassical predictions by an order of magnitude or more. This difference is known as *anomalous transport* and it is assumed to be generated by plasma micro-instabilities [64] and has both local and global implications in confinement [65].

Optimizing and controlling plasma performance in stable conditions is a major issue and challenge that has deserved a great effort in the whole fusion program.

I.4.2.1. Sheared flows and E_r

Radial electric fields play a key role in the control of transport in fusion plasmas. Sheared $E \times B$ flows can influence the turbulence via shear decorrelation mechanisms and, as a consequence, they can modify the level of turbulent induced transport. A strong radial gradient in the radial electric field (E_r) produces strong shear in the particle ($E_r \times$ B) drift velocity (B being the toroidal magnetic field). The stretching direction tends to be parallel to the direction of the background flow. The coherence lengths along the direction perpendicular and parallel to the sheared flow can quantify the level of eddy stretching (Fig. 1.13). The coherence distance can be interpreted as the size of turbulent eddies.

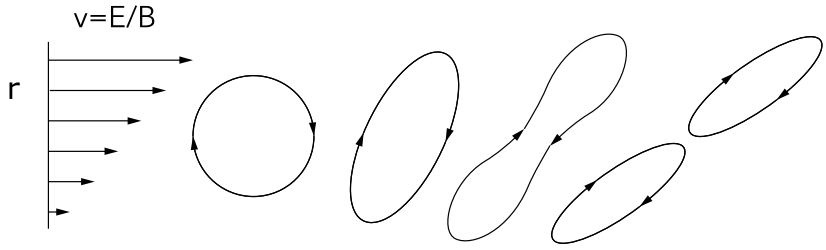

Figure 1.13 Stretching of turbulent eddies in the perpendicular direction due to the effect of shearing flow in the parallel direction.

The influence of sheared flows on turbulence can be expressed by a decorrelation time, proportional to the inverse of the radial gradient of E_r, $\tau_c \approx B^{-1}(dE_r/dr)^{-1}$. On the other hand, the decorrelation time due to background diffusion is estimated by $\tau_b \approx L_r^2/D$, where L_r is the radial scale length of fluctuations and D is the diffusion coefficient. When τ_c is smaller than τ_b, the sheared flow reduces the radial scale (correlation) length of the fluctuations, and consequently the level of anomalous transport. Historically, this mechanism for reducing turbulent transport was proposed for the explanation of the transition to the High Confinement mode (H-mode), which is now obtained routinely at the plasma edge of tokamaks and stellarators and corresponds to the ITER baseline scenario.

The force balance relation shows that the radial electric field depends on the ion pressure gradient (∇P_i), equilibrium flow poloidal and toroidal velocities (u_θ, u_φ) and the magnetic field in the toroidal and poloidal directions (B_φ, B_θ).

$$E_r = \frac{1}{Z_i e n_i}\frac{\partial}{\partial r}p_i - u_{\theta i}B_\varphi + u_{\varphi i}B_\theta \qquad (1.29)$$

Thus, the pressure gradient as well as the poloidal and toroidal flows play a crucial role in the development of radial electric fields and in the control of turbulence transport via sheared flows.

I.4.2.2. Turbulence and physics of Zonal Flows

The explicit macroscopic manifestation of turbulence are eddies which have different sizes and lifetimes and appear gradually when a fluid transits from laminar to turbulent regime. The Reynolds number, the ratio of inertial forces to viscous forces within a fluid in the Navier-Stokes equation, is defined as

$$Re = UL / \nu \tag{1.30}$$

where U is the velocity of the fluid, L a characteristic dimension and ν is the kinematic viscosity. At low Reynolds numbers, flows tend to be dominated by laminar flow, while at high Reynolds numbers turbulence results (Fig. 1.14).

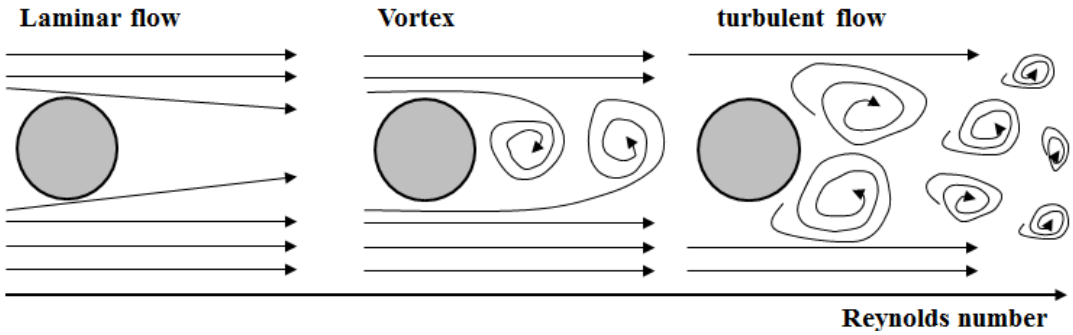

Figure 1.14 In this figure are illustrated the different flow regimes, from laminar to turbulent, through the formation of turbulent vortex.

Self-organization of plasma turbulence: negative viscosity: Electrostatic turbulence in magnetized plasmas is not isotropic in three dimensions due to the faster dynamics in parallel direction to magnetic field. This has implications in the *cascade mechanism*. Due to angular momentum conservation in an incompressible fluid, the vortexes are stretched in the direction of angular momentum. In an ideal two-dimensional fluid ($\mu = 0$) energy and enstrophy are conserved and is possible to find a *dual cascade situation* [66, 67].

The energy transfer between different spatial scales of the turbulence was studied first by Kolmogorov and is described in the K41 Theory [68] as the effect of energy input in a three-dimensional (3D) isotropic turbulent system. The basic idea of the K41 theory is that energy is injected into the system at some large scale (injection range k_i), then transferred towards smaller scales (inertial range) and finally dissipated through viscosity (dissipative range). K41-theory predicts that the energy decays with wave number as $k^{-5/3}$.

In a 2D fluid energy is transferred from the injection scale towards larger scales and enstrophy is transferred towards smaller scales. The two directions are called inverse cascade for energy and direct cascade for enstrophy transfer. Therefore, the name dual cascade is often used in the context of 2D turbulence. The inverse cascade is characterized by the relation $E \approx k^{-5/3}$ while the direct cascade shows k^{-3}. This is shown in fig. 1.15.

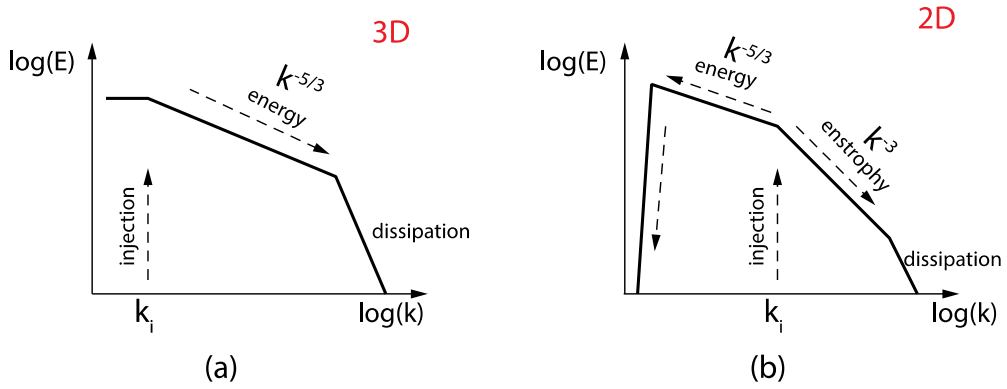

Figure 1.15 Energy transfer from large to smaller spatial scales. In absence of external input, energy flows from larger to smaller scales.

Self-organization of turbulence is proposed as the responsible mechanism of the conservation of the shape of plasma profiles [69, 70] and the inverse cascade energy transfer mechanism could be one of the underlying mechanisms [71].

Some conditions must be fulfilled in a system, as explained in a pioneering work by V. P. Starr in 1968, to show negative viscosity behavior in plasmas, i.e. inverse energy cascade [72]:

First, eddies which transport the momentum contrary to the gradient of mean flow must have a supply of turbulent kinetic energy.

Second, the mean flow should experience some form of braking (e.g. positive viscosity) so that its value does not increase without limit. However, this braking should be low enough to allow the generation of differential rotation.

Third, some kind of turbulent irregularity must be present. This ingredient is illustrated in fig. 1.16, showing a flow with some hypothetical pattern producing a convergence of momentum into the mid-channel. The essential features are the elliptical circulation and the systematic tilts of their major axes, which can be expressed as gradients in quadratic terms of fluctuating velocities. In steady state the turbulent drive is equal to the damping (i.e. for the poloidal dynamics).

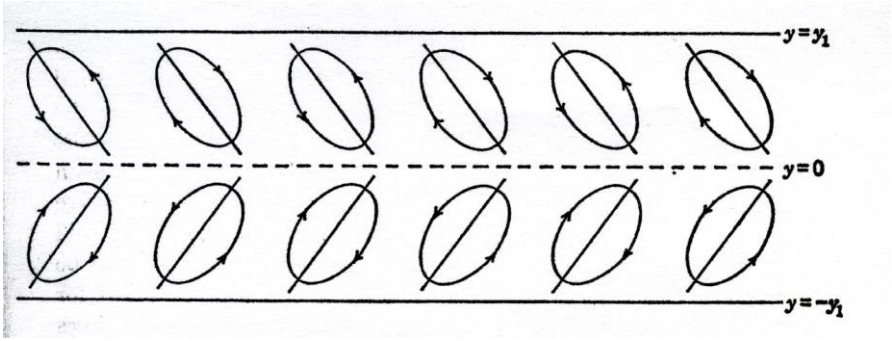

Figure 1.16 Typical hypothesized flow pattern in the presence of negative viscosity. The major axes of the turbulent structures is tilted.

When these conditions are fulfilled energy can be interchanged between the mean flow (large scales) and the turbulence (small scales), predicting the development of inverse cascade of turbulent energy spectra and condensation of the spectrum to form Zonal Flows which can control turbulent transport [73]. Zonal Flows are poloidaly and toroidally symmetric band-like shear flow structures with nearly zero frequency (i.e. frequency much smaller than those characteristics of broad-band turbulence).

The poloidal flow equation describing the dynamic of zonal flows is [74]

$$\frac{\partial \langle u_{\theta i} \rangle}{\partial} = -\frac{\partial}{\partial}\left[\langle \tilde{u}_{ri}\tilde{u}_{\theta i}\rangle - \frac{1}{m_i n_i \mu_0}\langle \tilde{b}_r \tilde{b}_\theta \rangle\right] - \mu_\theta \langle u_{\theta i}\rangle \qquad (1.31)$$

where $u_{\theta i}$ is the poloidal velocity of the specie i, $\tilde{u}_{ri}$ and $\tilde{u}_{\theta i}$ are the radial and poloidal velocity of fluctuations and μ_θ is the viscosity. Fig. 1.17 shows how instabilities driven by different free energy sources (i.e., density, pressure and temperature gradients) can produce turbulence. Sheared flows driven by radial electric fields (either driven by pressure gradients, rotation and Zonal Flows) can damp the turbulence level and the resulting transport can influence gradients themselves, giving rise to a feedback loop.

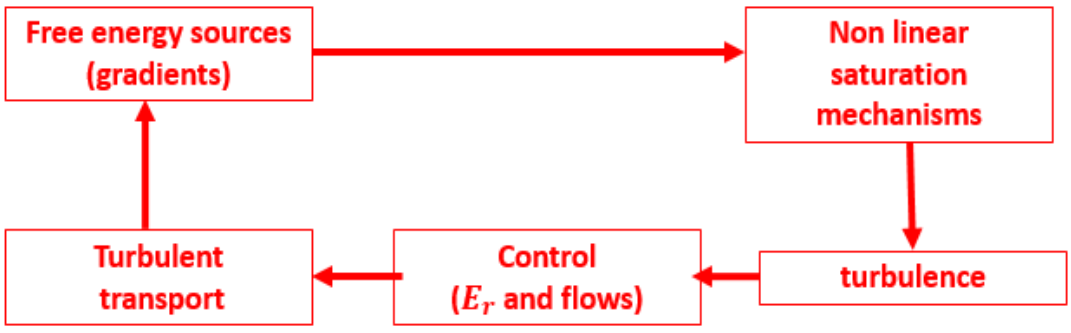

Figure 1.17 This diagram shows the interplay between turbulence (gradients) producing and damping mechanisms (shearing flows).

II. EXPERIMENTAL SET-UP AND METHODOLOGY

II.1. Langmuir probes

Electric probe technique was developed by Irving Langmuir in 1924 and is a fundamental diagnostic for measuring local properties of plasmas [75]. Actually electric probes are useful to measure temperature and density in a wide variety of gaseous ionized media such as ionized gases and also in shock waves, flames, fusion hot plasmas and atmospheric or space plasmas. Intense research work has been done in the field of electric probes, leading to abundant theory and practical applications [76, 77].

II.1.1. Langmuir probes theory and interpretation

II.1.1.1. Plasma sheath and Bohm criterion

The simplest collecting Langmuir probe is known as the "single probe". It consists of an isolated wire exposed to the plasma and biased with respect to a conducting portion of the vessel confining the plasma. More sophisticated probe configurations include double and triple probes.

While the probe is electrically isolated, a sheath forms at the plasma-probe surface interface to equalize electron and ions fluxes. As a consequence, the surface will reside at the floating potential (Φ_f), which is negative with respect to the plasma potential (Φ_p). The potential drop (Φ_f) occurs in a thin sheath which thickness is approximately tens of the Debye length.

$$\lambda_D = \sqrt{\frac{\epsilon_0 k T_e}{n_e e^2}} \tag{2.1}$$

For example for T_e and n_e in the range of 30 eV and $10^{18} m^{-3}$ respectively, gives $\lambda_D \approx 10\ \mu m$.

The existence of the electrostatic sheath has important implications with regard to plasma-wall interactions. In particular the physical sputtering of the material surface is enhanced due to the increased ion impact energy. The sheath also controls the rates at which particle and energy are removed from the plasma by the solid surface.

In addition to the electric field associated with the sheath, there is a pre-sheath electric field (where the potential drop is in the range of 0.5 kT_e/e) which extends further from the surface into the quasi-neutral plasma and accelerates the ions to reach the sound speed (c_s) at the plasma

sheath edge (Bohm criterion). It is found that the density at the sheath edge (n_s) is approximately one half of the density far from the probe (n_0).

II.1.1.2. Characteristic curve current-voltage

In the process of polarization of the probe the probe potential can be driven up and down with respect to the reference potential (typically the earth determined by the vessel containing the plasmas). This leads to differences in the dynamics of the collecting particles, resulting in a current – voltage characteristics (I-V curve) of a *single Langmuir probe* (fig. 2.1).

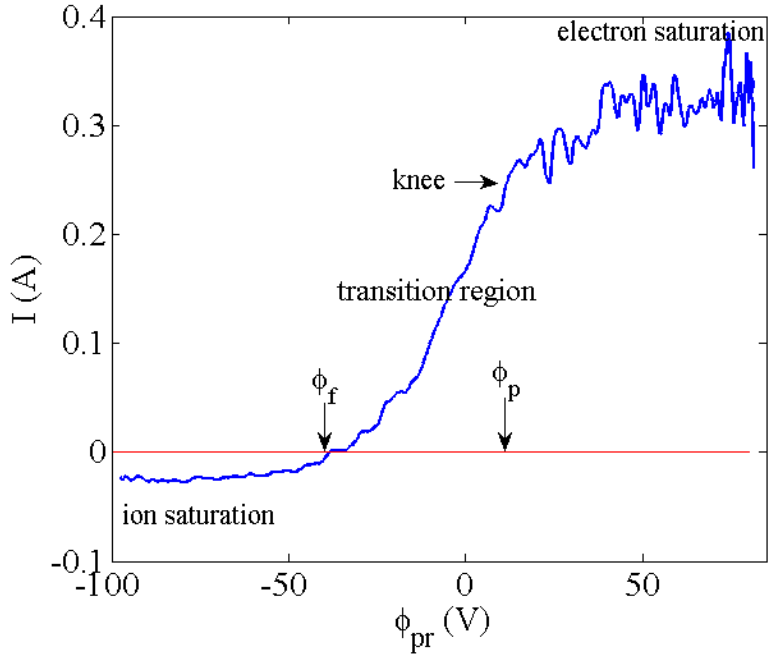

Figure 2.1 Particular case of a characteristic I-V curve of a Langmuir probe in a TJ-II NBI heated plasma discharge. The three regions (ion saturation, transition and electron saturation) are indicated.

At sufficiently large negative values of the probe bias, the electrons will be repelled and the measured current (I_{sat}) is only due to the ions, known also as *ion saturation current* (I_{sat}):

$$I_{sat} = \frac{1}{2} n_0 e c_s A_{pr} \tag{2.2}$$

where A_{pr} is the collection area of the probe and n_0 the density far from the probe (Fig. 2.1).

By biasing the probe less negatively with respect to the plasma potential the sheath potential drop is reduced and a larger fraction of the electron distribution are collected by the probe. Assuming a Maxwellian distribution, the electron current (I_e) will depend on the probe potential (Φ_{pr}) with respect to the plasma potential according to the Boltzmann factor:

$$I_e = \frac{1}{4} n_{es} e c_e A_{pr} \exp\left(\frac{e(\Phi_{pr} - \Phi_p)}{kT_e}\right) \tag{2.3}$$

Where $c_e$is the random thermal electron velocity $c_e = \sqrt{8kT_e/\pi m_e}$. As the probe bias exceeds the plasma potential, the sheath disappears and the electron saturation current is controlled by the random electron flux, leading to the electron saturation current, $I_{sat,e}$. As seen in figure 2.1, current exhibits a knee after bias potential Φ_{pr} exceeds the plasma potential Φ_p.

$$I_{sat,e} = \frac{1}{4} n_{es} c_e A_{pr} \tag{2.4}$$

The floating potential may be calculated by equating the ion and the electron currents to give the following result:

$$\Phi_f = \Phi_p + 1 + \frac{kT_e}{2e} ln\left(2\pi \frac{m_e}{m_i} \frac{T_e + T_i}{T_e}\right) \tag{2.5}$$

II.1.1.3. Langmuir probes techniques in fusion plasmas

Langmuir electrical probes are one of the most reliable diagnostics for obtaining certain plasma parameters such as electron temperature and density, plasma potential and electron energy distribution function. Usually, in laboratory experiments, during one plasma discharge, an ideally large number of *I-V* curves are performed, leading to statistical estimations of plasma parameters. In general, time resolution of electrical probes is limited by its cut-off frequency, $f_{cut} = \frac{1}{2\pi} R_{sheath} C_{stray}$, where $R_{sheath}$is the Resistance of the sheath and $C_{stray}$is the stray capacitance due to the electrical probe circuit. The spatial resolution of electrical probes is given by the sheath thickness, this is, the distance between two probes must be large enough to avoid sheath overlapping.

In some conditions it might be difficult to use a single Langmuir probe due to the absence of a defined potential reference. This problem can be overcome by choosing the reference electrode to be of similar size and shape and positioned close to the probe. This is the so-called *double probe method* that consists of two probes, generally of equal area.

By adding a third electrode in the close proximity to a double probe, the *tripe probe configuration* is obtained. The standard triple probe is the combination of a double probe and a third electrode. The third electrode is used to measure the floating potential while the other two, in a double probe configuration, are biased with a constant potential such that one tip draws an ion saturation current ($I_1 = I_{sat}$) and the other a net electron current ($I_1 = -I_{sat}$). The potential of the electron collecting element (Φ^+) will adjust itself to draw an equal but opposite current to the ion side. Given $I_1 - I_2 = 0$, the electron temperature may be obtained from:

$$\frac{kT_e}{e} = \frac{\Phi^+ - \Phi_f}{\ln(2)} \tag{2.6}$$

The principal advantage of the triple probe is that the ion saturation current, floating potential and electron temperature can be measured simultaneously with high (in the range of milisecond) time resolution. However, it should be noted that the triple probe technique gives a non-local

measurement of T_e due to the spatial (typically a few mm) separation between the probes. As a consequence a phase difference appears between probe measurements that does not allow quantifying high (in the range 10 - 100 kHz) frequency T_e fluctuations. Different improvements have been developed leading to the so-called modified triple probe technique and also to other innovative configurations, as shown in references [78] and [79].

II.1.1.4. Probe configurations of interest

Given that large amounts of probe data are collected during typical plasma discharges, it is essential the development of analysis tools for the efficient analysis and interpretation of measurements.

Power spectra and cross-correlation. The standard linear power spectrum analysis is commonly used for analyzing the distribution of fluctuation power over frequencies. The nonlinear interaction can be analyzed using the bicoherence method [80]. The level of similarity between two signals can be quantified by the cross-correlation coefficient. The coherence between two signal x(t) and y(t) is defined as:

$$C_{XY}(f) = \frac{|G_{XY}(f)|^2}{G_{XX}(f)G_{YY}(f)} \tag{2.7}$$

where $G_{XY}(f)$ is the cross-spectral density between *x(t)* and *y(t)*, and $G_{XX}(f)$ and $G_{YY}(f)$ are the auto-spectral density of *x(t)* and *y(t)* respectively. The coherence function gives information about the extent to which *x(t)* can be predicted from *y(t)* and it has a value from 0 to 1.

Two point correlation technique. With two points measuring floating potentials or ion saturation currents, two- point correlation [81] can be used for the analysis of phase velocity, wavenumber and correlation length. This is known as the *two point correlation technique*. The phase difference between to signals separated by Δx provides the value of wavenumber $k = \Delta\varphi/\Delta x$. The fluctuation power in frequency and wave-number domain is given by $S(k,\omega)$. The phase velocity of fluctuations is ω/k, but it has to be weighted with $S(k,\omega)$:

$$v = \frac{\sum_{k,w}\left(\frac{\omega}{k}\right)S(\omega,k)}{\sum_{k,\omega}S(\omega,k)} \tag{2.8}$$

Three point measurements: It is possible to calculate turbulent particle flux by using three Langmuir probe tips. This is achieved by setting two probe tips along poloidal direction measuring V_f and one tip placed on between of them measuring I_{sat}. From the two probes measuring V_f is possible to obtain the poloidal electric field, which is related to the radial particle transport:

$$\Gamma_r = \langle \tilde{n}_e \tilde{v}_r \rangle = \frac{\langle \tilde{n}_e \tilde{E}_\theta \rangle}{B} \tag{2.9}$$

where $\tilde{E}_\theta = (\tilde{V}_{f1} - \tilde{V}_{f2})/d$, being d the distance between the two probes.

As it will be described latter, the building of more complex probes, able to host tips following certain spatial configurations of interest, are useful to measure interesting quantities such as radial profiles of potential and/or I_{sat} , Reynolds stress components of electrostatic fluctuations and, if the probes are placed at distant positions along the device, they are an useful tool to detect global fluctuation.

II.1.2. Langmuir probes in the TJ-II stellarator

TJ-II has three access ports enabled for the installation of Langmuir probes arrays [82]. Four different arrays of Langmuir probes have been used, three of them are multi-probe arrays and are installed in the two positions shown in figure 2.2 and the other one is a probe working as an electrode biasing in the plasma edge.

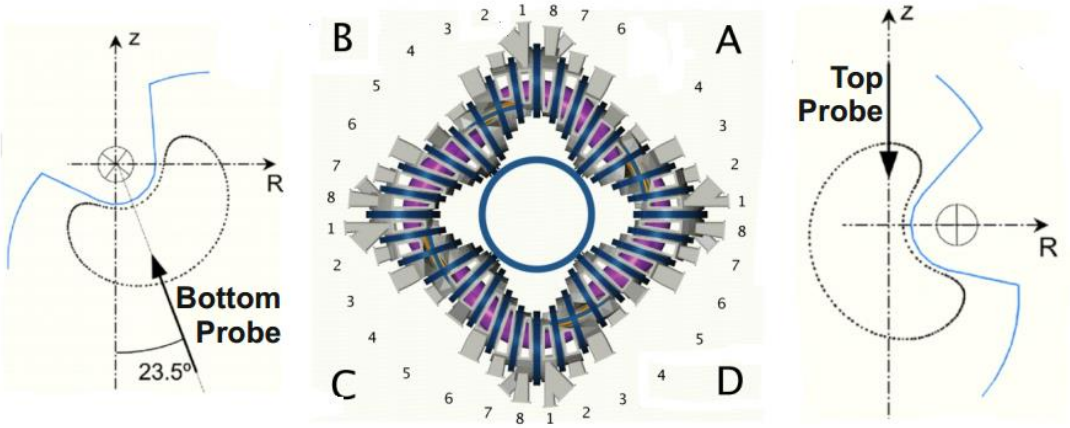

Figure 2.2 Relative poloidal and toroidal positions of access ports for probes in the TJ-II stellarator.

In TJ-II, the reciprocating system mainly includes two parts: a removable probe head and a displacement system, which enables the probe to be displaced in vacuum. The probe displacement system has two components: a slow one to set the probe at the initial measurement position and a fast one (run length = 0.1 m) to obtain the desired measurements within an adjustable time interval during the plasma discharge. The spatial resolution of the radial movement is about 1 mm. The fast displacement (up to 2 m/s) is achieved by using a pneumatic system.

Electrode biasing is a technique for externally modifying the edge electric field. When a biased electrode with respect to wall or limiter is inserted into the plasma edge, radial electric fields are induced by cross-field currents. Electrode biasing experiments play an important role in the demonstration of the causality relation between radial electric, transport and Zonal Flow dynamics [see chapter III].

In TJ-II, a 2D carbon composite mushroom-shaped electrode (12 mm high with a diameter of

25 mm) has been installed [81]. The electrode is screwed to a stainless steel shaft, which is protected by boron nitride as insulating material to be exposed to the plasma. The electrode is manipulated by a fast reciprocating probe drive. It can be biased (up to 350 V) with respect to the wall or one of the two limiters located in the Scrape-Off Layer region (about 0.5 cm beyond the LCFS). The electrode can run in DC, DC+AC mode. Various shapes of waveform can be used for the biasing voltage, for example, sine, triangular and square. The frequency of the waveform can be in the region 1-500 Hz, with resolution of 1 Hz. (See figure 2.3)

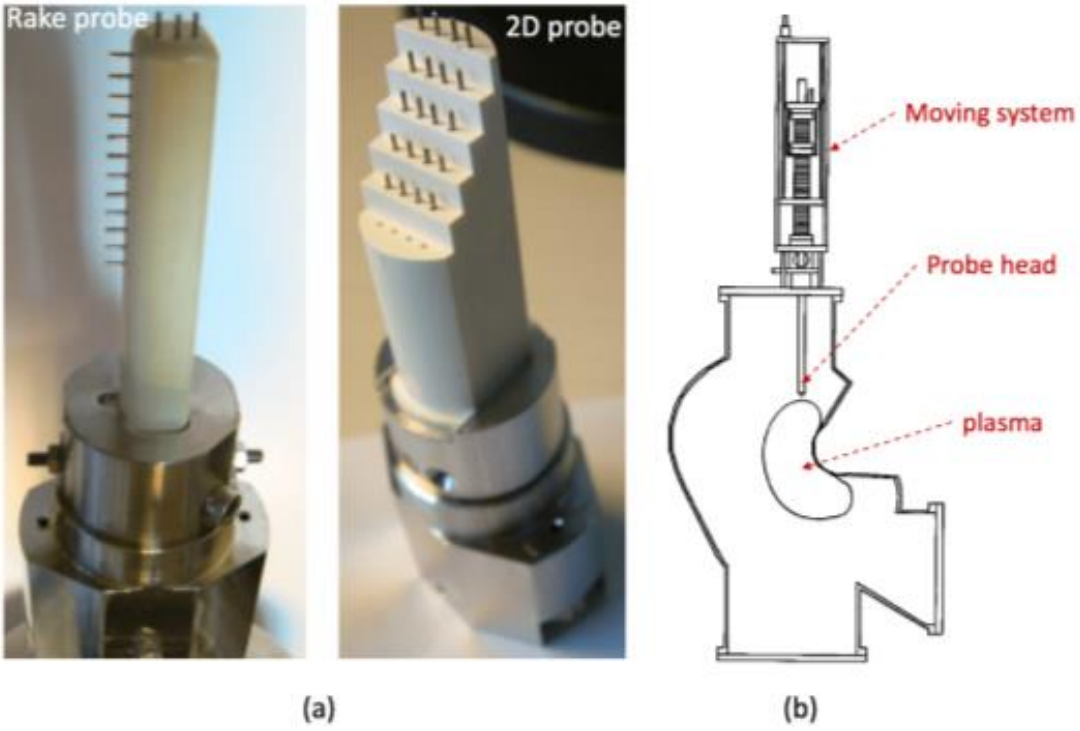

Figure 2.3 Images of two of the probe rakes installed at the TJ-II stellarator (a). Schematics of the external biasing probe installed at the TJ-II stellarator (b). Courtesy of Bing Liu.

II.2. Diagnostic and Methods for Recycling studies in JET

In the present study we compare ion and neutral fluxes at the JET divertor target to assess the Recycling and its influence on the SOL plasma. The ion fluxes reaching the wall and/or the divertor of a burning plasma device can be collected by negatively biased electric probe (see previous section I.1). The neutral fluxes can be obtained spectroscopically by measuring the emission from recycled neutrals re-entering the plasma thereby changing their atomic population equilibria. Therefore an atomic model is necessary that will be described in the next sections together with the hardware used for the emission measurement.

II.2.1. Sources of Visible light in fusion devices

Atomic line emission of visible light from electronic transitions

As introduced before, the existence of atomic excitation and de-excitation processes leads to spectral emissions. Following the classical electromagnetic theory, the atomic emission lines are classified according to their wavelength, λ. The simplest and first empirical relation between emission lines and spectra is the Rydberg formula [83]:

$$\frac{1}{\lambda} = R_H \left(\frac{1}{2^2} - \frac{1}{{n_f}^2} \right) \tag{2.10}$$

where $R_H = 1.09677581 \cdot 10^7 m^{-1}$ is the Rydberg constant [82] and n_f is a natural number higher than 2. The first explanation of this empirical relation was given by the semi-classical model proposed by Niels Bohr [84]. According to this model, electrons, which orbit around the nucleus, occupy stationary energy levels and emit electromagnetic radiation once they transit between allowed orbits. The frequency of the emitted electromagnetic wave is given by the Planck relation:

$$\left| E_f - E_i \right| = h\nu \tag{2.11}$$

where E_f and E_i are the corresponding energies of the final and initial orbits, respectively, ν is the frequency of the emitted electromagnetic wave and $h = 6.626 \cdot 10^{-34} Js^{-1}$ is the Planck constant. Assuming that momentum and energy of orbiting electrons are quantized, the Planck relation has been obtained for the case of an electronic transition between n>2 orbit and n=2 orbit:

$$h\nu = |E_n - E_2| = \frac{4me^4}{32\pi^2 \epsilon_0^2 \hbar^2} \left(\frac{1}{4} - \frac{1}{n^2} \right) = R_H \left(\frac{1}{4} - \frac{1}{n^2} \right) hc \tag{2.12}$$

where $\hbar = h/2\pi$ is the reduced Planck constant. The inferred value of R_H is very close to that which had been deduced from the Rydberg formula.

The energy and angular momentum of electrons is quantized and its description is given by the Hamiltonian (developed theory on this topic is well described in reference [85]).

In the case of Hydrogen atoms (and Hydrogen isotopes), the electrons interact only with photons and change their orbits by spontaneous and stimulated emission or by photon absorption. The number of photons emitted by a volume of particles (Hydrogen atoms) which transit between two given electronic states, labelled as *i* (initial) and *f* (final), is known as the emissivity of a spectral line and is expressed by the local emission coefficient:

$$\epsilon_{if} = \frac{1}{4\pi} n_f A_{if} \tag{2.13}$$

where n_f is the density of particles in the final excited state and A_{if} is the transition probability of a particle from the excited to the ground state, also known as the Einstein coefficient. The relation between the particle density at states with different excitation levels is given by the relation between excitation induced by impacts of electrons and emission to lower excitation states. The number of particles in excited states depends on electron temperature, T_e, which appears implicitly in the emission coefficient as the convolution of the excitation cross section σ_{exc} with the electron energy distribution ν_e:

$$\epsilon_{i,f} = \frac{1}{4\pi} nBn_1 n_e \langle \sigma_{exc} \nu_e \rangle \tag{2.14}$$

where $B = A_{i,f} / \sum A_{i,f}$ is the branching ratio, being $A_{i,f}$ the Einstein coefficients (give the probability of a reaction). In the case of atomic Hydrogen, the radiative transitions from *i* >*2* to *f* = *2* are known as **Balmer transitions** (see table 2.1):

Name	Initial orbit	Final orbit	λ (mm)
H_α	3	2	656.3
H_β	4		486.1
H_γ	5		434

Table 2.1: Values of wavelength of electromagnetic emission associated to electron transitions to n=2 orbit.

In the table 2.1 are shown transitions to n=2. Electronic transitions from n=3 to n=2 lead to the emission of electromagnetic radiation in form of photon in the visible range, with an associated wavelength of $\lambda = 656.3\, mm$, which is in the visible range. Interestingly, the H_α transition, from n=3 to n=2, has an Einstein coefficient, $A_{3,2} \approx 4 \cdot 10^7 s^{-1}$, which is the most intense in the Boundary plasma.

In the case of atoms with more than one electron the situation is more complex due to the electron-electron interaction, in addition to the simplest case of Hydrogen, in where the electron interacts only with photons.

Black-body emission in plasma

The material surfaces facing the plasma, such as divertors and limiters, experience an increase in their temperature due to the received power fluxes and, as a consequence, emit continuum Black Body Radiation with a spectrum given by the Planck's Law (see figure 2.4). It is known that there is an inverse relation between the maximum of emission wavelength λ_{max} of a black-body and its temperature [86]. This is stated by the Wien's displacement law:

$$\lambda_{max} = \frac{b}{T_{body}} \tag{2.15}$$

where T_{body} is the temperature of the material and b on the Wien constant. Note that for surfaces with T > 1000 ºC the fraction of light in the visible region at large wavelengths is considerable and can be seen by the naked eye.

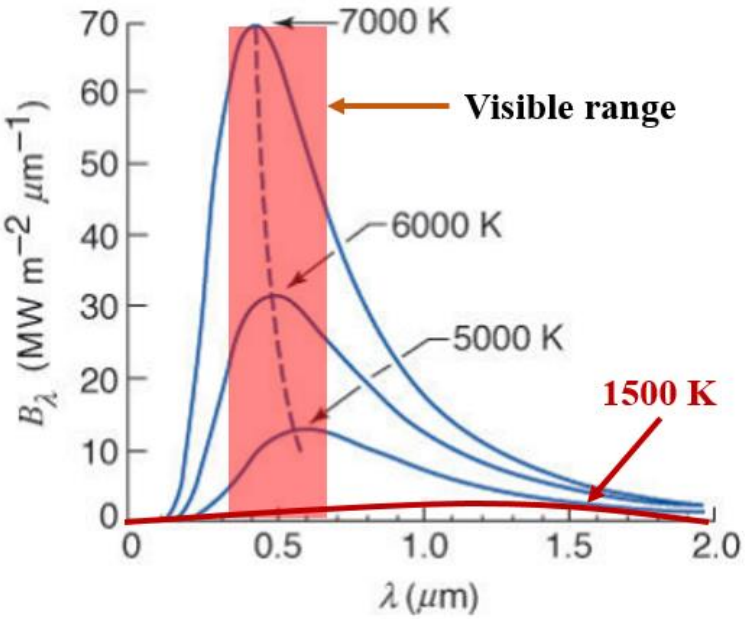

Figure 2.4 Wien's displacement Law. In red, the approximation of a curve for the case T=1500 K.

Bremsstrahlung radiation

In addition to the aforementioned sources of visible light in fusion plasma, which is generally dominated by the H_α atomic line (see figure 2.5), there is other contribution manifested as continuum emission level (spread along the entire spectral range) of radiation due to the deceleration of electrons when they become deflected by ions [87]. The intensity of Bremsstrahlung radiation is proportional to $n_e^2/T_e^{1/2}$ and is only important in very high density plasmas ($n_e > 10^{20} m^3$). In our case it can be neglected. This kind of radiation is present not only in fusion plasmas but also in other systems, good examples are the radio emission from ionised winds or the X-ray emission from clusters of galaxies[88].

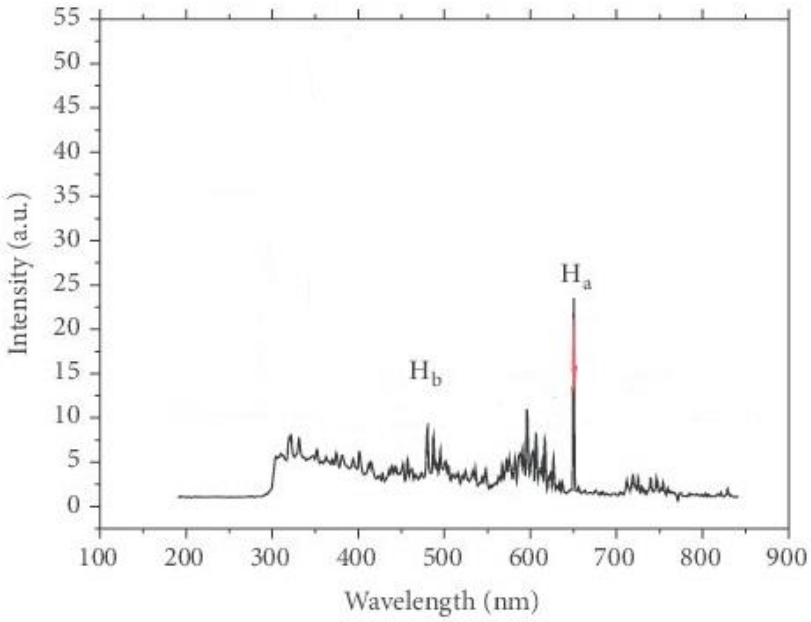

Figure 2.5 Example of the intensity of spectral plasma emission in function of the wavelength in fusion plasmas. From http://jes.ecsdl.org/content/159/2/H121/F2.expansion.html

It should be noted that the conditions existing in the Boundary plasma $(1\ eV < T_e < 1\ keV)$ favours the atomic lines of table 2.1 in this region.

II.2.2. Atomic models for the description of fusion plasmas

Optical emission spectroscopy gives information of population states of atoms (and ions). The excitation and de-excitation processes which take place in plasma can be inferred from population models in function of plasma parameters. Thus, electron density and temperature are determined from the line radiation induced by electronic transitions of the species which constitute plasma. Figure 2.6 shows a very simple representation of a model which includes different electronic levels as well as excitation and de-excitation processes which could occur in a Hydrogen atom. The labels "*p*" and "*q*" refer to excited energy levels while "*g*" indicates ground energy level. It also shows that the ionization threshold is one step above the highest excitation level as it leads to the "extraction" of the electron from the atom.

Depending on the value of plasma electron density, three different excited population models are used to describe excitation and de-excitation processes: local thermodynamic equilibrium model, corona model and collisional-radiative model [89]:

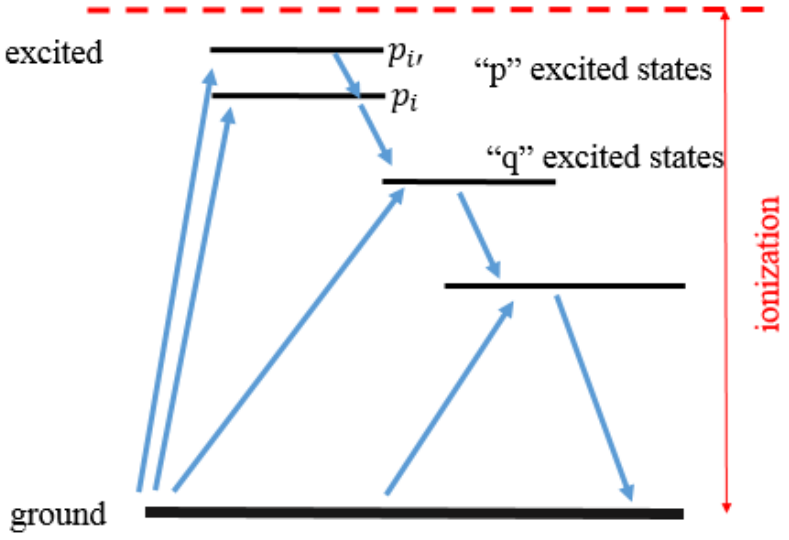

Figure 2.6 Schematic diagram of the possible electronic states and transitions in an atom of Hydrogen. p_i, $p_{i'}$ and q correspond to excited states. The ionization level is above all the excited states.

1. Local thermodynamic equilibrium model

In a quasi-neutral plasma, the temperature of the species (ions, electrons and neutrals) is given by their kinetic temperature and is defined by:

$$T_s = \frac{1}{3} m_s \langle v_s^2 \rangle \tag{2.16}$$

where m_s and v_s are, respectively, the mass and the velocity of the specie denoted as "s" and the angular brackets mean the average over an ensemble of particles. Then, the average kinetic energy of the species is taken as the value of the kinetic energy of the ensemble.

For very high electron density plasmas ($n_e \geq 10^{24} m^{-3}$), the high level of electron-ion collision leads to an equilibration of temperatures: $T_e \approx T_i$ and the population of electrons follows a maxwellian distribution of energy. So, the plasma is in *thermodynamic equilibrium*: collisional and radiation processes are in equilibrium with their corresponding inverse processes, which is known as **detailed balance**. In this case, the spectral radiation from plasma follows the Planck distribution:

$$I_\upsilon = \frac{2h\nu^3}{c^2} \frac{1}{\exp\left(\frac{h\nu}{k_b T}\right) - 1} \tag{2.17}$$

If the plasma remains in thermodynamic equilibrium the density of **excited states** of species follows the Boltzmann distribution:

$$\frac{n_q}{n_p} = \frac{g_q}{g_p} \exp\left(\frac{-(E_q - E_p)}{k_B T}\right) \tag{2.18}$$

In where $n_{q,p}$ is the density of the excited states q and p, and $g_{q,p}$ is the probability of the states q and p.

On the other hand, the density of **ionization states** is given by the Saha equation:

$$\frac{n_{i+1} + n_e}{n_i} = 2\frac{Q_{i+1}}{Q_i}\left(\frac{2\pi m_e k_B T}{h^2}\right)^{\frac{3}{2}} exp\left(\frac{-(E_{i+1} - E_i)}{k_B T}\right) \quad (2.19)$$

where n_i is the density of atoms in the "i" state of ionization, Q_i indicates their corresponding degeneracy and E_i is the amount of energy needed to remove electrons in order to ionize an atom to a state "i" (see fig. 2.6).

The temperature *T* is the same for all plasma species in the case of thermodynamic equilibrium, then the velocity of all species which form the plasma follows the Maxwell-Boltzman distribution:

$$f(v_r) = 4\pi\left(\frac{m_r}{2\pi k_B T}\right)^{\frac{3}{2}} v_s^2 \exp\left(-\frac{m v_s^2}{2k_B T}\right) \quad (2.20)$$

However, in the case of fusion plasmas, the electron density is $n_e \ll 10^{24} m^{-3}$ and ion temperature T_i is typically lower than electron temperature T_e, which leads to different amounts of energy transferred from one specie to the other during collisions. In this case plasma does not remain in thermodynamic equilibrium, being the particle dynamics is dominated by electrons via excitation and de-excitation processes driven by electron collisions.

2. Corona model

In much lower electron density plasmas ($n_e \leq 10^{17} m^{-3}$) it is assumed that the transitions of electrons to upper states occur always due to electron collisions from the ground level while tansitions to the ground state are accompanied by radiative decay (spontaneous photon emission). This is known as the **corona model**. In this low density case the population density is fully dominated by the atoms and ions in ground state, n_g.

The most common excitation process in the Boundary plasma for Hydrogen atom is by electron collision:

$$H(g) + e^- \rightarrow H(p) + e^- \quad (2.21)$$

where $H(g)$is the Hydrogen atom in the ground level and $H(p)$ is the atom in the excited populated level, with p > g (see fig. 2.6). As pointed out before $H(g) \gg H(p)$. As the electron density is very low, the cross-section of electron collision excitation processes is very low. Then, the population densities n_p and the transition between two excited states are negligible. The spontaneous emission is the only de-population process which takes part during this regime. Assuming that the ground state atoms dominate, ($n_g \gg n_p$), the population density of the excited state n_p can be modelled by a differential equation :

$$\frac{dn_p}{dt} = n_g n_p X_{gp}(T_e) - n_p \sum_{g<p} A_{pg} \tag{2.22}$$

In equation 2.22, the first term in the right-hand side is the contribution to excited states n_p due to electron collisions, being n_g the ground state density and $X_{gp}(T_e)$ the excitation rate coefficient, which depends of the electron temperature. The second term accounts the decreasing in the excited state population density, n_p, which is purely due to spontaneous emission. The spontaneous emission rate is given by the Einstein coefficient A_{pg}.

To obtain population densities is necessary to integrate equation 2.22, however, considering that excitation and de-excitation rate are equal (stationary conditions), the equation 2.22 can be solved as a simple algebraic equation and the population density of excited states is:

$$n_p = \frac{n_e n_0 X_{gp}}{\sum_{g<p} A_{pg}} \tag{2.23}$$

From 2.23 is obtained the population coefficient, which relates the population density of ground and excited states:

$$R_{gp} = \frac{n_p}{n_e n_g} \tag{2.24}$$

Again, fusion plasmas stay out of this regime because the relevant plasma regimes for fusion are characterized by electron densities of, at least, two orders of magnitude larger than those which are explainable by corona models. Corona model is able to explain lower density plasmas [90] such as electrostatic discharges or electric arching around objects. As explained in the coming lines, the dynamics of population /de-population processes in fusion plasmas is more complex.

3. Collisional radiative model (CRM)

For intermediate values of electron density ($10^{17}m^{-3} < n_e < 10^{24}m^{-3}$) the population density of excited (n_p) and ionized states gains importance with respect to the population density in ground state (n_g). In addition to the balance between electron collision excitation from the ground state and spontaneous emission de-excitations (the only processes that governs corona model), also other processes play a role. The most relevant ones are the following, based on figure 2.6:

- Electron collision excitation from states p_i to states $p_{i\prime}$, with $i' > i$.
- Electron collision de-excitation from $p_{i\prime}$ to p_i with $i' > i$.
- Spontaneous emission from $p_{i\prime}$ to p_i, with $i' > i$.
- Ionization from excited states p_i.

- Radiative recombination from ionized particles to ground state g and to excited states p_i (accompanied by photon emission).

The first CRM was stablished in 1972 for atomic Hydrogen, by Johnson and Hinnov [91]. Collisional Radiative Models include ionization, recombination and radiation processes and have been applied in a wide range of scenarios, e.g. ionized air mixtures [92], ionospheric plasmas generated in the surface of spatial re-entry vehicles [93], among others. More general models have been proposed for plasmas, including hot plasmas for nuclear fusion applications [94 and there in].

This thesis is framed in the study of the edge region of magnetically confined plasmas in medium and large-size nuclear fusion devices, where the electron density ranges from $n_e \approx 10^{18} m^{-3}$ to $n_e \approx 10^{20} m^{-3}$. Then the use of CRM is considered as the most appropriated to determine the population densities in this scenario. Depending on electron temperature, plasma is dominated by recombination reactions (for $T_e < 1\ eV$) or fully dominated by ionization processes (for $T_e > 10\ eV$). When $1\ eV < T_e < 10\ eV$, the two processes coexist (see fig. 2.7). As a consequence, for example, for a Hydrogen atom, the evolution of the excited state n_i population density is described by this model:

$$\frac{dn_i}{dt} = \sum_{i\prime<i} A_{ii\prime} n_{i\prime} - \sum_{i\prime<i} A_{ii\prime} n_i + n_e \left(\sum_{i\prime\neq i} X_{i\prime i}(T_e) n_{i\prime} - \sum_{i\prime\neq i} X_{ii\prime}(T_e) n_i + (\alpha + \beta n_e) n_+ - S_i n_i \right)$$

(2.25)

where n_i and $n_{i\prime}$ are the population densities of two excited states which are coupled between them. Again, $X_{ii\prime}(T_e)$ are the rate coefficients (Einstein coefficients) in function of the electron temperature. The right hand terms of the equation correspond to: spontaneous emission (two first terms), electron collision excitation and de-excitation (two first terms in the parenthesis), recombination and, the last one, ionization.

The population density of the different levels can be inferred from the resolution of equation 2.25. The most complicated aspect on it its solution to infer the value of cross-sections of collision ionization, excitation and recombination processes as well as the value of the Einstein coefficients linked to the spontaneous emissions. From the value of population densities, the intensity of emission lines is calculated making use of:

$$I_{if} = n_f A_{if} \tag{2.26}$$

The relation between ionization and recombination rate and the dynamics of neutral particles in plasma edge can be theoretically predicted from collisional-radiative model [95, 96, 97].

II.2.3. Retrieving neutral fluxes from photon fluxes: Atomic physics factor

When neutrals recycle at a surface, they will all become ionized in their path towards the plasma, however a fraction of them will be excited before being ionized, emitting photons (figure 1.12). So the neutral flux F^0 can be related to the photon flux $\Gamma_p$by a spectroscopic system which must be absolutely calibrated for Radiance ($L^{D\alpha}$), as represented in figure 2.7. In JET this is done for the divertor using the $D_\alpha$line (see II.2.5).

The number of neutral atoms and molecules entering the plasma and that are ionized following different reactions can be related to the fraction of them which are excited and emit photons in their paths towards plasma. This is done by the definition of a coefficient called S/XB [98, 99]. The S/XB coefficient gives the number of ionization events per emitted photon, known also as the emission efficiency, and is defined to link the photon flux dN_p/dt to the neutral flux F^0.

Given a material in contact with plasma, the neutral particle flux F^0released from its surface, with an area A is given by:

$$F^0 = \frac{1}{A}\frac{d\, n_0}{dt} \tag{2.27}$$

where n_0 denotes the number of neutrals. The number of photons emitted from a volume of particles which are being ionized is predicted from the collisional radiative model. The emitted photons per unit of time by the volume are calculated by integrating the emission coefficient $\in$ of the responsible spectral line over the volume and multiplied by 4π because of the homogenous character of emission:

$$\Gamma_p = \frac{1}{A}\frac{dN_p}{dt} = 4\pi \int \in dV \tag{2.28}$$

The ratio of the photon flux to the neutral flux is the following:

$$\Gamma_r = \frac{\partial N_p/\partial t}{AB}\frac{S}{X} \tag{2.29}$$

where S and X are the total ionisation and excitation rate of neutral atoms and molecules, respectively. S/(XB) is known as inverse photon efficiency and relates the photon fluxes to particle fluxes (gives the number of neutral ionization events per emitted photon). B is related to the spectral band of the observed light. Then, having an absolutely calibrated diagnostic, the neutral flux can be inferred from:

$$F^o = A\ 4\pi\ S/XB\ L^{D\alpha} \tag{2.30}$$

where $L^{D\alpha}$ is the emission radiance, obtained empirically, A is the area covered by the diagnostic (see figure 2.7) and the factor 4π is used because the photon emission from a volume of plasma is isotropic. (fig. 2.7)

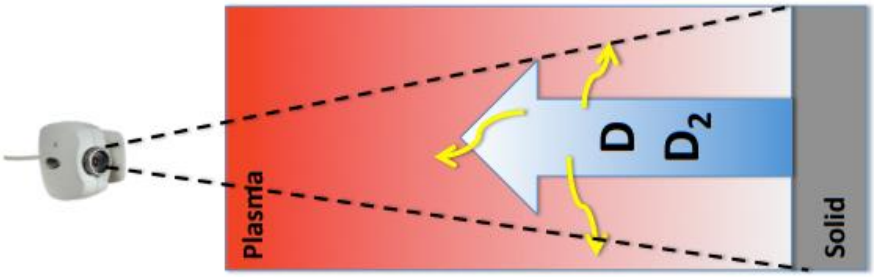

Figure 2.7 Representation of a spectroscopic diagnostic collecting photon emission from a volume of neutrals which are being ionized and excited.

S and X are obtained from the Collisional-Radiative Model. Figure 2.8 shows the dependence of S/XB on T_e and n_e for the H_α-line [95]. We can see that it has a very week dependence on the temperature for $T_e > 10\ eV$and on density for $n_e < 10^{19} m^{-3}$ (figure 2.8). In order to correctly estimate the neutral particle flux from the H_α-line emission, plasma must be in ionizing conditions. When $T_e < 10\ eV$, as recombination play a role or even dominate over ionization, the assumed hypothesis for ionization cross-section is not correct [95].

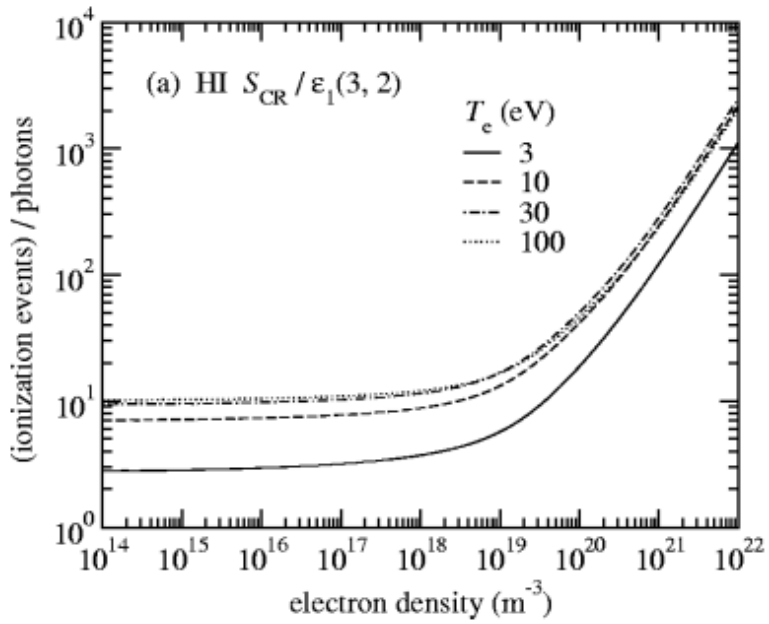

Figure 2.8 Dependence of the S/XB coefficient on electron temperature and density. Taken from reference [95].

II.2.4. KL8A visible fast camera system

In the last decades the fast development of digital imaging allows the observation of 2-dimensional fast phenomena with a speed of up to 10^7 frames per second. Fast viewing systems are already installed in the main magnetic confinement fusion devices such as the case of Alcator C-Mod [100], NSTX tokamak [101], ASDEX – U [102], JET [103], LHD [104] and the TJ-II stellarator [105].

The most important fields of application of fast visible systems are the study of edge turbulence [106], dynamics of runaway electrons from disruptions [107], measurements of electron temperature and pellets propagation and ablation [65]. As seen in the figure 2.9, the KL8A system is placed at JET sector 7 and is looking at sector 8. The aperture of the endoscope's optics was defined so as to have a wide-angle view of JET Vacuum Vessel, placed at the KL7 IR endoscope [108] as seen in figure 2.10.

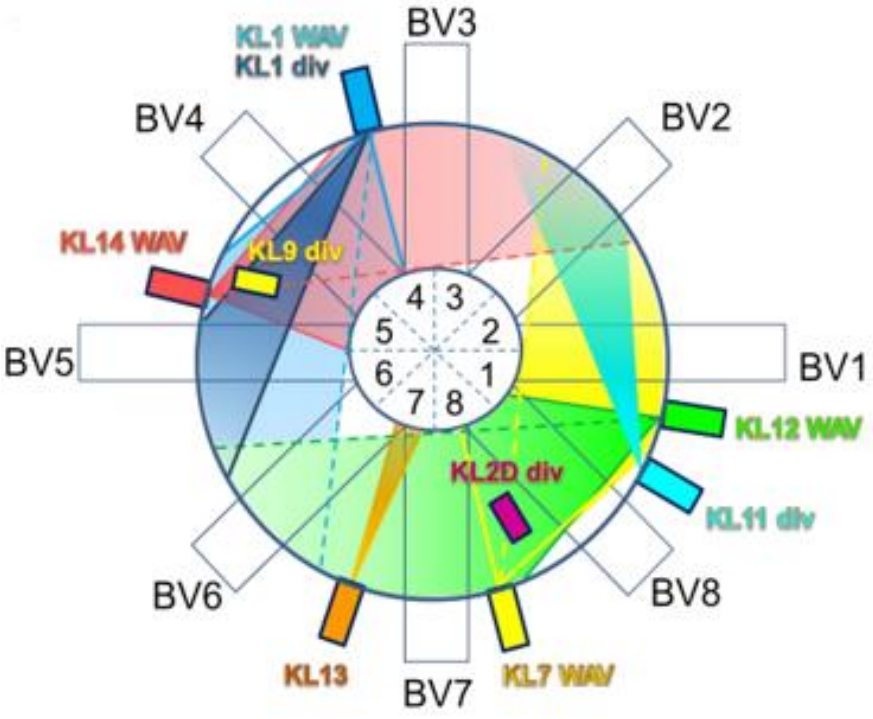

Figure 2.9 Situation of the KL7-IR endoscope in JET, at JET sector 7, among other viewing systems. This image is courtesy of Valentina Huber.

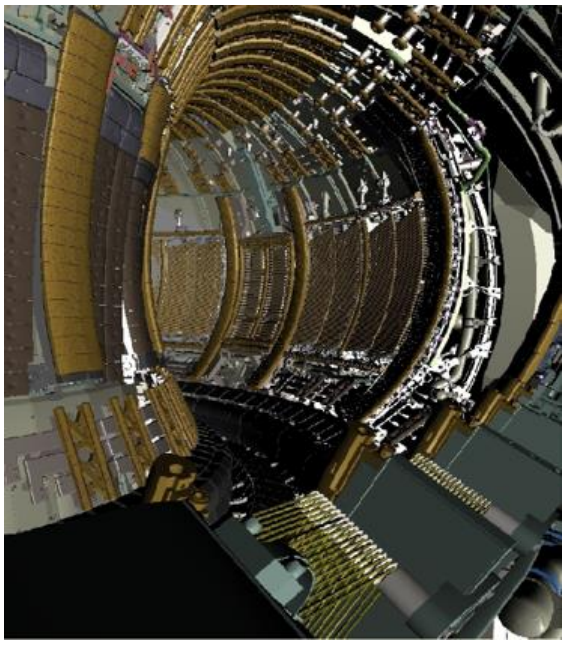

Figure 2.10 CAD reconstruction of the wide-angle view of the vacuum vessel (sector 8 of JET). The black structure in the base of the vacuum vessel is the JET divertor. In the center of the figure is seen the RF antenna also. Courtesy of Adriana martin de Aguilera.

II.2.4.1. Viewing optics and filter wheel

The visible light coming from the KL7 Endoscope is transported with the help of mirrors towards the KL8A Fast camera, as seen in the figure 2.11.

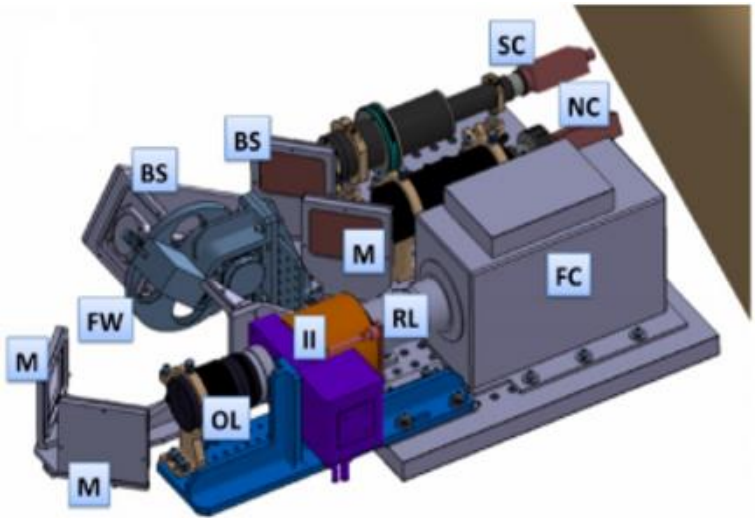

Figure 2.11 BS: Beam-spliter; M: Mirror; FW: Filter Wheel; SW: Slow Camera; NC:NIR Camera; OL: Objective lens; II: Image intensifier; RL: Relay Lens; FC: Fast Camera.

In the reference [108] is explained in detail how the light is transported to the Endoscope and to KL7 system. A Beam-splitter diverts a fraction of about 30 % of the light to a Protection camera (labelled as slow camera in the figure 2.11). In the optical path, a Filter Wheel allows for the spectral filtering of the visible light [109]. Band-pass filters are used to select spectral bands of interest for a given experiment. In JET, filters are installed along a filter wheel which has five positions and is remotely controlled through Newport NCS200 engine. A list of filters is shown in table 2.2:

Species	Wavelength (nm)	FWHM (nm)
D_α	656.19	1.0
Berilium II	527.1	1.0
Bremsstrahlung	538.35	3.0
Argon II	610.9	1.0
EMPTY	Visible spectrum	

Table 2.2 List of filters used in the fast visible camera installed at JET. Reference: https://www.andovercorp.com/products/bandpass-filters/semi-custom-bandpass-filters

II.2.4.2. Fast camera and Image Intensifier

Hamamatsu Image intensifier unit C9548-03:

Due to the ultra-fast videos, the exposure time is extremely short, the photon flux is low and the image needs to be intensified in order to increase the signal to noise ratio. Then, a two stage *image intensifier* (Hamamatsu model C9548-03BL) is used. The first stage is a GEN II adjustable intensifier coupled to a GEN I fixed intensifier. As GEN I has a lower saturation level than GEN II, this last can be operated at lower currents. In addition, the system auto-shuts down when the intensity of integrated light reaches a certain threshold. These properties allow a safe operation of the system.

The principle of operation of these devices is explained in the following lines: In GEN II intensifier, photons are converted to electrons in a photocathode by photoelectric effect and then are accelerated by an adjustable electric potential within a microchannel plate (the range of the potential is in between 600 and 800 V). Then electrons are converted again to photons in a phosphor plate and are conducted by optic fibre until GEN I intensifier, in which the light is conducted through an electron accelerating tube under a fixed electrical gain of 50 V. In consequence, the system provides a linear response to the amount of incident light as well as with the magnitude of the accelerating potential applied in the GEN II intensifier. The Image Intensifier has a linear response with both exposure time and acceleration potential.

Photron fast camera

It is a camera with a maximum resolution of 1024×1024 pixels. It can reach minimum exposure time of 1 μs and it produces 8-bit videos from a 10-bit CMOS sensor with 17 μm pixels. It can take images with a speed up to 250 kHz by reducing the useful area of the sensor. The most relevant parameters in the setting of fast viewing systems are the *frame rate* τ_f and the *exposure time* τ_{exp}. The frame rate gives the number of frames taken per second while the exposure time is the time that the sensor is collecting incident light. The frame rate is related to the time resolution of the system while the exposure time gives the higher speed event which can be captured by the sensor. The image is a result of integrating the incident light along the exposure time. In order to properly observe the dynamics of the plasma phenomena it is required that $1/\tau_{exp}$ is always higher than or equal to the speed of the observed phenomena. Finally, the exposure time is shorter than the entire length of the frame. The rest of the unused frame time is known as dead time (white space in fig.2.12). In the figure 2.12 is shown a diagram of the set-up of the fast camera and the Image Intensifier (II).

The Camera triggers the II: When the II is in active mode light is amplified and transmitted to the Fast Camera, else no light. Then, II acts as the shutter of the system. The exposure times of the II (τ_{II}) are shorter than those of the Camera (see figure 2.12).

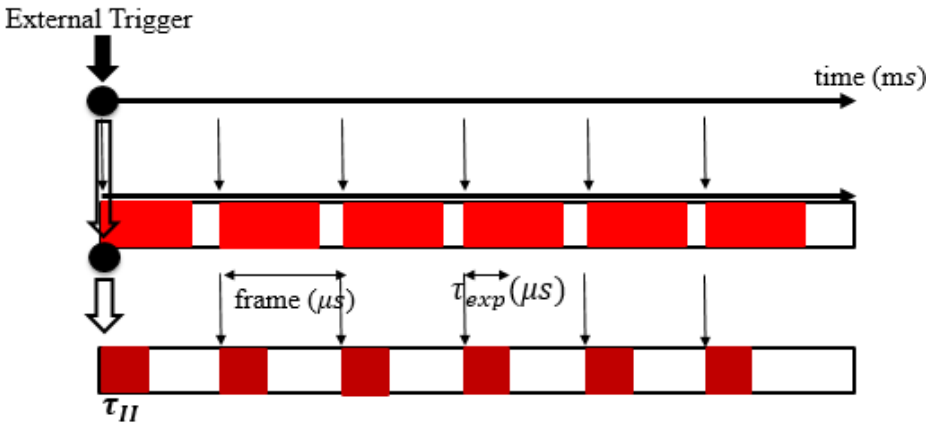

Figure 2.12 Diagram of time operation of fast camera. The exposure time τ_{exp} is shorter than the duration of the frame. The dead time is represent as the white space after the exposure time.

Sensing technologies

There two technologies that can be used to collect light and transform to electric signals: first, CCD sensors (Charged Coupled Device), in where pixels are p-doped MOS capacitors. MOS (Metal Oxide Semiconductors) diodes conduct electric current in inverse once photons collection begins. Then, a device is used to quantify the electron charges passing through the semiconductor-oxide interface. On the other hand, CMOS technology consists of an array of pixels integrated within a circuit. Each pixel has its own photodetector and amplifier. The data

is read in parallel with respect to the matrix of pixels, which increases the speed input to output with respect to the CCD sensors. CMOS sensors are more adequate at the moment to be used in fast visible imaging in fusion plasmas also because this technology is more resistant to radiation damage.

The spatial resolution of KL8A has been estimated and has a value of:

$$1\ px^2 = 4\ cm^2 \tag{2.31}$$

KL8A diagnostic has still an important open issue to be solved. Within the image intensifier, electrons are accelerated between to plates by an electric field. In the endoscope, where the image intensifier is placed, the magnetic field is of about 0.7 T. If a change is produced in the magnitude of the magnetic field it will finally cause a twisting in the electrons trajectory, following the Lorentz Law. This leads to a spatial rotation in the video frames. At the present this is a problem that is not fully solved. In spite of this limitation, KL8A has demonstrated its value as diagnostic in the study of a wide range of phenomena in JET, as for example:

1) *Observation of ELM's*: KL8A provides two dimensional data of the dynamics of ELM instabilities in the divertor. The speed or frames per second can reach up to 70 kHz with exposure times of the order to 1 μs.

2) *Disruption mitigation:* The camera can be used to collect the whole amount of light generated once the mitigating gas impacts the plasma during disruptions. The maximum speed is of about 20 kHz, constrained by the full sensor image needed to collect all the radiation produced. It is possible to use filters in order to infer the Argon emission during the disruption.

3) *Pellet observation:* The high temporal resolution at which KL8A is able to work makes possible to of detect and study pellets during their trajectory inside plasma, from the moment they are injected until they collapse after ablation process.

4) *Impurity transport:* As explained before, it is possible to use a filter in order to collect only visible light emitted in a desire wavelength spectral region. Usually filters are used to look at the transport of Berilium inside the JET vacuum chamber. The exposure time is increased up to values close to 1 ms in order to collect enough amount of light.

II.2.5. Divertor D_α-spectroscopy and Langmuir Probes at JET

There are radially distributed along JET divertor 36 Langmuir Probes (squares in figure 2.13). In each position, each probe is able to infer ion flux through ion saturation current. LP describe IV sweeping curve between +30 V and -140 V every 2.4 ms and with an acquisition rate of 100 kHz [110]. Signals provided by LP are discontinuous time series formed by groups of points

with a duration of about 2ms each one, which corresponds to the saturated ion branch of each IV curve. Then, ion saturation current is provided with $10\mu s$ time resolution.

During ELM's the biasing may be insufficient to repel electrons, which can have parallel energy in the order of 1 keV in the pedestal of JET [111]. However, the measured values of temperature during ELM's are of the order of 30 eV, which is low enough to allow the repulsion of electrons and measure realistic values of ion saturation current [110]. JET diagnostics provides two types of measurements from divertor Langmuir probes: first, local measurement of ion saturation current at each probe position along divertor and, second, integrated measurement of ion saturation current in both inner and outer divertor region. In addition, the values of both local and integrated values of current are transformed to measurements of ion flux.

In figure 2.13 are indicated the positions of the LP along the divertor, together with the D_α spectroscopic lines.

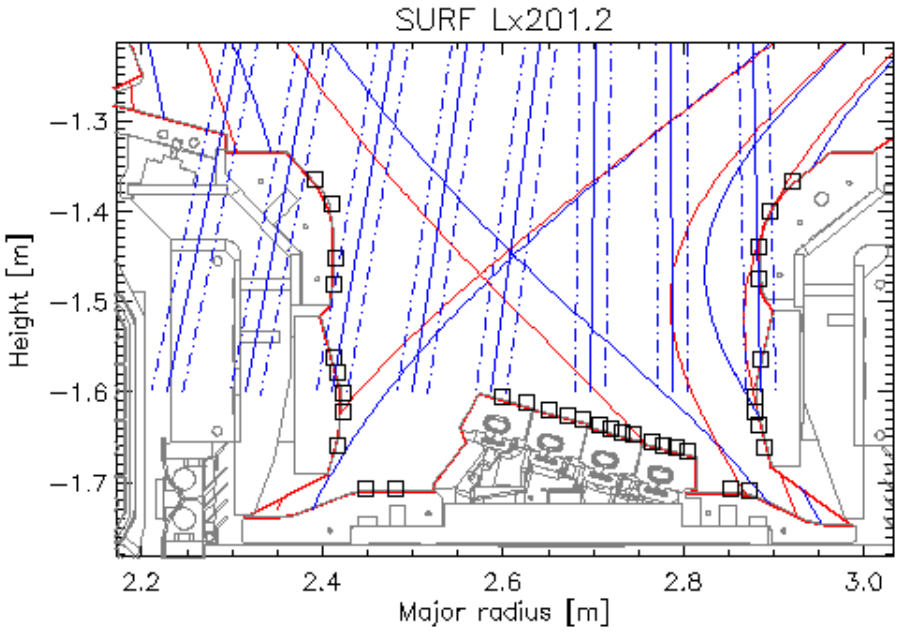

Figure 2.13 Black squares represent the position of Langmuir probes along the tiles which form divertor. The vertical blue lines represent the D_α chords.

On the other hand, from top of JET vacuum vessel, there are twenty D_α spectroscopic channels looking at the divertor region. The frequency resolution of these channels is of 10 kHz, which is enough to track ELM´s. These channels cover all the divertor and are absolutely calibrated in order to measure D_α radiance and also BeII and WI emission the spatial position at which each spectroscopic line is measuring is well defined. Spectroscopic lines obtain measurements of radiance $L^{D\alpha}$ coming from a point placed in the divertor. Radiance emitted from a point is isotropic, but the spectroscopic lines recover radiance emitted through a given solid angel. Then, lines give values of radiance per second, per unit of area and stereo-radian, and, assuming toroidal symmetry, the measurement of neutral flux can be obtained at the position of the LP at

a given toroidal section of the divertor (see equation 2.30) and can be expanded along the whole divertor. The combination of the high speed of KL8A fast camera and the good spatial resolution of D_α lines allows trustable spatiotemporal studies of visible light emitted along the divertor, done by the "cross-correlation" technique [144].

III. EXPERIMENTAL RESULTS

In this chapter are described the results obtained. First section is devoted to the description of the different spatial scales of the radial electric field E_r and their effects and connections with the intensity and width of radial turbulence as well as the enhancement of Zonal Flow activity. Second, it is shown the empirical evidence of the presence of Zonal Flows during the L-H transition and its consequences. Then, in third section are described the last results concerning the spatial-temporal structure of Zonal Flows and its dependence on the plasma heating scenario, magnetic configuration and isotope mass ratio. Finally are described results obtained at JET tokamak concerning the effect of magnetic configuration on the conditions of the Scrape-Off Layer and the physics of the plasma-wall interaction.

III.1. Empirical relation between neoclassical radial electric field, turbulence and Zonal Flows in the TJ-II stellarator

The spatial and temporal evolution of the radial electric field E_r has been studied in the plasma edge of the TJ-II stellarator. The radial correlation length of turbulence $L_r$was characterized in detail by using Langmuir probes. The use of a dual system of Langmuir probe rakes allows also the identification and study of Long Range Correlations, which are taken as a proxy of Zonal Flow-like structures. An empirical relationship between the intensity of neoclassical E_r, the radial correlation length of turbulence L_r and the amplitude of Zonal Flow activity was found together with different spatial scale lengths in E_r in TJ-II edge plasmas. The experimental findings show that the intensity and evolution of the two scales are strongly connected. In addition, the shearing rate of the short scale length E_r is comparable to the de-correlation rate of turbulence. This chapter is mostly based on the publication [112]:

III.1.1. Introduction

Zonal Flows in fusion plasmas

Zonal Flows manifest themselves as convective cells placed axi-symmetrically around the magnetic axis. Assuming that ZF are driven from the background turbulence, it is expected an enhancement of plasma confinement since ZF cause no cross-field transport. The radial structure of ZF is given by a quasi-sinusoidal feature whose wavelength covers a distance of about 10 – 50 times the ion Larmor radius [113]. This means in the order of 1 cm in the actual plasmas confined under ~ 1 Tmagnetic field. This size corresponds to the so-called *mesoscale*, larger than the *micro-scale*, which is defined by the ion Larmor radius, and shorter than the *macro-scale*, defined by the length of the machine minor radius. Assuming ZF as turbulence control element it is expected the observation of reduction in the turbulence level and radial particle transport. ZF manifest itself in the form of a large spectral power in the lowest frequency bands of the measured spectra[1] with has a global presence along the device.

Various works have reported the experimental detection of long-range correlations (LRC, see sections II.1 and III.1.2) consistent with the theory of "zonal flows", i.e., stable modes that are driven by turbulence and regulate turbulent transport [114 and references therein]. Zonal flows have been detected from the evaluation of LRC in plasma potential fluctuations by using Heavy Ion Beam Probe (HIBP) in core plasma and edge plasmas in the CHS helical system [115] and in the TJ-II stellarator [126] by using electrostatic probes, respectively. In the plasma edge the

[1] GAM's appear as sharp peaks at low frequencies, indicating low frequency coherent oscillations.

zonal structure was found by using mainly Langmuir probes [116, 117] and by phase contrast imaging in DIII-D [118]. More evidences of the detection of Zonal Flows by using a wide range of diagnostics can be found in the bibliography [119, 120, 121, 122, 123, 124, 125, 126, 127, 128, 129, 130]. The amplification of zonal flows by externally imposed radial electric fields has been observed both in tokamak and stellarator devices [131]. The coupling between long range correlations of the floating potential fluctuations and radial turbulent transport has been studied in TJ-II edge plasmas in earlier works [129, 130] and the driving and damping mechanisms of the $E_r \times B$ velocity associated with the zonal flows were discussed [132]. At present, the clarification of the relation between the growth of zonal flows and the development of transport barriers is an active area of research, with the goal of identifying the triggering mechanisms of the transition to improved confinement regimes [133].

Zonal Flows and radial electric fields

Radial electric fields play a key role in controlling transport in fusion plasmas. It is known that in quasi-axisymmetric or quasi-helically symmetric magnetic configurations, collisional plasma transport is intrinsically ambipolar. In non-quasi-axysimmetric magnetic field configurations, parallel viscosity and Neoclassical (NC) non-ambipolar fluxes determine the Neoclassical radial electric field on a much larger length scale than the gyroradius [134]. On the other hand, recent simulation results for tokamak plasmas have shown that multiple radial scale lengths on the electric field and pressure may develop, together with the spontaneous growth of long-lived patterns of $E_r \times B$ flows [135]. It is concluded that the E_r profile has a radial fine spatial structure (in the order of few ion Larmor radius). This quasi-regular, long-lived, self-organized and localized structure is spontaneously formed and is known as "$E \times B$ staircase". Direct observation of fine scale structures in radial electric fields have also been reported in the JET tokamak consistent with the stationary zonal flows [136].

Simulations have shown that the interplay between transport driven by turbulence and 3-D drift-optimized configurations could be explained on the basis of the reduction of turbulent transport by zonal flow generation [137]. The amplification of low frequency ZF-structures in plasma scenarios with reduced Neoclassical viscosity has been observed in TJ-II [138]. In addition, gyrokinetic simulations have shown that radial electric fields may affect the residual level of zonal flows in stellarators [139, 140]. Experiments performed in the TJ-II stellarator have shown that long range correlations detected in potential fluctuations, consistent with zonal flows, are amplified either by externally imposed radial electric fields or when approaching the L-H confinement edge transition.

In this chapter are described recent empirical findings on the relation between neoclassical radial electric fields, turbulence and Zonal Flows which have been found in the TJ-II stellarator.

III.1.5. Experimental set up and methodology

III.1.5.1. Plasma conditions

Experiments were done in ion root (negative electric fields), pure neutral beam injection (NBI) heated plasmas (700 kW port-through power at 33 kV) in the TJ-II stellarator (toroidal magnetic field $B \approx 1$ T, plasma minor radius $a \approx 0.20$ m). The experiments have been carried out within the "standard" magnetic configuration, in which the rational surface 8/5 is placed approximately in $\rho = 0.8$. This situation corresponds to iota = 1.6 in the plasma edge, as shown in figure 3.1.

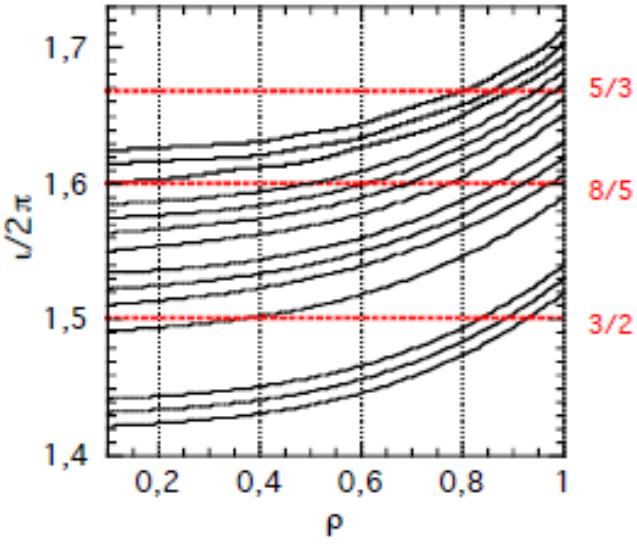

Figure 3.1 Radial profiles of plasma iota and rotational surfaces in the standard magnetic configuation of TJ-II stellarator. 8/5 rational surface is in the positioned in the plasma edge for magnetic configuration.

Four discharges (#36934, #36935, #36936, #36937) have been selected as a good sample for doing the data analysis due to its reproducibility. Line averaged plasma density is measured by laser two-color heterodyne interferometry [141]. On the other hand, H-alpha monitors placed at each sector of TJ-II stellarator are used to infer the ion flux reaching the walls. The ion flux is proportional to the H_α through the recycling coefficient. Density evolution is characterized by a characteristic rump-up developed as long as the NBI injection heats the plasma and until reaching the density limit, which happens at about $6 \cdot 10^{19} m^{-3}$.

III.1.5.2. Dual system of Langmuir probes: Long Range Correlation

The results reported here were obtained by the use of a detection system consisting of two Langmuir probe arrays, denoted as probe 1 and probe 2, located at two different toroidal/ poloidal ports, as shown in figure 3.2. The use of multi-Langmuir probes at different locations allows the simultaneous measurement of different plasma parameters and the assessment of their global and local characteristics. Rake probe 1 is installed on a fast reciprocating drive on top of the device (sector D). This probe consists of twelve Langmuir probe pins (measuring floating potential) with a radial separation of 3 mm, and three poloidally separated pins at the rake probe front edge, measuring the floating potential (Φ_f) and the ion saturation current (I_{sat}). The second probe (probe 2) is also installed on a fast reciprocating drive, located in a bottom port (sector B) entering the plasma in a region with higher flux compression than probe 1. This probe has eight probe pins separated by 2 mm, together with three poloidally separated pins at the top of the probe head. The sampling rate of the floating potential signals is 2 MHz. The two probe systems were used to study the temporal and spatial evolution of floating potential profiles, the radial correlation length of floating potential fluctuations and LRC in the edge of hydrogen plasmas.

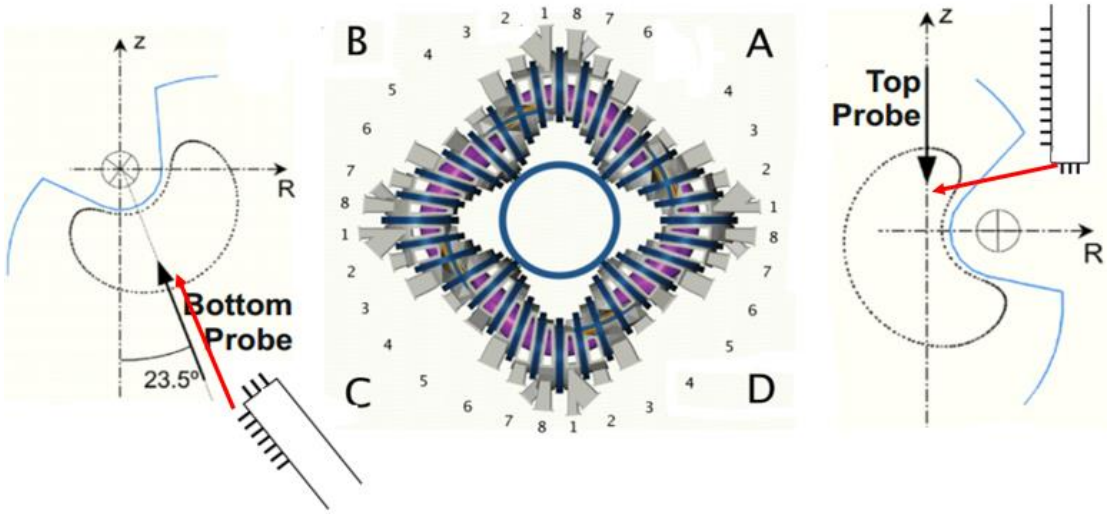

Figure 3.2 In the center, top view of the TJ-II stellarator, with the four sectors labelled. In the right is shown a schematic of probe 1, installed at top access port in sector D. The figure on the left represents the entrance of probe 2 through bottom port installed at sector B.

The position of the probe arrays with respect to the vacuum vessel walls is translated to ρ dimensions by using data from VMEC, which calculates the position of magnetic surfaces for the case of equilibrium plasma [142]. Previous results show that this method provides a reliable estimation for probe position in spite of the variation induced by the plasma current existent in TJ-II stellarator NBI plasmas [143]. Fig. 3.3 shows the feature of floating potential profiles

measured simultaneously by probes B and D during NBI TJ-II plasmas. As expected in ion root scenarios, floating potential values are negative in both probes and the values are comparable.

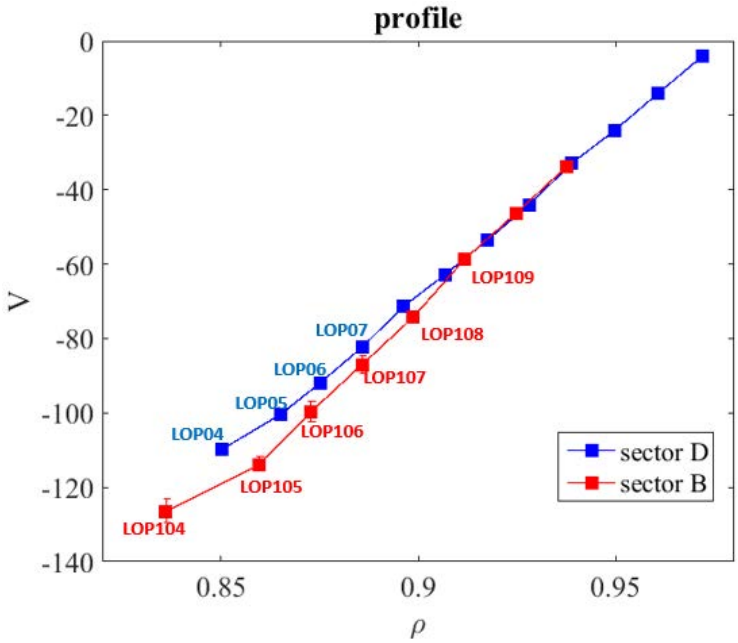

Figure 3.3 Radial profiles of floating potential averaged along the duration of NBI phase, measured at sectors B and D by Langmuir probes.

Long range correlations (LRC) in potential fluctuations, as a proxy of Zonal Flows, have been computed using probe LOP07 as a reference (Fig. 3.3). As shown in figure 3.4. LRC correlations are dominated by frequencies below 20 kHz with phase shift close to zero.

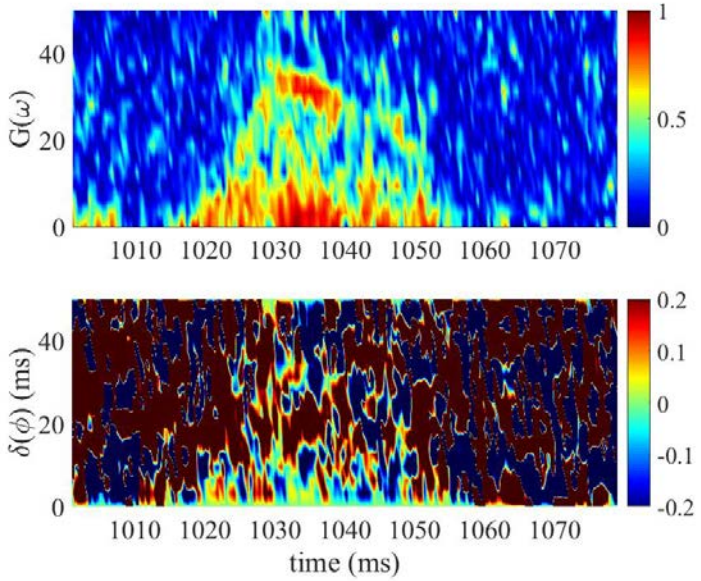

Figure 3.4 Above, cross-coherence calculated between distant probes: burst of high level of coherence is present at low frequency bands (f<20 kHz) for high levels of radial electric field. Below, the phase shift between signals approaches zero, pointing to the global character of the fluctuation.

As expected, the maximum in LCR have been observed for floating potential signals corresponding to probes LPO07 (system B) and LOP107 or LOP106 (system D) (Fig. 3.5).

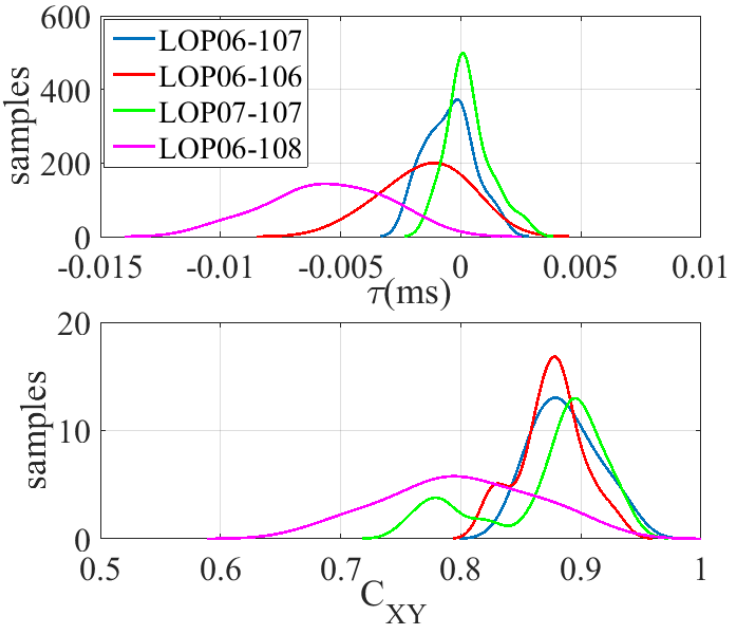

Figure 3.5 Above, distribution of points representing the time delay at which maximum of cross-correlation is found. For the case of LOP107-LOP07, most of the points are located at zero time delays, which corresponds to the detection of a global coherent fluctuation. Below, distribution of points in function of the maximum value of cross-correlation. In the case of LOP107-LOP07, the most probable value is 0.9.

III.1.2.1. Determination of E_r and its shearing rate

The perpendicular velocity of the plasma is described by equation 3.1:

$$v_{\perp} = \frac{E \times B}{B^2} - \frac{\nabla p \times B}{\rho B^2} \tag{3.1}$$

The first term in the right hand side is known as $E \times B$ velocity. Since it is charge-independent it does not produce any currents in the plasma with the exception the ones due to collisions. The second term is the diamagnetic velocity, which is charge-dependent and produces a current, known as diamagnetic current. The radial electric field is also obtained from the radial force balance equation for any specie:

$$E_r = \frac{1}{Z_i e n_i}\frac{\partial}{\partial r} p_i - u_{\theta i} B_{\varphi} + u_{\varphi i} B_{\theta} \tag{3.2}$$

where v_θ, v_φ, p and ρ are poloidal velocity, toroidal velocity, pressure and density. The first term in the right hand side of 3.2 is known as the diamagnetic contribution to E_r. For the case

of the TJ-II stellarator, it is demonstrated that the perpendicular velocity of fluctuations $v_\perp$ is dominated by $E \times B$ velocity [144].

This means that E_r can be estimated from the measurement of the $E \times B$ velocity. Empirically, $v_\perp$ can be inferred from the two point correlation technique, previously used in tokamaks [145] and stellarators [146]. In this work, the NC E_r is obtained by the gradient of Φ_p, which is aproximated by the gradient of Φ_f:

$$E_r = -\frac{d\Phi_f}{dr} \tag{3.3}$$

From the radial profile of Φ_f, measured in sector D by "probe D" (using 12 points along a radial distance of 30 mm), it is possible to obtain the value of NC E_r by a linear fitting over the values of Φ_f. The estimation of E_r from the two point correlation technique (by using the 2 probes placed at the probe head) is made for the four discharges (equation 3.3) and is compared with the result from the fitting of Φ_f. As seen in figure 3.6, the correspondence between the two methods is very good, which gives credibility to the calculation of E_r by the fitting method. Thus, gradients in floating potential are used from now as a proxy for radial electric fields.

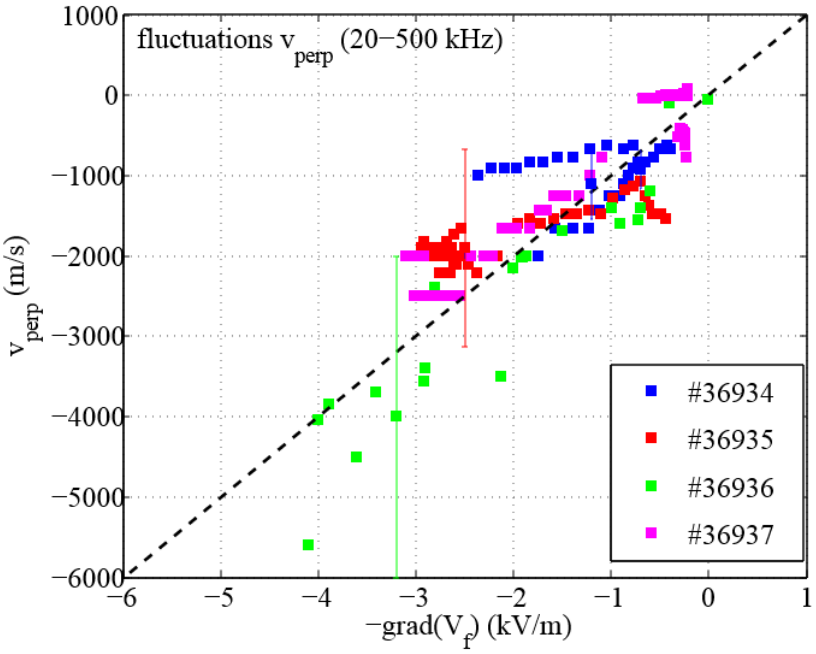

Figure 3.6 Perpendicular velocity of fluctuations measured by Langmuir probes plotted with respect to the gradient of floating potential. The evident good agreement between results obtained from both techniques allows to use the measured gradient in floating potential as the magnitude of radial electric field.

Concerning the determination of shearing rate due to E_r, it constitutes a more complex issue. In a first approach the second derivative of Φ_f could be considered and three points are needed to calculate $d\Phi_f^2/dr^2$. This "classical" method to calculate E_r shearing rate can lead to 7 local

measurements distributed along minor radious. However, in this study, the aim is to measure the magnitude of the shearing rate at different spatial scales, which requires a more elegant technique.

Then, the *scale-space representation technique* [147] has been implemented in order to obtain the shearing rate of E_r at different spatial scales. An inherent property of certain magnitudes or objects is that they only exist as meaningful entities over certain ranges of scale. Multi-scale representation of sensory data is of interest in the field of image processing as its purpose is to represent signals at multiple scales in such a way that fine scale structures are suppressed and a scale parameter *t* is associated with each spatial scale level in the multi-scale representation. The space scale is modulated by the use of a Gaussian Kernel, defined by a first order Bessel function, of a certain scale:

$$g(x,t) = \frac{1}{2\pi t} e^{-x^T x/(2t)} \tag{3.4}$$

If $L(x,t)$ is defined as the smoothed version of the original magnitude, *s(x)*:

$$L(x,t) = \int_{\alpha \epsilon \mathbb{R}^2} s(x-\alpha) g(\alpha,t) d\alpha = \int_{\alpha \epsilon \mathbb{R}^2} s(\alpha) g(x-\alpha,t) d\alpha = g(x,t) * s(x) \tag{3.5}$$

The parameter *t* is known as the *scale parameter* and gives the minimum scale of the features to be retained in the resulting image $L(x,t)$. On the other hand, α is the change of variable and represents the spatial scale of the convolution kernel $g(x,t)$. The differential value of $L(x,t)$is given by:

$$\partial_x^n \partial_y^m L(x,t) = \partial_x^n \partial_y^m \big(g(x,t)\big) * s(x) \tag{3.6}$$

Briefly, the properties of Gaussian Kernel are described: *g(x,t)* satisfies the non-enhancement of extrema principle, which means that local extrema can be smoothed only after the convolution. *g(x,t)* is a solution of the diffusion equation:

$$\partial_t g(x,t) = \frac{1}{2} \nabla^2 g(x,t) \tag{3.7}$$

$L(x,t)$ is equivalent to the evolution of a temperature profile with an initial condition of the form $L(x,0) = s(x)$. Huge progress has been done in the field of scale-space representation technique and its applications [148], mainly in the field of image processing, but it is perfectly applicable in 1 D problems. Actually, in our case, the spatial scale parameter α is related to the number of probe pins over which the calculation is made. In this case, we have chosen the central probe pin of probe D, labeled as LOP09 and $\alpha = -n{:}\,n$, with $n = 5$. This means that our spatial scale is from LOP04 to LOP14. The t parameter is modulated from 0.1 to 2, then the second derivative operator is wheighted along probe pins as shown in figure 3.7. This provides a proper scenario to calculate the effect of spatial scale in value of shearing rate of E_r,

but, measured in one point. At the end, the interesting magnitude is the value of $d^2\Phi_f/dr^2$ in $\rho \approx 0.9$.

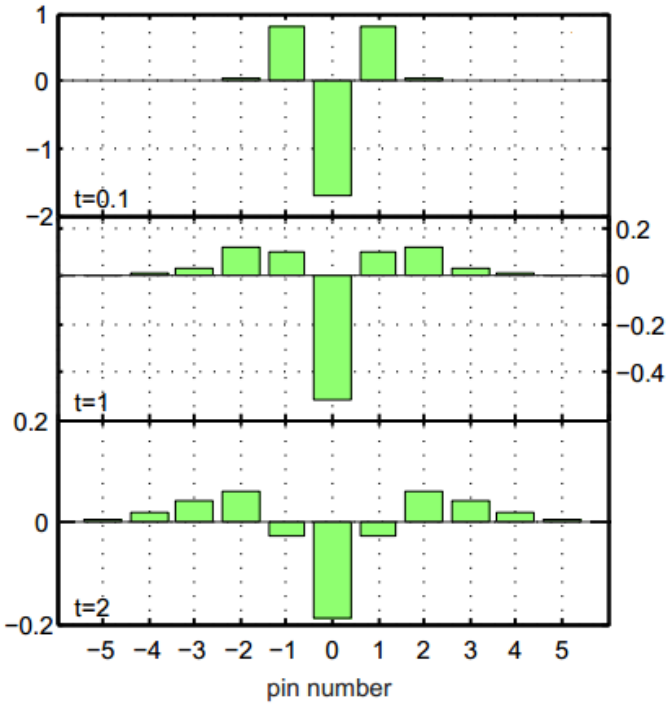

Figure 3.7 Weight of each spatial point in second derivative operator given by the parameter t.

III.1.3. Results and discussion

III.1.3.1. Neoclassical E_r and Long Range Correlations

The confinement time and density for the four discharges under investigation increase in the form of a ramp. As the density is ramped up, the negative radial profile of V_f steepens, reaching values close to 100 V (negative). At the same time the root mean square of fluctuations increases (fig. 3.8).

The mean velocity of fluctuations perpendicular to B along the magnetic flux surface is computed by the two point correlation technique in the laboratory frame of reference. In the plasma edge, the value of $v_\perp$ (in the electron drift direction) achieves values of the order of few kms^{-1}. The value of NC E_r, deduced from the gradient of V_f, matches the perpendicular velocity of fluctuations. This implies that the contribution of the pressure gradient to the perpendicular velocity is small under these conditions, consistent with the low beta of TJ-II

plasmas [149]. Gradient in floating potential is used from now as a good approximation for Neoclassical E_r. The calculation (linear fit of V_f radial profile) of NC E_r has been done along a distance of the order of ten times the ion Larmor radius. The deduced magnitude of E_r evolves to negative values and reaches values of 3 kVm^{-1} (negative), which is in quantitative agreement with previous NC calculations in TJ-II stellarator [138].

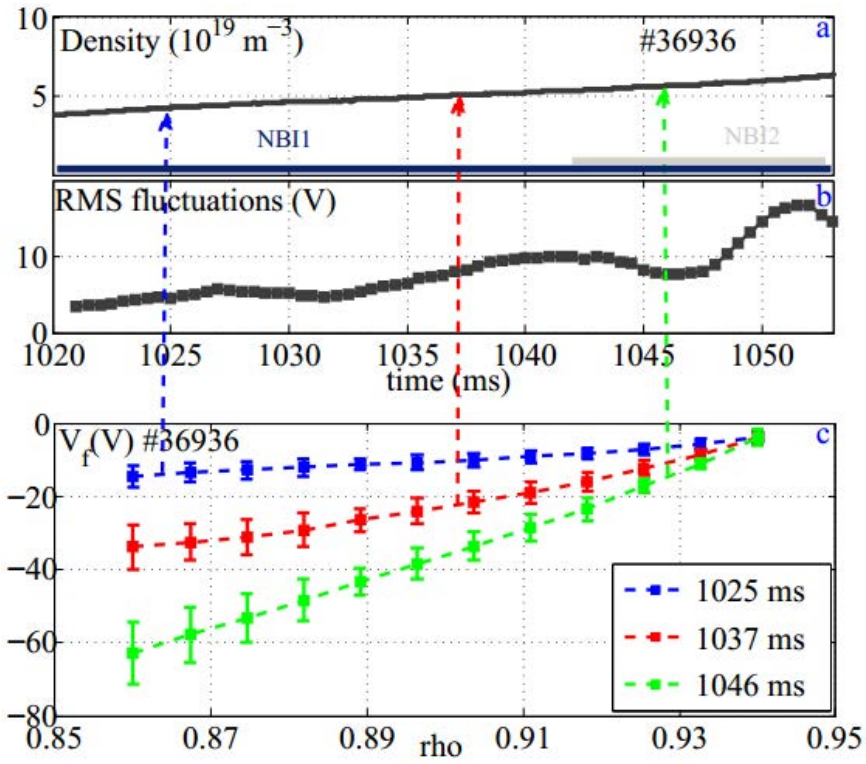

Figure 3.8 a) Temporal evolution of line averaged density and b) evolution of RMS of turbulence (low frequency). In c) are plotted the radial profiles of floating potential at different moments.

LRC are strongly dominated by frequencies below 20 kHz for all the analyzed cases. As NC E_r increases, the high toroidal cross-coherence appears for higher frequencies, which is in agreement with previous theoretical predictions [150]. This is a clear indication that ZF are relatively stationary for low values of NC E_r (concentrated at frequencies lower than 5kHz) and become more fluctuating for higher values of NC E_r (dominated by frequencies near to 20 kHz). In the figure 3.9 is shown the cross-coherence at low frequencies for the four discharges.

Cross-phase between distant signals LOP07 and LOP107 has values close to 0 in the four cases, confirming the existence of low frequency coherent oscillations (as shown in figure 3.10). As for the case of LR-coherence, the width of frequency coherent band increases with increasing NC E_r (fig. 3.11).

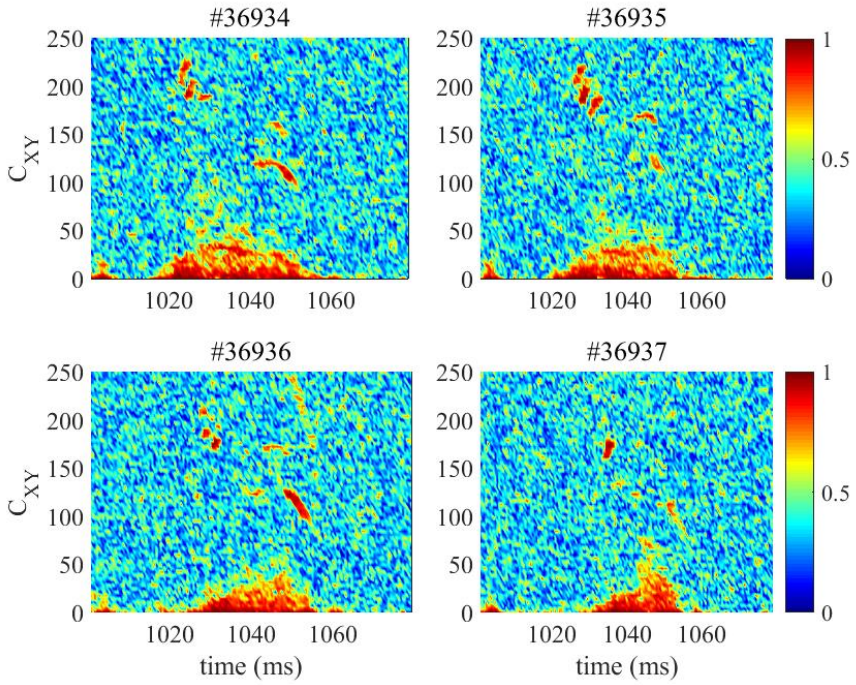

Figure 3.9 Evidence of long range coherence in floating potential for the four cases of study. The coherence is present in low frequencies (below 20 kHz).

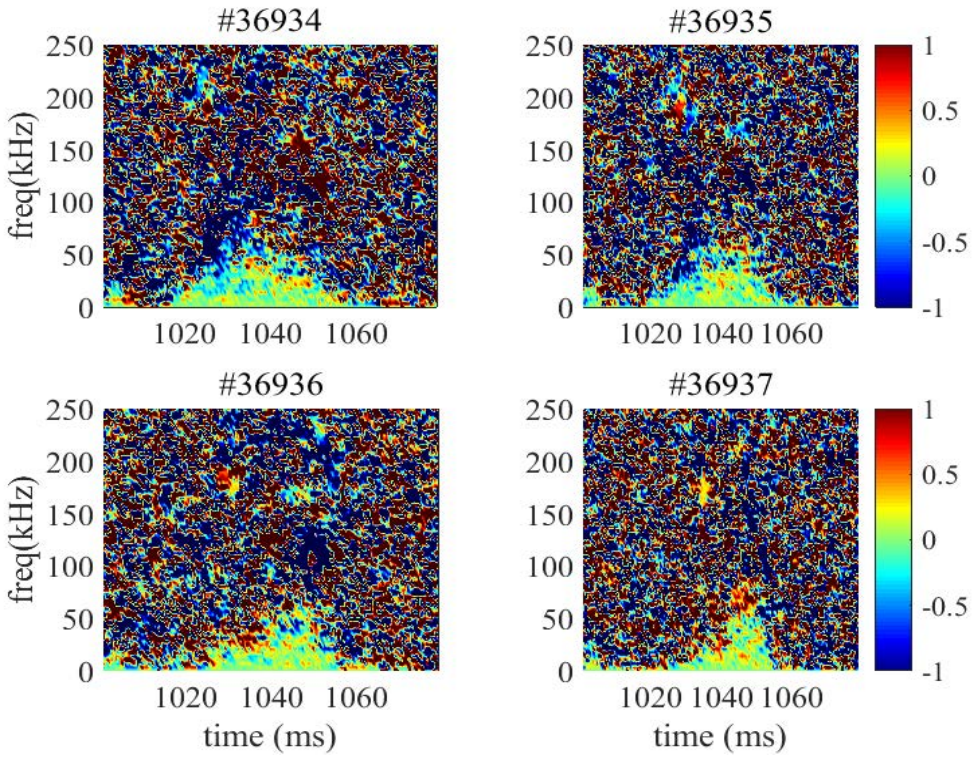

Figure 3.10 Cross-phase between distant electrostaic signals. Coincident with the large level of coherence, the cross-phase is close to zero, indicating zero phase delay between signals.

Interestingly, as mentioned, the high LRC appears also for higher frequencies as the radial electric field increases i.e. zonal flows become more stationary (dominated by frequencies below 5 kHz) in plasma regimes with small E_r and more fluctuating (dominated by frequencies below 20 kHz) as $|E_r|$ reaches values above 2 kV/m , as shown in figure 3.11 (a). We have also studied the influence of long radial scale (in the range of 20 ion Larmor radius) electric fields (denoted as NC E_r) on the radial scale length of the zonal flow-like structures. As shown in figure 3.11 (b), the radial scale length of LRC structures tend to decrease slightly with increasing NC E_r.

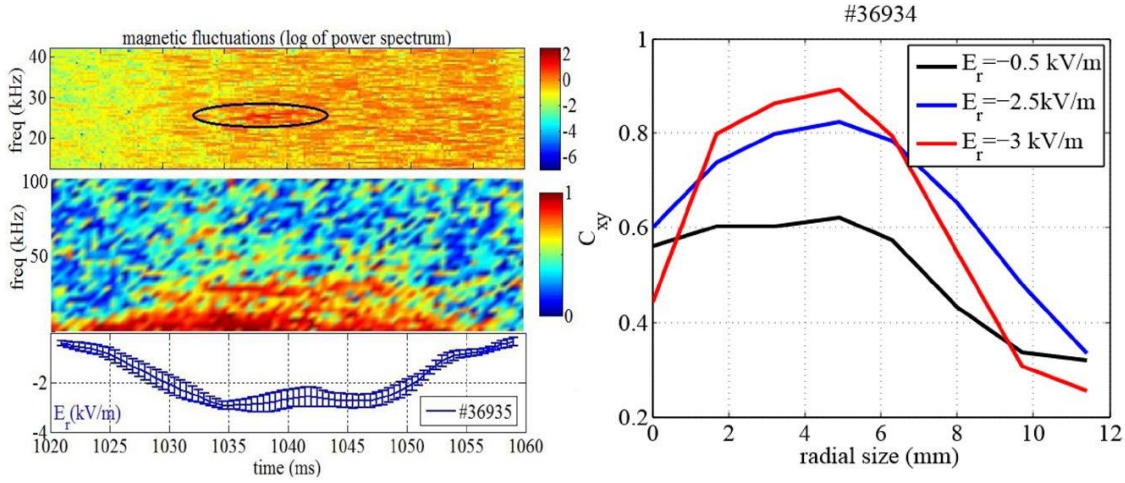

Figure 3.11 In the left is shown how the high level of coherence spreads across the frequency spectra as the radial electric field increases. In the right hand side, indications of the radial electric field reducing the radial size of the Zonal Flows.

Figure 3.12 shows the spatio-temporal Long Range coherence and cross-phase. On the other hand it is possible to represent the evolution along discharge time of the radial profile of the value of LRC for $\tau = 0$. The phase delay between signals strongly depends on the radial position, being constant at around $\rho = 0.9$ and increasing (negative or positive) as we move radially inwards and outwards.

The behavior of cross-phase along minor radius is highly reproducible, as shown in figure 3.13. Positive phase shift values mean inwards propagation whereas negative phase shift indicates outwards propagation. According to these criteria, the results on cross-phase can be interpreted as outwards propagation in the internal positions, no propagation in the central region, where the highest level of LRC is found (around $\rho = 0.9$), and finally, inwards propagation in the outer region (figure 3.13).

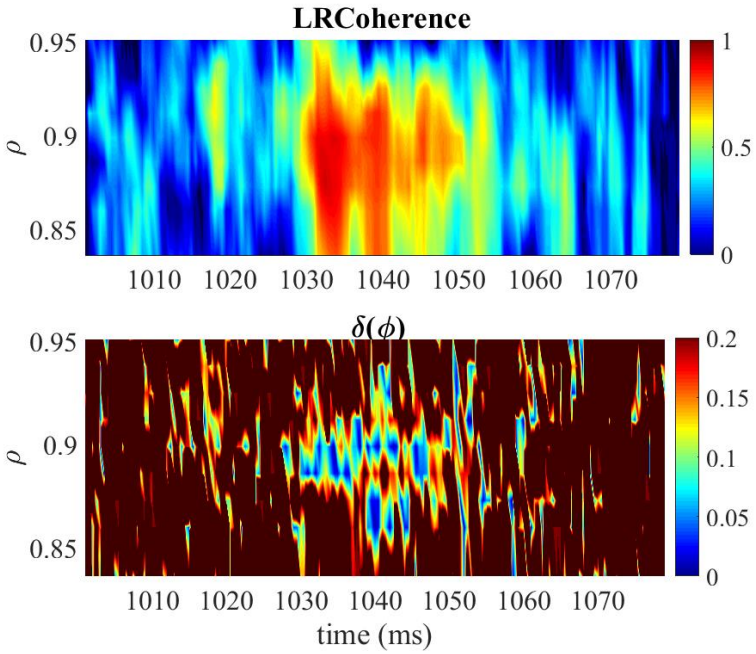

Figure 3.12 Above, spatio-emporal evolution of the LRC. LRC pattern is centered at $\rho = 0.9$ and decays radially. Below, spatio-temporal profile of cross-phase between distant signals: phase shift close to zero accompanies high levels of LRC, indicating the location of global coherent fluctuation. Data corresponds to TJ-II plasma discharge #36935

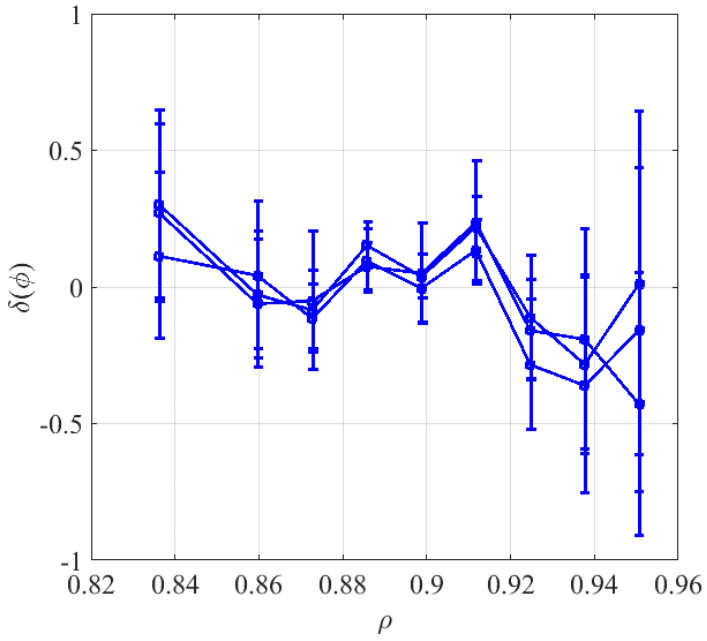

Figure 3.13 Time average along the duration of NBI heating phase of the phase shift between electrostatic signals measured at distant toroidal positions for TJ-II plasma discharges #36934, 35, 36, 37. The phase shift is close to zero along a radial region centered in $\rho = 0.9$

Finally, to point out the relation between E_r and LRC, in figure 3.14 is represented the level of LRC between reference signals (LOP07 – LOP107) with respect to the value of NC E_r. It is evident the existence of a clear empirical relationship between these two magnitudes.

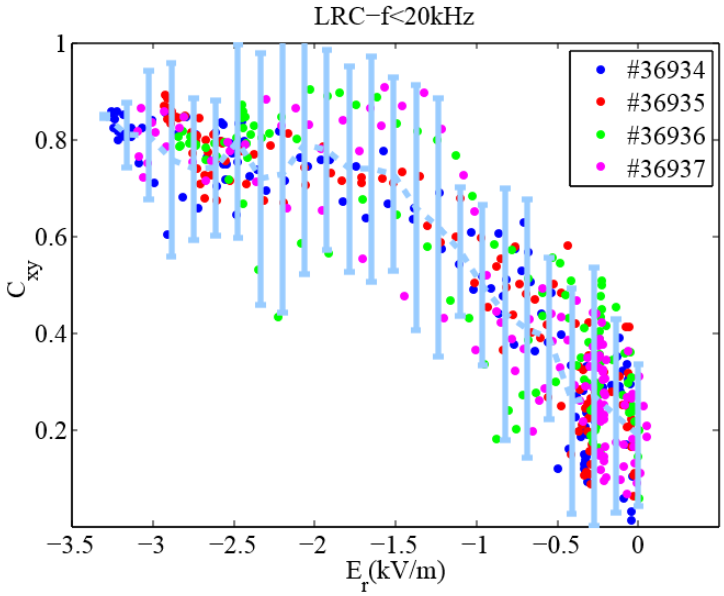

Figure 3.14 Level of LRC found between low frequency electrostatic fluctuations measured at two toroidal different positions in TJ-II. LRC is enhanced with the increase of NC radial electric field.

III.1.3.2. Radial Correlation Length of turbulence

The radial correlation length, L_r has been calculated using the twelve floating potential signals of "probe D", following its definition. L_r has been calculated for different frequency bands and it was found to be clearly dominated by low frequency (f < 25 kHz) fluctuations. $L_r$decreases by about 30-40% when the absolute value of NC E_r increases. This is due to the clear decrease of cross-correlation coefficient along radial distance when NC E_r reaches values above 2 – 2.5 kV/m. The higher frequency fluctuations, associated to local turbulent structures in the plasma edge, have much lower values of L_r, for both higher and ower values of E_r. These results are shown in figure 3.15. The most interesting result, which stablishes a direct empirical relationship between radial turbulence and ZF, is that for high values of NC E_r the measured width of radial turbulence corresponds to the radial size of ZF. This empirical result can be interpreted as the reduction in L_r until a certain value which mainly corresponds to the radial width of Zonal Flow. In both measurements, L_r and ZF width, the measured variable is a radial correlation length coming from the radial profile of cross-correlation. The first case is a pure radial measurement while in the second case is measured the radial profile of log range cross-correlation. In absence of turbulence and presence of a Zonal fluctuating structure, the value of the width of Zonal Flows and the result of L_r is the same because it is actually accounting the radial width of ZF and is not clear whether the term $L_r$can be attributed to the radial turbulence.

On the other hand, when turbulence spreads outwards and ZFs disapear, the empirical value of L_r is mainly dominated by the radial turbulent structures, as shown in figure 3.16.

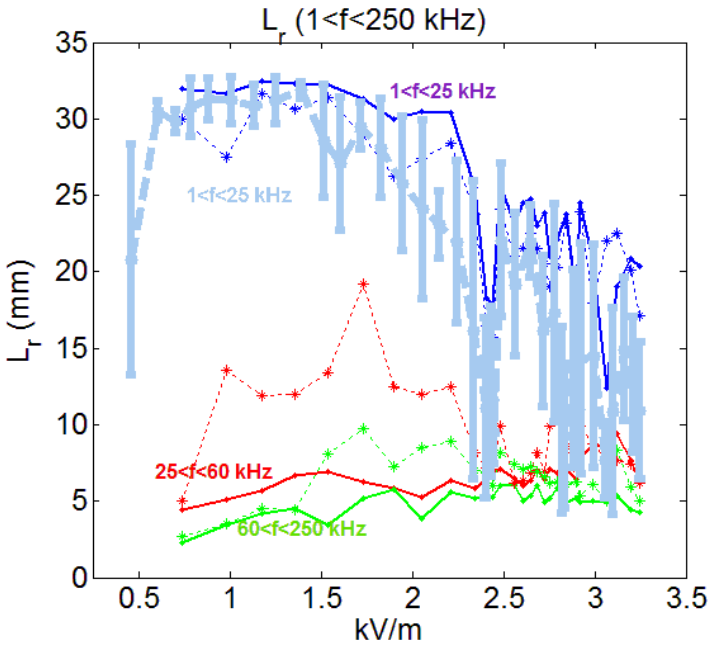

Figure 3.15 L_r dependence on E_r. Spectral energy of radial turbulence is dominated by low frequency fluctuations (1<f<20 kHz). A clear reduction of L_r is driven by radial electric field. Higher frequency fluctuations are not affected by electric field. Shaded lines represent L_r obtained through cross-coherence instead of cross-correlation, the result is similar in both cases.

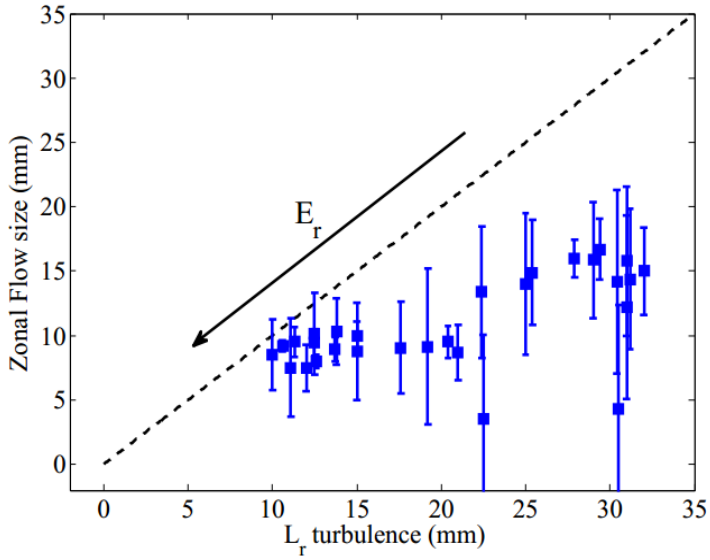

Figure 3.16 The empirically obtained measurement of L_r is dominated by the radial correlation length of turbulence itself when $E_r$is weak. As E_r increases, the measured L_r decreases, indicating a reduction of correlation length of turbulence. The minimum size of radial turbulence is measured when LRC activity is large and empirical L_r is supported by radial size of LRC.

III.1.3.3. Shearing rate of E_r

The results shown in this section have been obtained by applying the tools which allow the characterization of effect of shearing rate of E_r at different spatial scales. Indeed, spatial scale through which shearing is calculated has a strong influence on its final value. The scale parameter associated to the Gaussian spatial Kernel is modulated in order to calculate shearing in E_r, as explained before. The results show that, for values of NC E_r lower than about 2 kVm^{-1}, the magnitude of the shearing rate does not depend on the spatial scale. However, once NC E_r increases above 2-2.5 kVm^{-1} the calculated shearing rate is very sensitive to the spatial scale along which its value is being calculated. This indicates that the shearing rate of the short scale length E_r increases when the NC E_r increases. In figure 3.17 is shown the value of shearing rate of E_r as a function of the scale parameter, for two cases of NC E_r. It is appreciable how, for the case of high NC E_r, smaller values of the scale parameter (associated to short scale lengths) lead to higher values of the shearing rate.

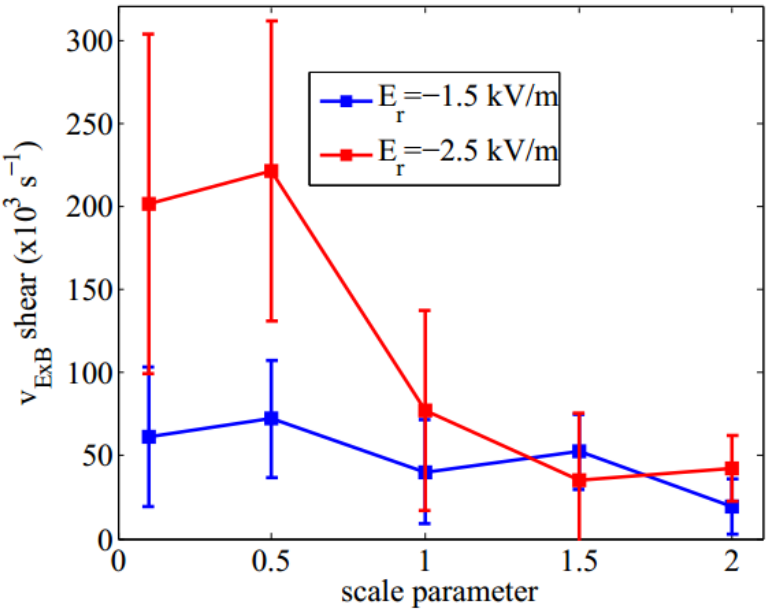

Figure 3.17 The magnitude of shearing rate due to E_r depends on the space scale parameter used to calculate it when NC E_r has a certain value, usually above 2 kV/m. When the magnitude of E_r is low, the value of shearing rate due to short scale length Er is not affected by scale parameter.

Interestingly, the measured magnitude of the shearing rate due to short scale length E_r reaches values above $10^5\ s^{-1}$.Turbulence decorrelation rate is stimated as ${\tau_c}^{-1}$, being τ_c the autocorrelation time of electrostatic turbulent fluctuations. The value of decorrelation rate of turbulence is or the order of $10^5 s^{-1}$ [151] in magnetically confined plasmas. This means that the short scale length E_r shearing rate has a magnitude of the order of the decorrelation rate of turbulence.

Following the empirical results, the connection between the NC E_r, the level of LRC (as indication of the intensity of Zonal Flows) and the radial correlation length of turbulence is evident as well as the differences between the two different spatial scales in shearing rate. These results are summarized in figure 3.18.

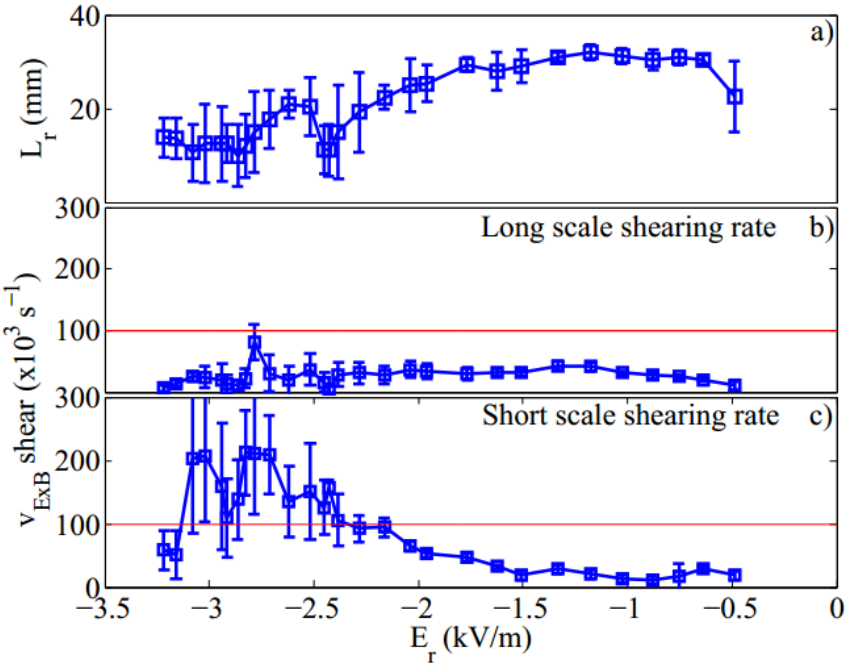

Figure 3.18 a) Reduction of radial correlation length of turbulence with increasing radial electric field. In b), the calculated shearing rate due to large scale radial electric field is always below the threshold value necessary to decorrelate turbulence. In c) is shown the value of shearing rate due to the short scale length E_r. Shearing rate increases with the value of NC radial electric field.

III.1.3.4. Influence of external biasing on LRC

The influence of externally imposed radial electric fields on the amplitude of Long Range Correlations (LRC) has been also investigated.

Experiments were carried out in neutral-beam injection (NBI) heated hydrogen plasmas in the TJ-II stellarator (P_{NBI}≈ 450 kW, B = 1 T, plasma minor radius ⟨ a⟩ ≤ 0.22 m), with line-averaged electron density n_e = (1.0− 2.5)× 10^{19} m^{-3}, central electron and ion temperatures T_e = 250 − 300 eV and T_i= 100 − 150 eV, respectively. A graphite electrode was installed on a reciprocating probe drive at segment A8 and biased with respect to a radially movable limiter at segment C3. In the present experiments the electrode was inserted 3 cm, corresponding to normalized effective radius r/a = 0.85, whereas the limiter was kept at r/a = 1. The electrode was biased with respect to the limiter with an AC voltage during plasma discharges. The waveform of the biasing voltage is a negative half- wave rectified triangular wave, i.e. in each period, half- cycle biased with V_{bias} = 0 and half-cycle biased with a triangular shape peaked

at V_{bias} = −340 V as shown in figure 2(a). The frequencies of 40, 60 and 80 Hz were chosen for the present experiments.

Figs 3.19 and 3.20 show examples of the global influence of negative biasing on the floating potential signals measured by probes B and D and on the level of LRC, respectively.

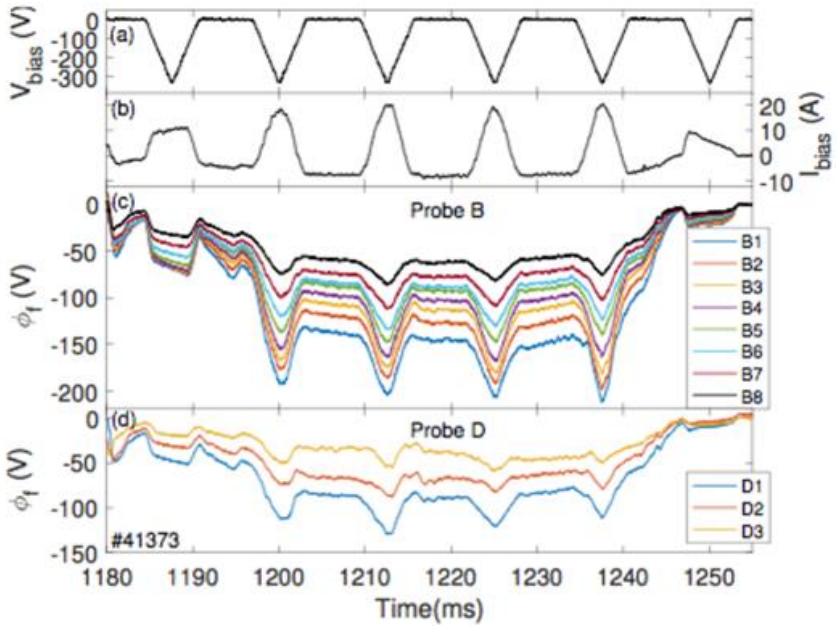

Figure 3.19 Above, external negative biasing potential and response of biasing current. In the middle, the response of the radial profile of floating potential to external biasing measured in sector B. In the bottom, the response of floating potential at sector D.

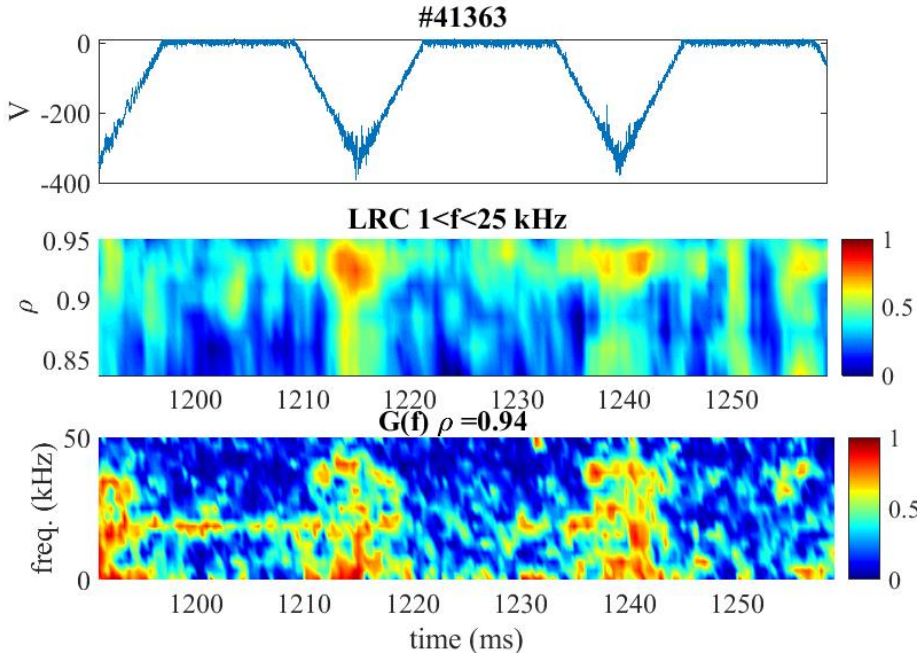

Figure 3.20 Above, external biasing. In the middle is shown the spatio-temporal evolution of LRC and below is shown the cross-coherence resolved in frequency. Both LRC and cross-coherence at low frequencies are enhanced by the external biasing.

Figure 3.20 shows the time evolution of the LRC during biasing at f=40 Hz; the amplitude of LRC is strongly amplified during electrode biasing, reflecting the role of the radial electric field in modifying LRCs, in agreement with experiments where Er was modified by changing plasma density.

III.1.3.5. Physics of Zonal Flow Dynamics

Two processes are under investigation to understand the observed interplay between radial electric fields and the amplitude of Zonal Flows. First, sheared electric fields are efficient turbulence symmetry-breaking mechanism. This hypothesis deals with Reynold's stress, which is assumed to act as a generation term of Zonal Flows [152, 153]. Second, radial electric field can induce large values of $E_r \times B$ drift which prevents the locally trapped particles from drifting radially, reducing the effective damping times of Zonal Flows [154, 155]. Actually, previous studies (simulations and theory) confirm the amplification of low frequency ZF structures in plasmas with reduced viscosity [138]. In figure 3.21 is shown an example of how the decay time of Zonal oscillations is strongly modulated by the value of plasma viscosity.

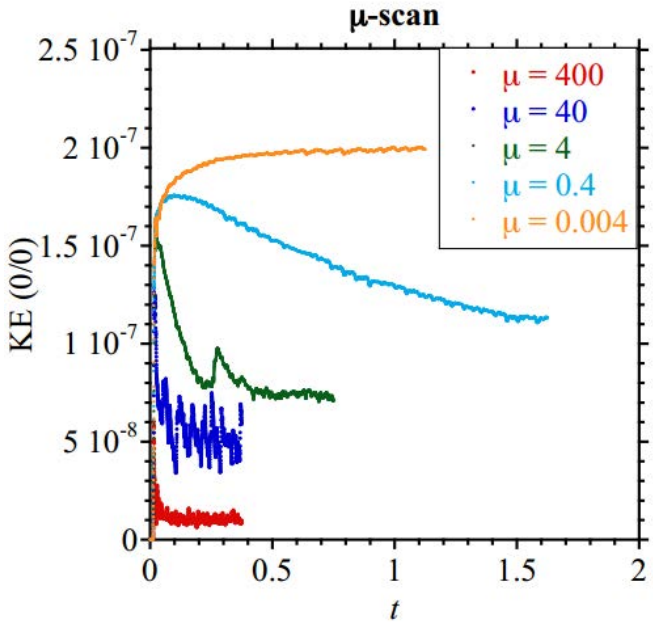

Figure 3.21 Dependence of the decaying times of Zonal Flows (m/n = 0/0) with value of the plasma viscosity μ. Courtesy of Dr. Luis García Gonzalo.

The interaction between Zonal Flows and turbulence can be described by a model (eq. 3.10) based on the Lotka-Volterra equations that describe the dynamics of periodic reactions [156, 157]. In 3.10 is included a generation or driving term, which is associated to Reynolds stress and a damping term, linked to the viscosity [128].

$$\frac{dA_{ZF}(t)}{dt} = R(t) - \mu A_{ZF}(t) \tag{3.10}$$

where $R(t)$ represents the temporal evolution of the spatial derivative of Reynolds stress, μ is the damping coefficient and $A_{ZF}(t)$ is the amplitude of the Zonal Flow. Recently, the model has been introduced to study Zonal Flow-like fluctuations in electron cyclotron heated plasmas in the TJ-II stellarator [128, 129], showing that, although the turbulence-driven forces can provide the necessary perpendicular acceleration, no evidence of causal relation between the ZF drive and the locally measured Reynolds stress could be established.

Reynold's stress drive: In the present thesis Reynold's stresses have been simultaneously measured in two localized radial positions using the 2D probe (see fig. 2.3). Poloidal velocity v_θ is calculated from the radial derivative of V_f and radial velocity v_r is obtained from the variation of V_f along poloidal direction. Fluctuating radial electric field $\widetilde{E_r}$ can be obtained at four points along second and fourth column. At each radial position, the final value of $\widetilde{E_r}$ is taken as the average between the two values coming from the two columns as well as the position is taken as the intermediate distance between the two probes. This average is taken in order to avoid any possible phase shift effect in the calculation of $\widetilde{v_\theta}$ due to the mismatch in poloidal position. The analogous procedure is followed for obtaining $\widetilde{v_r}$ at each radial position. Then, from these data the radial derivative of Reynold's stress is calculated at a fixed position. $E \times B$ velocity is estimated from floating potential measurements as:

$$\begin{aligned} v_\theta &= \frac{E_r}{B} \\ v_r &= \frac{E_\theta}{B} \end{aligned} \tag{3.11}$$

The mean poloidal velocity of fluctuations is expected to respond to the Reynolds force as:

$$\frac{d\langle v_\theta \rangle}{dt} = -\frac{d\langle E_r \rangle}{Bdt} = -\frac{d\langle \tilde{v}_r \tilde{v}_\theta \rangle}{dr} = R \tag{3.12}$$

The negative sign is due to the fact that, assuming E_r is driven by RS, the term R has to be negative in order to propel the plasma in the negative sense of the poloidal direction.

Then, the Reynolds product $\langle \tilde{v}_r \tilde{v}_\theta \rangle$ is calculated as the spatial and time averaging (over periods of 1 ms) of a fluctuating quantity ($\tilde{v}_r \tilde{v}_\theta$). Figure 3.22 shows the evolution of Reynolds stresses and its gradient (R) with radial electric fields in NBI plasmas. The order of magnitude of R calculated as $\langle \tilde{v}_r \tilde{v}_\theta \rangle$ in temporal windows of 1 ms is in the range of $R \approx 10^7 m/s^2$. This value is not high enough to produce the necessary turbulent acceleration to drive radial electric field ($d\tilde{E}_r/Bdt \approx 10^8 m/s^2$), neglecting the damping term on the equation 3.10.

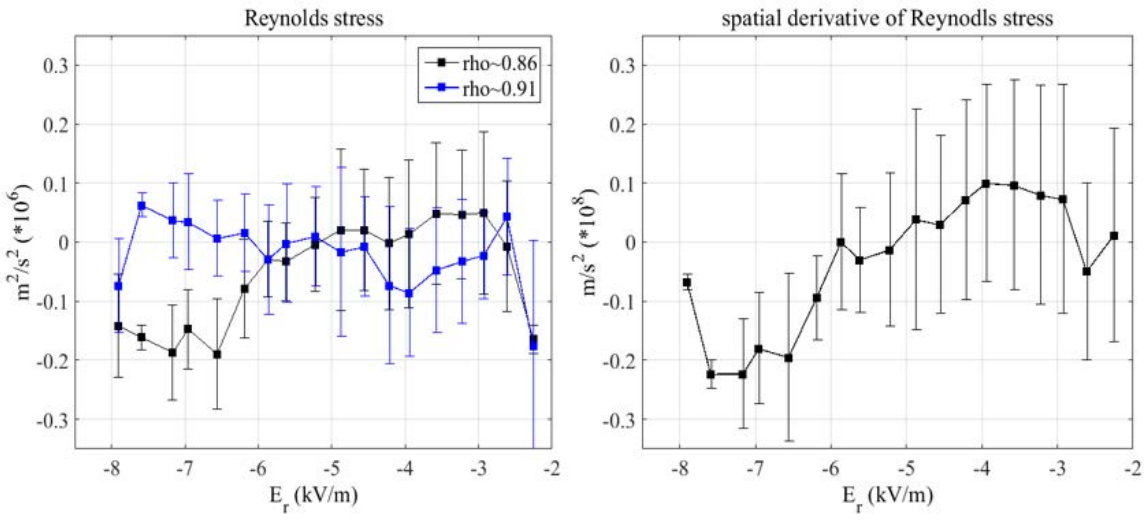

Figure 3.22 Reynold's stress measured at two radial positions and its dependence on the value of NC Er. In the mst internal position, there is a slightly tendency to an increase in the magnitude of RS (negative value). The magnitude of RS is in the order of $10^5 m^2 s^{-2}$.

In order to minimize the effect of time average on the value of R, the analysis has been performed down to the scale under the millisecond (each $\tilde{E}_r$ excitation event has a duration of about $\approx 300\ \mu s$) using a conditional average technique. As a result, and in agreement previous findings [128, 129], the order of magnitude of R during zonal $\tilde{E}_r$ excitations can be strong enough to produce acceleration but, again, a causal relation between the empirical value of R and its deduced value from $\tilde{E}_r$ has not been found.

These results suggest that ZF is not only related with turbulent acceleration (R) but also to other factors that may affect ZF damping, e.g. viscosity (μ). Effective viscosity was calculated by using the aforementioned conditional average technique, proceeding as follows:

Identification of Zonal Flows: Conditional averaging of $\widetilde{\mathrm{E}}_r$

The first step in the detection of Zonal Flows is to apply a low pass filter to $\widetilde{\Phi}_f$, which leaves the remaining low frequency band (<20 kHz) of $\widetilde{\Phi}_f$ to be analyzed. The effective detection of Zonal fluctuations is accomplished by the use of conditional averaging technique, as used in previous studies of plasma fluctuations [158, 159]. This technique is based on the use of a trigger condition to detect relevant candidate fluctuations together with several variable conditions. The triggering condition is used to detect those fluctuations which are candidates to correspond to ZF and is defined as $A_{\widetilde{V}}(t) > RMS(\widetilde{\Phi}_f)$, where $A_{\widetilde{V}}(t)$ is the instantaneous amplitude of ZF and $RMS(\widetilde{\Phi}_f)$ is the root mean square of fluctuations. From previous works [160] is concluded that plasma fluctuations follow exponential like decays and that decay times have values between 10 and 80 μs. So a second condition was set so that $A_{\widetilde{V}}(t + 100\ \mu s) < RMS(\widetilde{\Phi}_f)$, and $A_{\widetilde{V}}(t + 10\ \mu s) > RMS(\widetilde{\Phi}_f)$, being t the triggering time. In this way, all fluctuations whose decaying times are smaller than 10 μs or larger than 80 μs are discarded.

Damping of Zonal Flows

The second term on the right hand side of equation 3.10, $\mu A_{ZF}(t)$, accounts the decay rate of the fluctuation, which is given by the coefficient μ, while $A_{ZF}(t)$ is the amplitude of the fluctuation. The decay coefficient μ is considered as the effective viscosity and its empirical value is calculated by fitting the tails of Zonal Flow excitations present in the fluctuating V_f signals. The evolution of the ZF after the triggering peak is assumed to be dominated by an exponential model, considering the driving Reynold's stress forces negligible:

$$A_{\tilde{V}} = A_p e^{-\mu t} \tag{3.13}$$

where A_p is the amplitude of the peak and μ is actually the effective viscosity, expressed in $[s^{-1}]$. The fitting is performed from the triggering time (peak) and until 150 μs after. The explained procedure is applied to $\widetilde{\Phi}_f$ signals. Effective viscosity is assumed to remain constant during the time of the $\widetilde{E}_r$ excitation, which means that the calculated value of μ fits the model described in equation 3.10 during the surviving time the excitation. In usual plasma discharge in TJ-II, this method detects several ZF events. The events can be processed and an average evolution of ZF is obtained as a result (as shown in fig. 3.23).

Dependence of NC E_r on the damping term

For each ZF "excursion" detected, RS evolution is calculated for the same time interval. Then, the RS and V_f events are conditionally averaged in function of the value of $NC\ E_r$. This last is modulated by the external biasing. As result, the model described by equation 3.13 can be evaluated for different values of $NC\ E_r$. The damping term can be calculated for the cases of the biased discharges as well as the four shots without biasing.

The characterization of effective viscosity has been a major challenge until now. As explained previously, effective viscosity is empirically derived from the calculation of the decay times of zonal fluctuations in E_r. First resutls obtained show that decay times tend to increase with the value of E_r, however, the existence of large error bars did not allow to get a final conclusion [161]. After taking a careful look to the raw data it was realized that most of the zonal perturbations which fulfill the conditions described in this section actually don't have a real exponential decay. This leads to a huge error bar due to exponential fitting. This problem is overcome by filtering the selected data in order to process only those tails whose decay is exponential. This action is partially successful and finally the error bar is reduced for the higher values of E_r.

As shown in figure 3.23, the calculated effective viscosity (μ), have values from 20 to 100 μs^{-1}, which are asociated to decay times from 10 to 70 μs. In the case of density ramp discharges, the increase of E_r induces a tendency to decay in μ within the error bar. Once external biasing is applied the decrease of μ for large values of E_r is more evident.

As seen in figure 3.23, the large error bars appear when E_r is low (in both density ramp and external biasing cases) being reduced once E_r increases. The author considers that this difference in the error bar is due to two facts. First, assuming that large values of E_r lead to an enhancement of ZF activity and a reduction of spectral energy of broadband turbulence, the probability of detecting zonal oscillations is larger than in the case of lower E_r. Second, when E_r is low, spectral energy is distributed between broadband (mostly) fluctuations and ZF. Actually, for lower values of E_r, the low or even inexistent level of LRC suggest that ZF are weaker, which means that the processed decay times can correspond mostly to other kind of local plasma fluctuations.

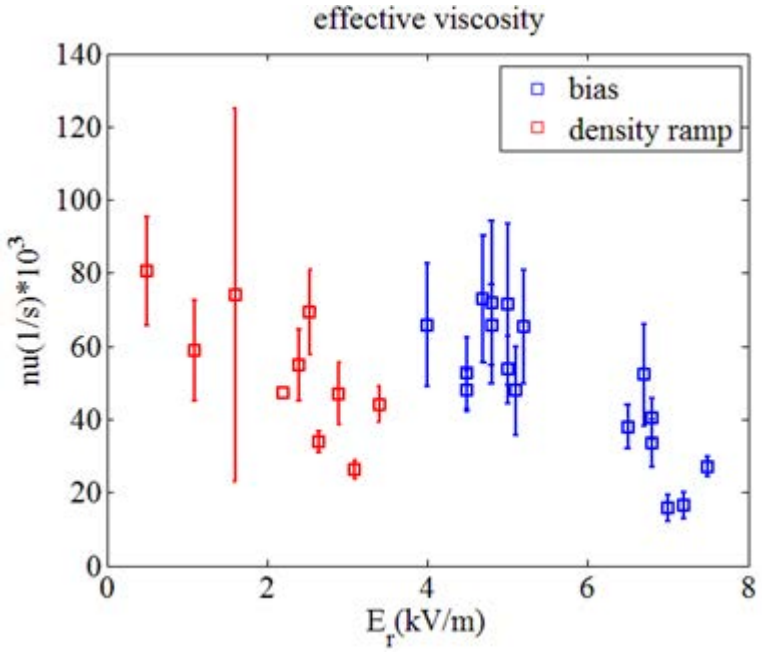

Figure 3.23 Dependence of effective viscosity on NC Er. In red, data corresponds to shots without external biasing. Effective visocosity tends to decrease as radial electric field increases, however, this dynamics is contanied within the error bar. Under biasing conditions, the decrease of effective viscosity is more clear but error bars are still large.

III.1.4. Conclusions

In this chapter, we have studied the influence of long scale length radial electric fields (NC E_r) on zonal flow-like structures in the TJ-II stellarator with the following conclusions:

Influence of NC E_r components on the dynamics of Zonal Flow

During NBI plasma discharges, a negative electric field well is formed in the plasma edge. It was found that the level of LRC (taken as a proxy of ZF activity) increases strongly with the NC E_r, saturating once it reaches a value of 2 kVm^{-1} (negative). LRC are dominated by low

frequencies (1<f<20 kHz). The frequencies associated with ZF-like structures increase with increasing E_r, which means that the ZF has a more fluctuating character when NC E_r is higher.

The radial electric field is composed of different radial scales and there is a strong relation between the magnitude of the electric field structures with short (due to ZFs) and long (neoclassical) radial scales. The $E \times B$ shearing rate corresponding to the short scale length structures of E_r may have sufficient magnitude to regulate turbulence.

The radial profile of cross-correlation is determined by both the extent of edge turbulence and the radial width of Zonal Flows. The obtained $L_r$is a pure empirical value that actually accounts for the radial size of turbulence in the absence of ZF. However, once ZF is present, the value of L_r includes the radial width of ZF in addition to turbulence. The only way to determine the weight of each of these effects was to measure the radial profile of LRC. Once L_r is fully due to ZF an increase in the L_r does not imply a deleterious effect on transport.

These findings are consistent with previous experimental results that shown that the amplitude of LRC is amplified by externally imposed radial electric fields and in the proximity of the L-H transition. In addition, GK simulations show the influence of NC E_r in the residual level of ZF [137]. It is important to point out that this section reports empirical relations between the NC E_r, radial turbulence, $E \times B$ shear flows and low-frequency zonal flow-like structures, which means a dynamical connection between the macro-, meso- and micro-scales.

At high densities, the negative radial electric field satisfies the ion-root solution for ambipolar particle fluxes, in accordance with results in heliotrons and stellarators [162]. The amplification of ZF structures in plasma scenarios with reduced viscosity and its coupling with the $NC\ E_r$, together with the reduction of turbulence reported in this section, are results of special relevance for the coming future stellarators with reduced NC transport. This is due to the fact that the shearing produced by ZF can determine the saturation level of turbulent transport.

Influence of NC viscosity and RS on the dynamics of Zonal Flows

The application of external negative biasing with respect to vacuum vessel in TJ-II NBI plasmas results in the enhancement of LRC as an approximation of ZF activity. Keeping density constant brings an interesting scenario where E_r becomes instrumental as driving mechanism of Zonal Flows. The comparison of this new scenario with previous density driven E_r plasmas is interesting to clarify the role of $E_r$in the appearance of Zonal Flows. E_r is proposed to enhace ZF activity through *RS* driving and /or increasing damping times of ZF (decreasing viscosity).

The use of a 2-dimensional array of electrical probe allows the characterization of local Reynolds Stresses and combined with the operation of a distant probe allows the measurement of LRC for low frequencies. Zonal fluctuations of E_r are identified by using a conditional technique and averages are obtained for different regimes of E_r. The study of decaying times of these averaged long range correlated fluctuations in E_r gives the value of effective viscosity.

Effective viscosity was calculated by identifying oscillation decays and fitting by an

exponential in two sets of plasma discharges where the radial electric field was modulated by the plasma itself and by electrode biasing respectively were selected. Results give viscosity values in the order of $10^4 - 10^5\ s^{-1}$with a tendency to decrease as E_r increases in the NBI regime with edge biasing with strong dependence of LRC with E_r (see figure 3.23). The value of driving *RS* has been also calculated at these time scales, and it has not been possible to assert that its value is related to the amplitude of Zonal field fluctuation.

These results are consistent with recent Monte Carlo simulations showing that radial electric fields in the range of those experimentally measured have an effect in the edge neoclassical orbit losses in the TJ-II stellarator [163]. Although the order of magnitude of turbulent acceleration is comparable to the neoclassical damping of perpendicular flows, its dependence with radial electric fields is not correlated with the evolution in the amplitude of LRC. In addition, NC viscosity manifests as the global relaxation of the ZF fluctuation, but, the local value of *RS* is not necessarily the magnitude of the driving *RS*, which has to be inferred from its average along the flux surface [164].

These findings suggest that both mechanisms, turbulent acceleration driven by turbulence and neoclassical particle orbit effects, are intertwined to determine the dynamics of Zonal Flows.

III.2. Role of isotope mass and evidence of fluctuating zonal flows during the L-H transition in the TJ-II stellarator

The underlying mechanism behind the development of edge plasma bifurcations, leading to the establishment of an edge transport barrier, is still one of the main scientific conundrums facing by the magnetic fusion community after more than twenty years of intense research.

The results presented in this chapter show the critical role of both zero frequency (equilibrium) and low frequency varying large-scale flows for stabilizing turbulence during the triggering of the L–H transition in magnetically confined toroidal plasmas. No evidence of isotope effect on the L–H transition dynamics was observed in the investigated TJ-II plasma scenarios.

It is concluded that there are different paths to reach the L-H transition with impact on the conditions to access the H-mode. This chapter is based on the publication [165]:

III.2.1. Introduction

The transition (L-H transition) of plasma to high confinement mode (H-mode) is one of the most interesting object of study in both tokamak and stellarator scenarios. After some decades since the discovery of H-mode, the experimental works have been focused on the study of the mechanisms which lead to the transition from L-mode to H-mode as well as the conditions that allow plasma to remain at high confinement mode and how these mechanisms and conditions are affected by some plasma parameters. These conditions are related to radial electric field. One of the variables which can introduce variations in the behavior of plasma (mainly confinement time and power threshold) during L-H transition is the isotope mass.

Edge transport barriers are a key tool for the enhancing of the plasma confinement properties in magnetic-fusion devices. The transition from L- to H-mode plasmas is characterized by the development of an edge transport barrier, the suppression of turbulence, the formation of a negative radial electric field well in the edge and the reduction of D_α emission [166, 167]. During the L-H transition, the turbulence is decorrelated by $E \times B$ shear flows and by inhomogeneities in radial electric field [168]. The understanding of H-mode regimes has led to a more complete understanding of turbulent transport in high temperature plasmas for nuclear fusion. The scientific interest generated by the study and exploration of improved confinement regimes has led to a very extent and varied theoretical and experimental work, which are properly reviewed in reference [165].

Understanding the impact of the isotope mass on transport during the transition from low to high (L–H) confinement mode is determinant for the development of ITER base-line scenarios with controlled edge localized modes (ELMs) and reduced L–H power threshold.

At present, the nature of the mechanisms behind the $E_r \times B$ shear flow during transition L-H is still an open question. One of the most important process under discussion is the relation between turbulence driven flows (ZF) and pressure gradient driven flows during the triggering of L-H transition and sustainment of H-mode plasmas [169] . The radial electric field in the plasma edge is balanced by pressure gradients and plasma flows, as described in equation 3.14:

$$E_r = \frac{1}{Z_i e n_e}\frac{dp_i}{dr} - u_{\theta i}B_{\varphi} + u_{\varphi i}B_{\theta} \tag{3.14}$$

where ∇P_i is the pressure gradient (also known as diamagnetic term), v_θ and v_t are the poloidal and parallel velocities of fluctuations and B_t and B_θ are the poloidal and toroidal components of magnetic field. Thus, the pressure gradient as well as the poloidal and toroidal flows play a crucial role in the development of radial electric fields and in the control of turbulence transport via sheared flows.

The L-H transition is present in both Tokamak and Stellarator devices, which demonstrates the ubiquitous character of L-H transition in fusion plasmas. It is also known that, in both tokamak and stellarators, the turbulence driven zonal flows and the ion pressure gradients driven flows play a synergistic role in the triggering of L-H transition. There are empirical evidences of Zonal Flows triggering the L-H transition in Alcator C-mode [170] and in EAST [171, 172] tokamaks. The presence of ZF during Limit Cycle Oscillations (LCO) is reported in tokamak plasmas at the L-H transition [173, 174] and having shearing rates comparable to the mean shearing rate [175]. The interaction between $E_r \times B$ flows and turbulence has the form of predator–prey model in the proximity of the L-H transition, which is known as *limit cycle oscillations* (LCO).

Recent experimental work carried out in the HL-2A tokamak is of special relevance as it gives a detailed description of how the growing up of pressure gradients in the plasma edge is necessary to trigger the transition to H-mode in tokamak devices [176]. This result is based on the observation of two types of LCO, with opposite temporal ordering between $E_r$and turbulence. The first type is the standard predator-prey cycle, where the turbulence leads the generation of zonal flow, which in turn suppresses the former. With the second type, the $E \times B$ flow grows first, causing the reduction of fluctuations. The latter points to the pressure gradient as candidate for inducing the transition to the H-mode. This result is in agreement with theoretical predictions for tokamak plasmas [177] as well as with empirical results [178]. So from both theoretical and experimental results is concluded that the development of ion pressure gradients is necessary to achieve L-H transition or at least to maintain the plasma in H-mode confinement in Tokamaks.

In stellarators, it is still an open question whether E_r is dominated by ion pressure gradients or by Zonal Flows. The ratio of the main electric field to the diamagnetic contribution (directly related to pressure gradient) is larger than one in the W7-AS stellarator during H-mode [179, 180]. In the TJ-II stellarator, the diamagnetic contribution from ion pressure gradient is comparable to the measured E_r in L-mode but it changes only very slightly after the L-H transition. Also in the TJ-II stellarator was observed that, during the L-H transition, the strong

reduction of density broadband fluctuations takes place before the increase of the mean E_r but is simultaneous to the enhancement of low frequency (1<f<20 kHz) fluctuating radial electric field [181]. In addition, experimental results on ZF carried out in the TJ-II stellarator prove that the Zonal Flow activity reaches a maximum level when electron plasma density is close to L-H transition density threshold [182]. Finally, it is known that both mean and low frequency fluctuating E_r are capable of developing transport barriers, which are a key element present on the L-H transition and H-mode plasmas.

Isotope effect

Understanding the underlying mechanism of plasma confinement scaling with isotope mass has been a long-standing open issue in magnetic confinement fusion plasma research [183]. It has been observed, in most tokamak experiments, that the plasma confinement time increases with the increasing ion mass under similar plasma conditions.

The study of the isotope mass effect on L-H transition power threshold is determinant for the development of ITER-base line scenarios with controlled edge localized modes (ELM's) and reduced L-H power threshold. In general, in tokamaks, experimental results show that L-H power threshold is reduced by about 50 % when Deuterium or Helium are used instead of Hydrogen [184]. Latest results obtained in mixed Hydrogen/Deuterium plasmas at JET indicate a nonlinear dependence of L-H transition power threshold, confinement time and stored energy on the concentration of Deuterium with respect to Hydrogen [185]. JET has also shown in recent 2016 experiments that an injection of a trace of Helium gas (below 10 %) in hydrogen plasma leads to a reduction of the L-H power threshold by 25 %.

Motivated by the newest contributions on the role of E_r and its components in the triggering of L-H transition, in both tokamaks and stellarators, as well as the influence of isotope mass and magnetic configuration, new experiments were proposed. A detailed description of the evolution of fluctuating Zonal Flows together with mean sheared flows during the L-H transition in H-mode plasmas are discussed in this chapter.

III.3.3. Experimental set-up and methodology

III.3.3.1. Plasma scenarios

Experiments have been carried out in ECRH and NBI heated plasmas. Heating consisted of two gyrotrons delivering 300 kW each at X mode with a frequency of 53.2 GHz plus two NBI injectors which launch co- and counter-beams with up to 700 kW por-through power with neutral Hydrogen accelerated at about 33 kV. L-H transition is achieved in NBI heating phase (under a power of 500 kW) and with a line averaged plasma density of $\approx 2 \cdot 10^{19} m^{-3}$. Central electron temperatures are about 350 eV. Two scenarios have been set up for isotope mass concentration of Hydrogen and Deuterium: 100% Hydrogen and Deuterium dominated (70%) plasmas were generated in the NBI heating regime. All the data shown here come from experiments done in the standard magnetic configuration of TJ-II. This is, having the edge rotational transform value close to 1.6, which corresponds to *n/m=8/5* rational surface located at $\rho \approx 0.81$.

III.3.3.2. Plasma diagnostics

Large-scale coherent structures in plasma potential (Zonal Flows) are investigated by using a dual system of Langmuir probe arrays, labelled as probe 1 and probe 2 (fig. 3.24). Probe 1 is the 2-dimensional system and probe 2 "probe B" (see section II.1). The sampling rate of Langmuir signals is 2 MHz and the radial region accessible is at $\rho > 0.8$. Radial electric field (E_r) and wavenumber spectra of turbulence are characterized by two-channel Doppler reflectometer (fig. 3.24). It allows the measurement of perpendicular rotation velocity of turbulence and density fluctuations with good spatial and temporal resolution. All the necessary information to understand principles and applications of Doppler reflectometry (DR) can be found in reference [186]. DR can cover a radial range of $0.6 < \rho < 0.8$. Finally, Thomson scattering was used to characterize electron temperature and plasma density profiles [187].

III.3.3.3. Methodology

The L-H transition is characterized by sudden and strong decay of H_α emission simultaneous to the increase of line average density as well as plasma stored energy and confinement times. Zonal Flow intensity is measured by using Langmuir probes (figure 3.24). The techniques used to detect and quantify ZF are the cross-correlation and the cross-coherence calculated between distant probes.

The followed procedure is equivalent to that explained in the previous section. The level of LRC can be measured by electrical probes during L-mode, H-mode and during L-H transition. As in all previous parts of this work, distant cross-correlation (LRC) and phase cross-coherence are computed for low frequencies (1<f<20 kHz). This quantities are calculated in temporal windows of 1 ms, with an overlap of 0.5 ms. L-H transition leads to a strong and global modulation in the plasma parameters as well as in plasma-wall interaction magnitudes, which induces strong changes in the signals obtained by plasma diagnostics. This global modulation is present in Langmuir probe measurements and can be reflected as high level of LRC if signals are not properly pre-processed. To avoid that matter, Chevyshev second order filter is applied to the data which have been filttered previously in the band from 1 to 20 kHz. In this way, any contribution of the DC component of V_f signals to LRC can be ruled out [188]. This methodology is done for both Hydrogen and mixed (Hydrogen + Deterium) plasmas in order to investigate any possible difference in the level of the LRC during the L-H transition.

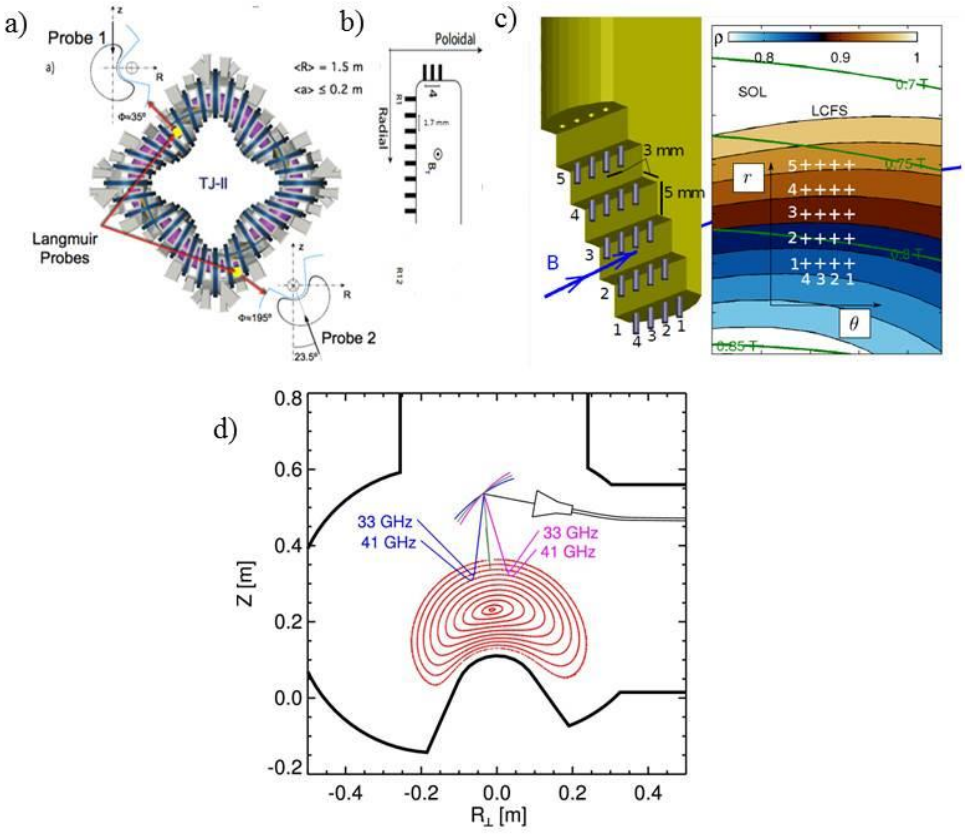

Figure 3.24 a) top view of TJ-II stellarator with the situation of the two probe arrays. In b) is shown a draw of probe 2. In c) is shown a CAD image of probe 2D and the position of its Langmuir pins within edge region of TJ-II. Finally, in c) is shown the relative position of Doppler reflectometer with respect to plasma.

III.2.3. Results and discussion

III.2.3.1. L-H transition in the TJ-II stellarator

Previous experiments carried out in TJ-II under Li-coated vacuum vessel and NBI heating power have reported the experimental evidence of spontaneous L-H transitions. In TJ-II, L-H transition occurs at a threshold value of electron density. In NBI heating phase, plasma density depends on NBI heating power and on the magnetic configuration. The results shown in this thesis report have been obtained in standard magnetic configuration and with NBI heating power of 500 kW [189]. As mentioned before, the threshold density values are of about $2 \cdot 10^{19}\ m^{-3}$. Similarly to other devices, in TJ-II, the L-H transition is accompanied by a reduction in the $H_\alpha$emission due to the decrease of outwards particle flux. It is reported also a reduction of the level of broadband fluctuations by a factor of 2-3. In addition, L-H transition leads to an increase of density gradients, stored diamagnetic energy and energy confinement time (tipically of about 20% in TJ-II). Also as observed in other devices, at the L-H transition mean E_r becomes more negative and strong $E_r \times B$ flow shear develops together with an abrupt reduction of broadband turbulence. In TJ-II, all the described processes happen within a temporal window of some tens of microseconds around L-H transition with the exception of the mean E_r, whose change towards more negative values takes place in temporal window of the order of the millisecond.

For obtaining the present results, eleven plasma discharges have been studied. Five of them have been carried out with pure Hydrogen plasmas (#42139, #42146,#42147, #42178, #42179) and the other six have been done in mixed Hydrogen plus Deuterium plasmas (#42131, #42133, #42134, #42135 and #42136), with actually 70% of Deuterium. In all these discharges, L-H transition takes place at density values close to $2.10^{19} m^{-3}$ and the behavior of plasma parameters during a temporal window around L-H transition time is highly reproducible. On the other hand, the duration of H-mode, after L-H transition, does not follow a common or reproducible pattern, as plasma remains in H-mode typically for a period of 5 to 10 ms but is different for each plasma discharge. During the process of L-H transition H_α and D_α emission decreases dramatically and energy confinement time increases, due to the increase of stores diamagnetic energy as well as a clear decrease of H_α emission, due to the reduction of particle transport radially outwards.

III.2.3.2. Zonal Flows during L-H transition

As pointed out in the introduction, experimental results obtained in W7-AS and TJ-II stellarators suggest the presence of low frequency oscillating E_r (Zonal Flows) in addition to the mean radial electric field which is driven by ion pressure gradients, in the L-mode preceding the L-H transition, during the L-H transition and after it in the H-mode. Zonal Flow-like fluctuations are identified through the calculation of cross-correlation and cross-coherence in

phase between distant electrical probe measurements (LRC). The highest level of LRC have been found between the probe tips placed at the third row in probe 1 and the innermost probe tip placed at probe 2. In terms of the TJ-II minor radious this situation corresponds to $\rho \sim 0.88$. The evolution of LRCs during L–H transition has high reproducibility in Hydrogen and Deuterium plasmas. The figure 3.25 shows the time evolution of LRCs of floating potential fluctuations during the development of L–H transitions in Hydrogen plasmas. The degree of long-range coupling for potential fluctuations is significant in the low confinement regime, increases in the proximity of the L–H transition and slightly decreases once in the H-mode. LRC are strongly bursty both in time (figure 3.25.c) and space (figure 3.27). It should be noted that the maximum cross-correlation is observed for time delays close to zero, consistent with the existence of a toroidally/poloidally symmetric low frequency (<10 kHz) ZF structures. The result shows the existence of high level of coherence (levels up to 0.9) for low frequency (typically below 10 kHz) during the preceding L-mode as well as during the H-mode (figure 3.25.d).

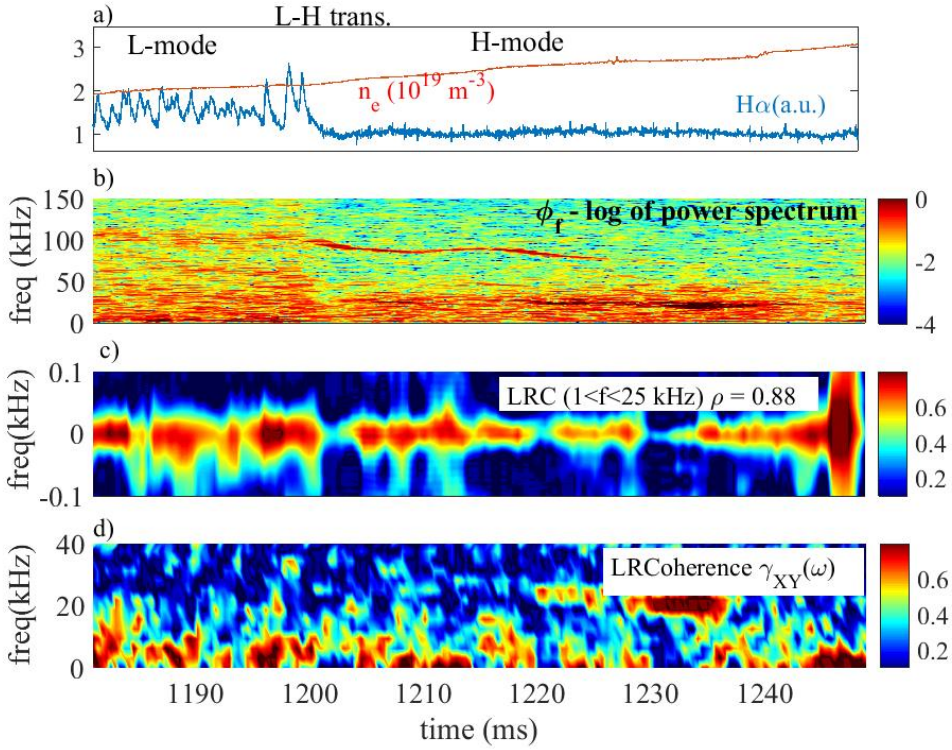

Figure 3.25 Typical temporal evolution of line averaged density and H_α during L-H transition is shown in a). In b), the reduction of spectral power for higher frequency fluctuations in H-mode with respect to L-mode. High levels of LRC are present in L-mode, during the L-H transition and in H-mode plasmas (c). Equivalently, high levels of cross-coherence are present at low frequencies during L-H transition and H-mode.

The highest correlated LP tips (identified as explained before) are selected as reference and then the cross-correlation is calculated between the LP tip placed at probe 1 and all the LP tips radially disposed along probe 2. This operation yields the radial distribution of LRCs. Assuming a Gaussian distribution, the radial size of LRC is taken as the equivalent radial distance between the reference tip and the radial position of the tip placed at probe 2 whose

cross-correlation with reference tip is nearest to 1/e. Figure 3.27 shows the bursty radial behaviour of LRC in Hydrogen plasmas, which also shows that the maximum levels of LRC are concentrated at time delays close to zero, which is consistent with the existence of a toroidal/poloidal symmetric low frequency ZF structures. The behaviour of LRC is similar for D and H plasmas (fig. 3.26).

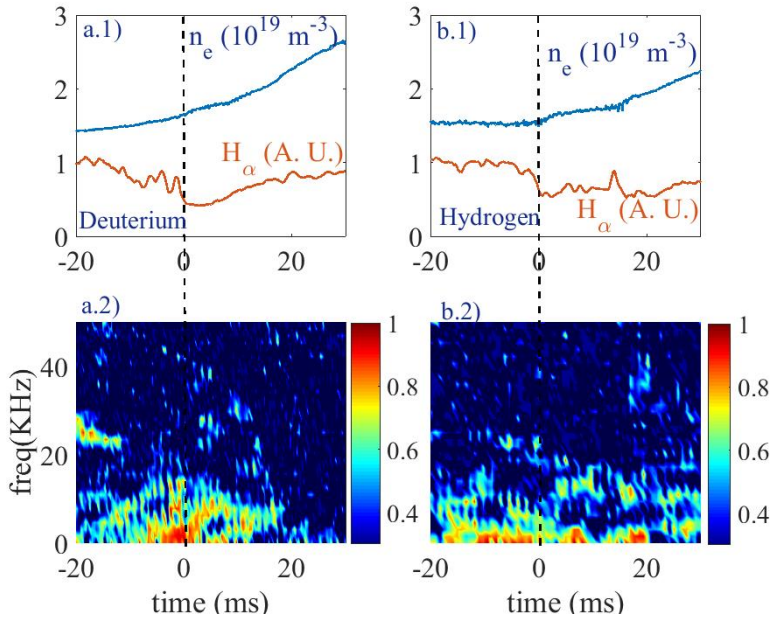

Figure 3.26 Above, evolution of line averaged density and H_α in both Hydrogen (a.1) and Deuterium (b.1) plasmas. Below, cross-coherence present during the L-H transition.

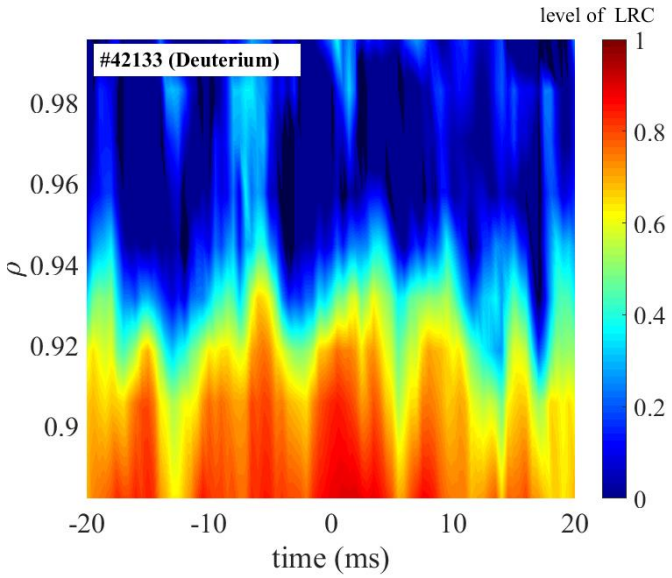

Figure 3.27 Spatial structure of LRC in the external region of plasma edge during L-H transition. LRC exhibits a bursty behavior.

III.2.3.3. Influence of isotope mass on plasma turbulence

The information of the characteristics of micro-turbulence is contained in the wavenumber spectra. The perpendicular wavenumber spectra is measured by steering the incidence angle of the probing beam of the Doppler Reflectometer. DR is able to work in a perpendicular wavenumber range from 1 to 15 cm^{-1}. It is possible to characterize wavenumber spectra in both ECRH and NBI heating regimes as well as in both L-mode and H-mode plasmas, for both pure Hydrogen and mixed (H+D) plasmas. The results show that the heating scenario (ECRH vs NBI) induces a change in the wavenumber spectra. Turbulence level is higher in ECRH than in NBI plasmas, which is in agreement with previous results obtained in the TJ-II stellarator [190]. The variations in the isotope mass ratio do not induce changes in the properties of the turbulence, as seen in figure 3.28.

The wavenumber spectra shown in figure 3.28 is a combination of turbulence level measured using a large set of probing frequencies in DR. The overlaping between the two data sets (Hydrogen and mixed H+D plasmas) is evident in both NBI and ECRH plasmas, suggesting that isotope mass ratio is not relevant. The differences in the wave number spectral power are due to heating scenario (ECRH vs NBI), being the fluctuation level clearly higher in ECRH phase than in NBI heating regime.

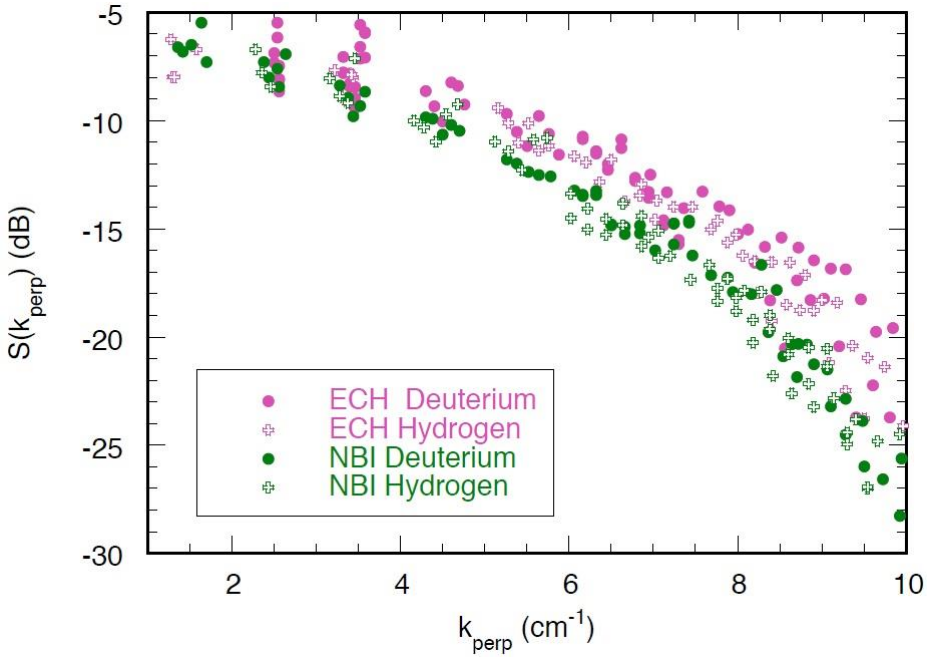

Figure 3.28 Distribution of spectral energy throughout the perpendicular wavenumber of turbulence in TJ-II. The figure shows that the differences in spectral energy are mainly due to the heating scenario instead of the dominant isotope mass. Courtesy of Teresa Estrada.

DR system is optimized in TJ-II and is able to detect the back-scattered signal with a very high signal to noise ratio, which makes the errors associated to Gaussian fitting of the Doppler shifted spectra considerably small. The main error source comes from the power calibration used to compare the fluctuation level measured at different probing frequencies of the reflectometer. In figure 3.28, the spread of the data can be considered as the error in the measurement.

III.2.3.4. Influence of isotope mass on Zonal Flows during L-H transition

L-H transitions have been achieved both in pure Hydrogen and mixed (D+H) plasmas under the same magnetic configuration and NBI heating power. The density threshold in both cases is close to $n_e \approx 2 \cdot 10^{19} m^{-3}$. From previous results it is known that, across the L-H transition, electron temperature profiles are constant while the density radial profiles become more prominent and its amplitude and width increases. At the same time, an edge transport barrier is established. Density and temperature profiles are obtained by an integrated data Bayessian analysis system [148]. Density profiles are similar in Hydrogen and Hydrogen +Deuterium plasmas both in L- and H-mode. This is shown in figure 3.29.

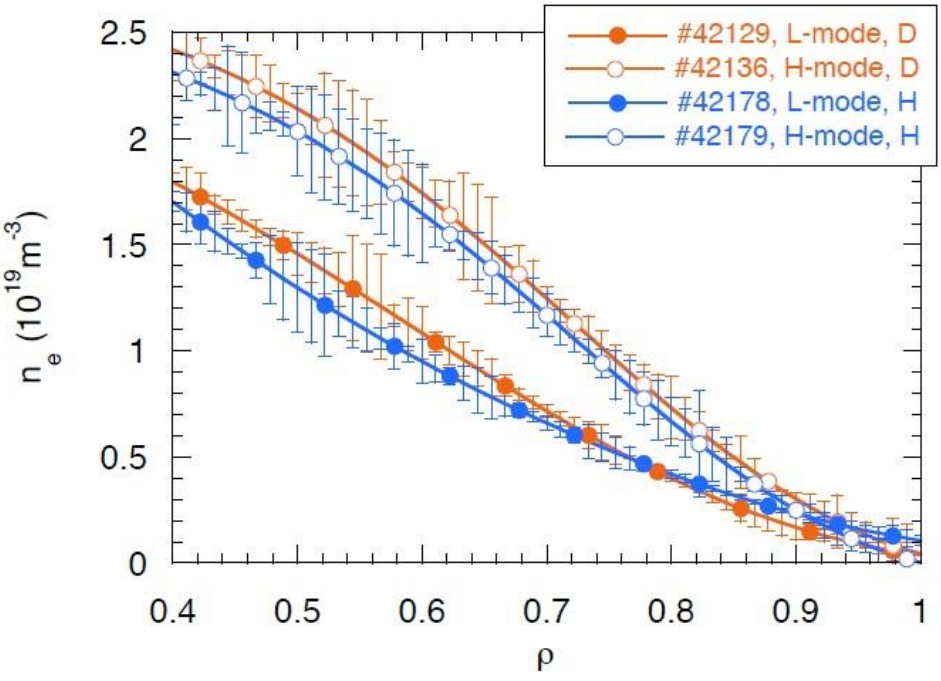

Figure 3.29 Radial profiles of density in the plasma edge of TJ-II. The profile in H-mode clearly steepens with respect to L-mode. The isotope mass has not a clear influence. Courtesy of Teresa Estrada.

The levels of LRC and the magnitude of E_r in L- and H-mode plasmas have been studied in detail. The results show that both LRC and E_r are not affected by the isotope mass ratio. The

results are highly reproducible and are shown in figure 3.30. The radial profile of E_r is measured 1 ms before and after the L-H transition and the temporal evolution of LRC is taken from 10 ms before to 10 ms after L-H transition, being LRC obtained at $\rho \approx 0.88$. The E_r well develops during the L-H transition achieving values of the order of $10\, kVm^{-1}$ (negative) in both Hydrogen and Deuterium plasmas. The amplitude of LRC reaches a maximum value at the L-H transition and it does not show any dependence on isotope mass ratio. This is shown in figure 3.30.

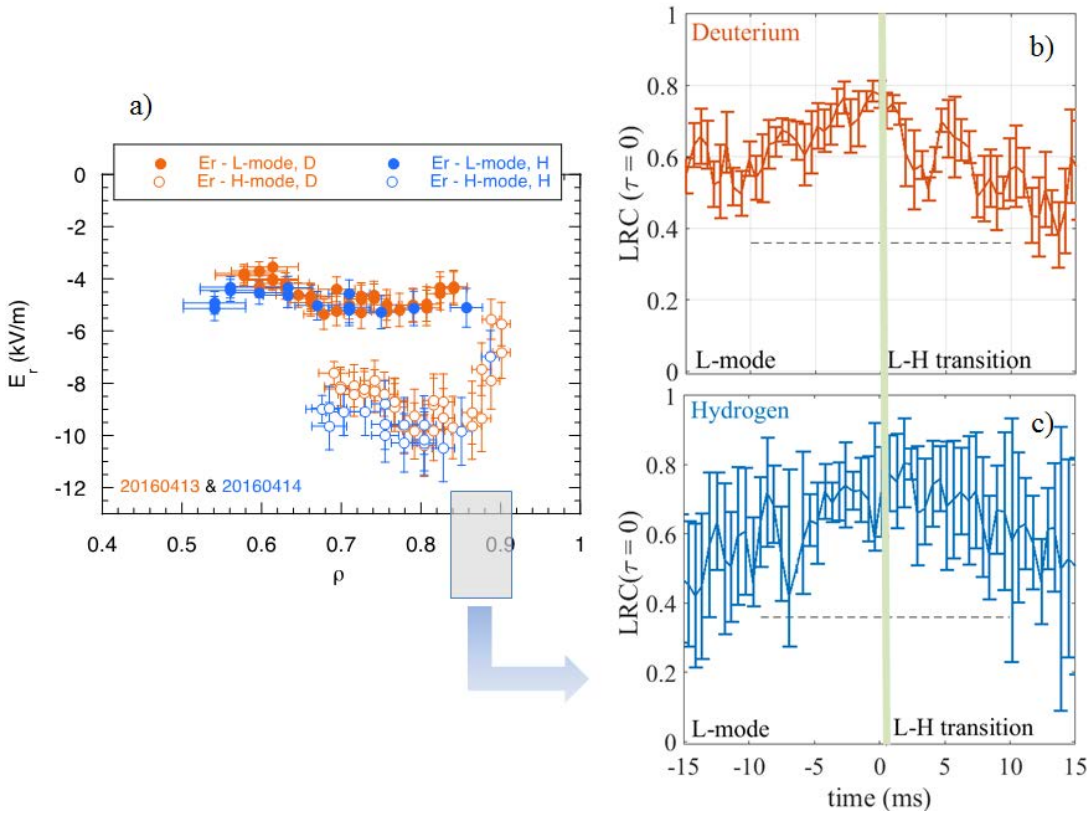

Figure 3.30 a) shows the radial profile of electric field measured by Doppler reflectometry. Er steepens clearly after L-H transition. In b) and c) are shown, respectively, the evolution of the level of LRC during the L-H transition in both, Hydrogen and Deuterium plasmas. LRC reach its maximum level when L-H transition happens. Both Er and level of LRC are not affected by the isotope mass.

Assuming that Zonal Flows are driven from turbulence free energy, the use of bicoherence techniques has been proven to be useful in order to identify coupling between the broadband turbulence and the low frequency fluctuating structures through three wave coupling mechanism [191]. Bicoherence analysis has been succesfully applied also to TJ-II data and the strongest coupling have been found between $\tilde{E}_r$ and $\tilde{n}_e$ [192]. In this case, bicoherence annalysis has been done between $\tilde{E}_r$ and $\tilde{I}_{sat}$, both obtained at probe 1. The evolution of total bicoherence is similar for both pure Hydrogen and Deuterium dominated plasmas in L-mode and during the L-H transition.

In the figure 3.31 is shown the evolution of total squared bicoherence during L-H transition for both isotope mixture cases. The result is an average of the temporal evolution over all the discharges. Both in pure Hydrogen and Deuterium dominated plasmas the integrated bicoherence indicates a modification in the non-linear phase-coupling in the proximity of the L-H transition.

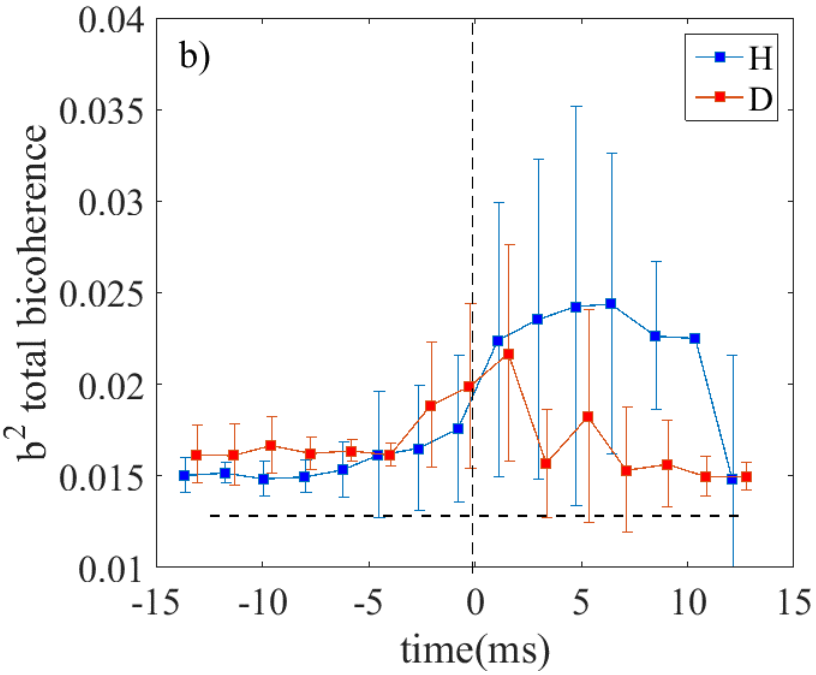

Figure 3.31 Total squared bicoherence, as indication of non-linear coupling between low frequency zonal flows and higher frequency turbulence. The level of bicoherence increases as plasma approaches L-H transition in both Hydrogen and Deuterium dominated plasmas. Once in H-mode, for Hydrogen plasmas exhibit considerably larger values of total bicoherence. Data shown in this figure is a result of average trough discharges.

III.2.3.5. Observation of decoupling between density and potential fluctuations.

The reduction of the fluctuation level is obvious from the time-resolved frequency spectrum of ion saturation current and floating potential during the L-H transition (see figure 3.32).

The intensity of fluctuations below 250 kHz in ion current collected by Langmuir probes is significantly suppressed during L-H transition. However, floating potential fluctuations are compressed to a low frequency range (f<10 kHz) during the L-H transition. These very low frequency fluctuations appear only in potential signals and are the ones which exhibit a global character (LRC), so Zonal Flows. The different behavior of the frequency spectra of potential

and density fluctuations during the L-H transition indicates that LRC are mainly present in potential but not in density fluctuations, which is consistent with the charateristics of Zonal Flow structures.

Finally, as hown in figure 3.32, transient high frequency fluctuation feature is present at around 85 kHz after the L-H transition in both potential and current signals. Its origin is unknown at the moment but it is presumably due to the H-mode equilibrium $E_r \times B$ Doppler shift.

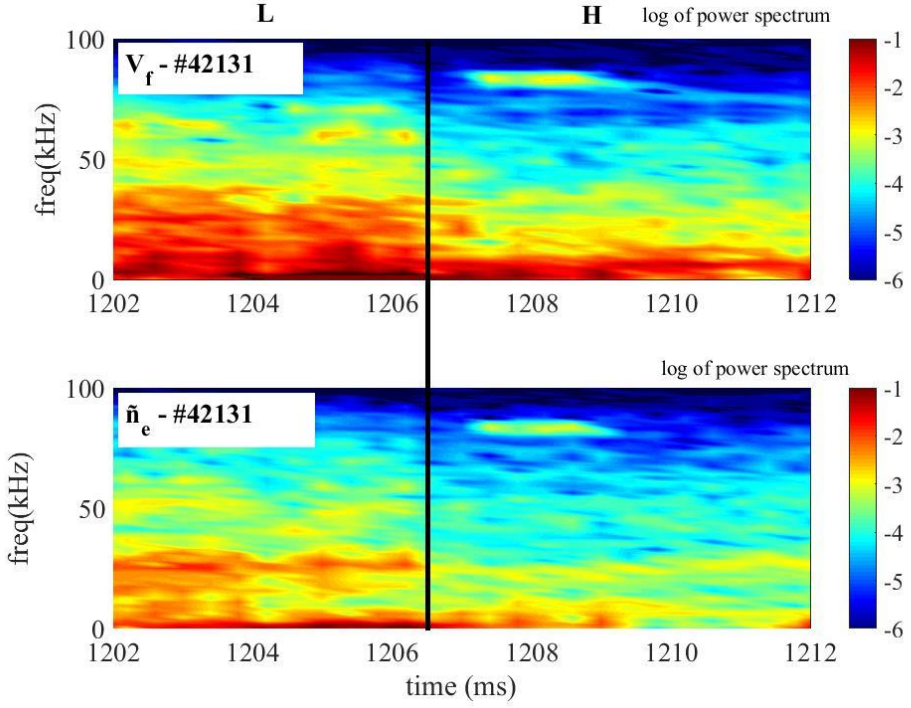

Figure 3.32 Above, temporal evolution of power spectra of floating potential thorugh L-H transition for discharge #42131 (Deuterium). Below, evolution of power spectra of density fluctuations. After the L-H transition, level of density fluctuation decreases for the whole spectra, while, for the case of potential, low frequencies maintain large spectral power.

III.2.3.6. Reduction of radial particle flux during L-H transition

The particle flux due to electrostatic fluctuations can be resolved in frequency from the simultaneous measurement of the spectral components of density (approximated by ion saturation current), potential fluctuations (floating potential) and the poloidal wave number of potential fluctuations, as explained in previous reference works [193]. This calculation is achieved by using three Langmuir tips placed at the head of probe 1 (two V_f and one I_{sat}). In figure 3.33 b is shown an example of how the particle flux is reduced for frequencies below 100 kHz while the frequencies that dominate the remaining particle flux are shifted to higher values during H-mode. Before the L-H transition, in L-mode transport is dominated by frequencies in the band of 20 to 250 kHz and is modest in the frequency range dominated by Zonal Flows (f < 20 kHz). This result shows that particle transport is reduced at low frequencies

as large scale (ZF) structures have symmetric characteristics. In H-mode plasmas turbulent transport is strongly reduced for frequencies below 100 kHz due to the reduction of density and potential fluctuations. High level of Long Range coherence is present in L-mode plasmas as well as during the L-H transition and H-mode plasmas (figure 3.33 b).

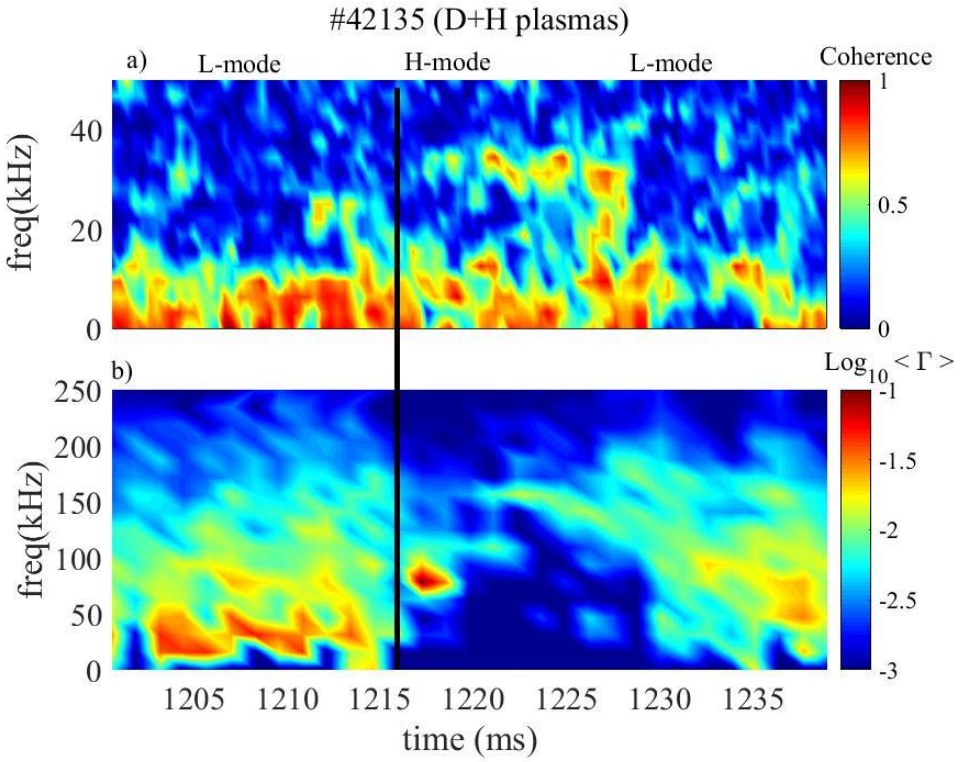

Figure 3.33 In a) is shown the evolution of cross-coherence during L-H transition. In b) is shown the frequency solved radial particle flux. Coherence for low frequencies remains in large values during L-H transition. Radial particle flux dominating frequencies are shifted to higher values in H-mode. Previously, in L-mode, particle flux is dominated by a frequency band in the order of 10 to 50 kHz (approximately). The lowest frequencies (1 to 10 kHz), dominated by Zonal Flows, do not contribute to radial particle transport in either L- and H-mode plasmas.

III.2.3.7. Discussion: turbulence control by Zonal Flows

Different mechanisms are proposed in order to understand how Zonal Flows control and reduce turbulent transport during the L-H transition:

a) *Turbulence control by Zonal Flows*: Due to its spatial structure, Zonal Flows do not contribute to radial transport. In addition, driven by turbulence, Zonal Flows constitute an energy sink for turbulence, which cause a reduction of radial transport. This hypothesis is consistent with the result shown in figure 3.33.b.

b) *Turbulence control by mean and fluctuating sheared flows:* Shearing rates induced by low frequency fluctuating Zonal Flows can be estimated by using Langmuir probes. Effective shearing rate due to Zonal Flows is calculated from $\gamma_{ZF} V_f^{ZF} / \Delta_r^2$, where γ_{ZF} is the value of long range coherence for low frequency fluctuations, Δ_r is the typical radial scale where Zonal Flows are damped and V_f^{ZF} is the peak to peak amplitude of floating potential fluctuations for frequencies below 20 kHz. Following typical values found in TJ-II for the described magnitudes the inferred value of the shearing rate in L-mode is in the order of $0.5 \cdot 10^5 s^{-1}$. This value is lower than the decorrelation level of floating potential fluctuations, which is calculated as the inverse of the auto-correlation time measured in the laboratory frame of reference and results in $\sim 3 \cdot 10^5 s^{-1}$. The obtained value for shearing rate due to fluctuating sheared flows is also lower than the value of the mean shear flow, which is estimated to be in the order of $10^5 s^{-1}$. Then, present results suggest that low frequency fluctuating flows play a marginal role to stabilize turbulence by decorrelation mechanism caused by shearing.

c) *Consequences of the synergy between NC E_r and fluctuating $E_r \times B$ sheared flows:* The influence of NC E_r on Zonal Flow-like structures has been reported in TJ-II. Also, in JET tokamak, fine structures in the radial electric field have been observed in consistency with stationary Zonal Flows. Actually, the mechanisms which sustain the observed relation between NC E_r and the amplification of low frequency Zonal Flow-like structures have been investigated and results are shown in this thesis [chapter III.1].

d) *Effects of curvature and spatial scale of radial electric fields:* The curvature of radial electric field (second spatial derivative of NC E_r) can be stronger than the effect of shear over the turbulence [194, 125]. However, for the case of the experiments shown here, the analysis of curvature of radial electric field is not possible due to instrumental limitations. Further work is needed in this direction.

III.2.4. Conclusions

In this section have been described experimental findings obtained in the TJ-II stellarator on the evidence of Zonal Flows during the L-H transition and H-mode plasmas as well as the role of isotope effect in the conditions of L-H transition in TJ-II.

LRC, as approximation of Zonal Flow-like oscillations, have been characterized in the edge plasma of TJ-II during the L-H transition making use of a dual system of electrical probes. Large levels of LRC for low frequency band (1<f<20 kHz) are present during the preceding L-mode, reaching a maximum level during the L-H transition.

Under the presence of Zonal Flows and during the L-H transition, the radial particle flux is strongly reduced in TJ-II, as reported in previous works [125, 195]. Considering the evolution of ZF-like fluctuations and the mean radial electric fields during the L-H transition, it is

concluded that Zonal Flows control turbulent transport by acting as energy sink for the low frequency turbulence and leading to the development of zero frequency sheared flows. Shearing rates due to Zonal oscillating radial electric fields (1<f<10 kHz) are clearly smaller than the shear due to the mean flow (zero frequency). This empirical findings point towards considering low frequency fluctuations in radial electric field as a triggering mechanism of L-H transition and as driving mechanism of electric fields during H-mode plasmas in stellarators.

Wavenumber spectra and mean radial electric fields measured by using Doppler Reflectometry system, level of LRC quantified by using electrical multi-probe arrays, turbulence level reduction and electron plasma temperature and density are similar for pure Hydrogen plasmas and Deuterium dominated plasmas during the L-H transition in TJ-II NBI plasmas.

III.3. Spatial structure of ZF in TJ-II: role of plasma heating, isotope effect and oscillation frequency

In this chapter we describe the spatial structure of a low frequency global potential oscillation, which is likely ascribed as the low frequency zonal flows, in TJ-II plasmas. Time-space properties of the global potential oscillation are investigated in plasmas produced by ECRH and NBI heating schemes that are characterized by different mean radial electric field structures. The radial width of the oscillating structure strongly depends on the heating scheme. Preliminary results roughly suggest that the radial width of LRC increases with the ion mass in NBI scenarios. A scientific publication has been written based on these results [196]:

III.3.1. Introduction

The low frequency zonal flows (LFZFs) and the geodesic acoustic modes (GAMs) have been intensively studied to utilize their intrinsic capability of turbulence transport regulation in fusion plasmas. A great deal of studies including experimental identifications both of the LFZFs and of the GAMs as well as theoretical modelling and numerical simulation have been performed to achieve a better understanding of the LFZFs. However, the physics of the spatial structure of the LFZF, important to estimate the efficiency of the turbulent transport self-regulation, is not still understood and validation studies are still needed.

Understanding the influence of isotope mass effects on plasma confinement is one of the most relevant open issues in magnetic confinement fusion. In most of the tokamak experiments the plasma confinement time increases with increasing ion mass under similar plasma conditions [183]. Interestingly, the isotope effect was reported to be weaker in stellarators than in tokamaks [181]. However, standard transport theories don not predict the isotope effect. Diffusive-like transport theories consider diffusivity as $D \approx L_r^2/\tau_c$, where L_r is the characteristic radial scale length and τ_c is the characteristics time scale of turbulence. If L_r scales as $L_r \sim \rho_i$, then an increase of ion mass implies an unfavorable effect on plasma confinement. A multi-scale mechanism has been proposed to explain the isotope effect [197, 198]. The basics idea is that the smallest plasma scales (controlled by the Larmor radius) can affect the development of large-scale zonal flows thus affecting plasma transport.

The isotope dependence of local plasma turbulence scale and long-range coherent structure has been studied in the TJ-II stellarator and the ISTTOK tokamak. In both ISTTOK and TJ-II, the local turbulent scale increases with isotope mass. This observation would be consistent with gyro-Bohm scaling [199, 200].

In this chapter, the influence of TJ-II plasma heating and ion mass on the spatial structure of LRC are investigated.

III.3.2. Experimental set-up and methodology

III.3.2.1. Plasma scenarios and diagnostics

Experiments were carried out in ECRH and NBI heated plasmas in TJ-II standard configuration with the edge rotational transform $\iota(a)/2\pi \sim 1.65$. Hydrogen and Deuterium (100 %) in the ECRH phase; Hydrogen (100%) and Deuterium dominated plasmas (up to 70%) were generated in the NBI heated regime.

A typical time evolution of the target discharges is shown in Fig. 3.34. At the first half of the discharge, the plasma is sustained by two electron cyclotron resonance heating (ECH) systems of the port through power of 250 kW each, deposited at the plasma center. At the middle of the discharge t = 1.15 s, the heating scheme is switched to the co-directed neutral beam injection (NBI) heating having the equivalent port through power to the two ECHs. The ECH heated plasma has a lower density and a larger particle transport (reflected in the H_α emission) than the NBI heated plasma.

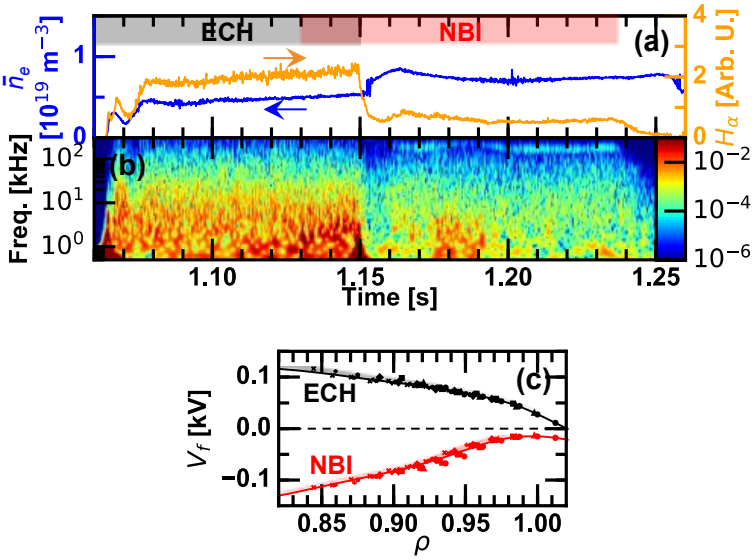

Figure 3.34 Time evolutions of (a) the line averaged density and the H_α emission intensity, (b) wavelet power spectral density of floating potential at $\rho \sim 0.9$, radial profiles of (c) mean floating potential in the ECH period and the NBI period.

III.3.2.2. Methodology: characterization of radial width of ZF

The Floating potential profile and its fluctuation are diagnosed by a couple of the Langmuir probes (probes 1 and 2) separated poloidally ~ 155 deg. and toroidally ~ 160 deg and located in sectors B and D. The probe 1, the so-called poloidal probe, consists of sixteen Langmuir probe tips, separated radially 5 mm and poloidally 3 mm. The probe 2, the so-called rake probe,

consists of twelve radially separated tips ~ 3 mm each, whose radial position is scanned within eight discharges shot-to-shot basis. The radial scan covers the range $0.82 < \rho < 1.02$, where ρ is normalized averaged minor radius. Position of the 1-probe (poloidal probe) is typically fixed at $\rho = 0.9$, for the use as the reference probe for evaluating the long range correlation with respect to the B probe (rake probe) as shown in Fig. 3.35.

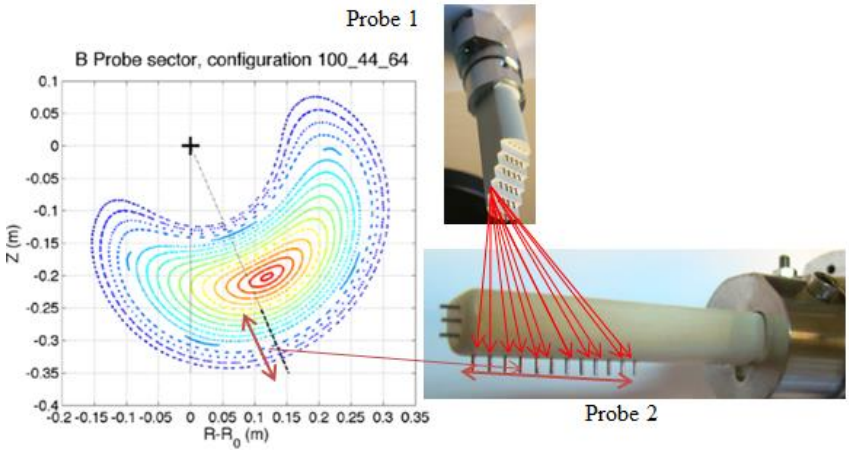

Figure 3.35 The typical shape of plasma region in TJ-II stellarator obtained by VMEC code for standard magnetic configuration and the red arrow shows the position of Lagnmuir array (probe 2) along plasma radius (left figure). In the right hand side is shown the correspondence between reference pin in probe 1 and all the pins placed at probe 2.

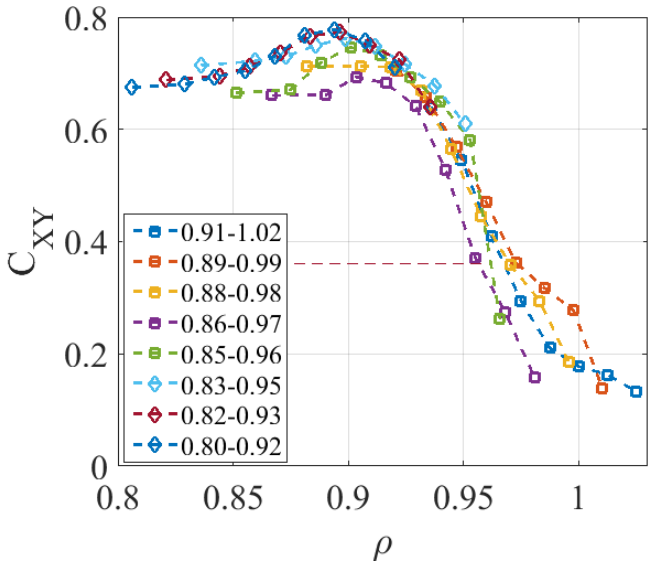

Figure 3.36 Several radial profiles of LRC obtained during the realization of a set of consecutive and highly reproducible discharges. As shown in the figure, the profile is characterized from $\rho = 1$ until $\rho = 0.8$. The case shown here corresponds to ECRH plasmas..

In the order of ten discharges have been used to measure the radial profile of LRC in both Hydrogen plasmas Deuterium dominated discharges. Then a comparison of radial width of LRCs is done for the two different cases of isotope mass ratio and for different heating scenarios

(ECRH vs NBI). In addition, the effect of E_r induced by external biasing on radial width and amplitude of ZF is also assessed in both Hydrogen and Deuterium plasmas.

III.3.3. Results and discussion

III.3.3.1. Radial profile of Zonal Flows: dependence on ion mass

Plasmas reported in this paper were obtained in two heating regimes: in the first phase plasmas were sustained by ECRH and in the second phase plasmas were sustained by co-NBI heating. In the ECRH phase line averaged plasma density is in the range $0.5 \cdot 10^{19} m^{-3}$ In both Hydrogen and Deuterium plasmas, whereas in the NBI phase plasma density increases up to $0.8 \cdot 10^{19} m^{-3}$ in Hydrogen plasmas and up to $0.9 \cdot 10^{19} m^{-3}$ in Deuterium plasmas.

Figure 3.37 shows the radial profiles of floating potential corresponding to ECRH phase and NBI phase respectively for both Hydrogen and Deuterium dominated plasmas. The points appearing in the figures result from the measurement of radial profile of V_f in sucessive discharges by probe 2 (9 Langmuir pins separated by 2 mm, in sector D), which is in fact an equivalent feature to that shown in figure 3.36 for LRC. As seen in the figures, the probe radial scan leads to a high overlapping between profiles.

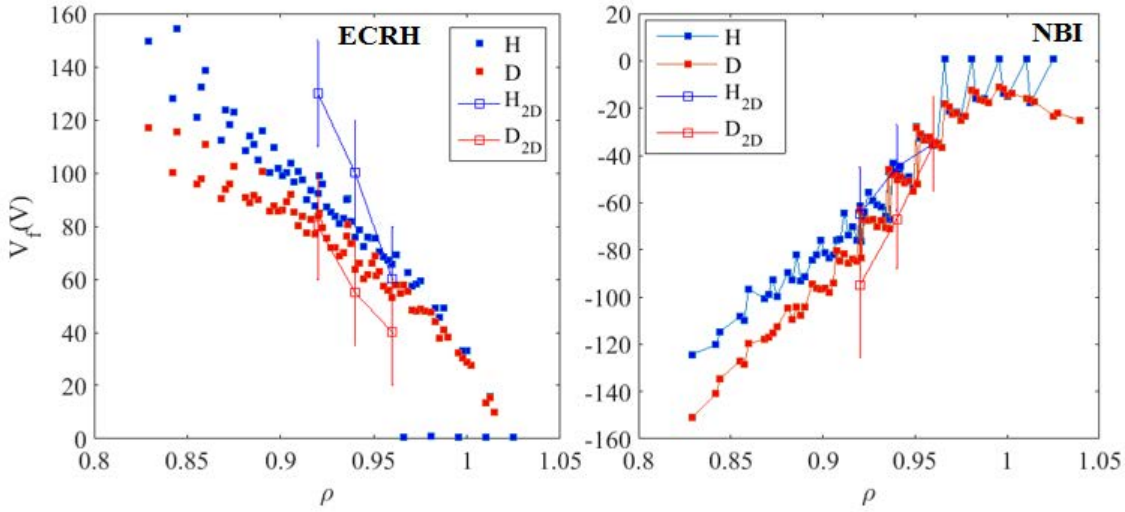

Figure 3.37 Radial profile of floating potential measured by the two distant probe systems in ECRH plasmas (left) and NBI plasmas (right). Profiles are obtained from averaging trough several discharges. In blue are represented pure the Hydrogen plasma discharges #43702/…/#43709 while in red Deuterium are indicated the dominated plasma discharges: #44202/…/#44212.

In figure 3.37 are also depicted the three values of V_f measured by probe 1, which is the reference fixed probe, for both Hydrogen and Deuterium dominated plasmas. The most internal

pin of probe 1 is used as reference signal to calculate the radial profile of LRC with all the other pin measurements from probe 2.

The floating potential is positive in the plasma edge of ECRH heated plasmas, in agreement with the electron-root solution of neoclassical predictions and negative in the plasma edge of NBI heated plasmas in agreement with the ion-root solution of neoclassical predictions. Both in ECRH and NBI scenarios, floating potential profiles show comparable values in Hydrogen and Deuterium plasmas, being floating potential values systematically lower (in the range of 20 V) in the plasma edge region ($\rho \approx 0.85 - 0.9$) in D dominated plasmas.

In figure 3.38 is shown the spatio-temporal evolution of LRC in TJ-II Hydrogen plasmas. The values are obtained from the radial scan of 10 reproducible discharges. In ECRH plasmas the radial width of LRC is clearly larger than in NBI case, which is completely measured. For the case of Deuterium dominated plasmas, similar results were obtained.

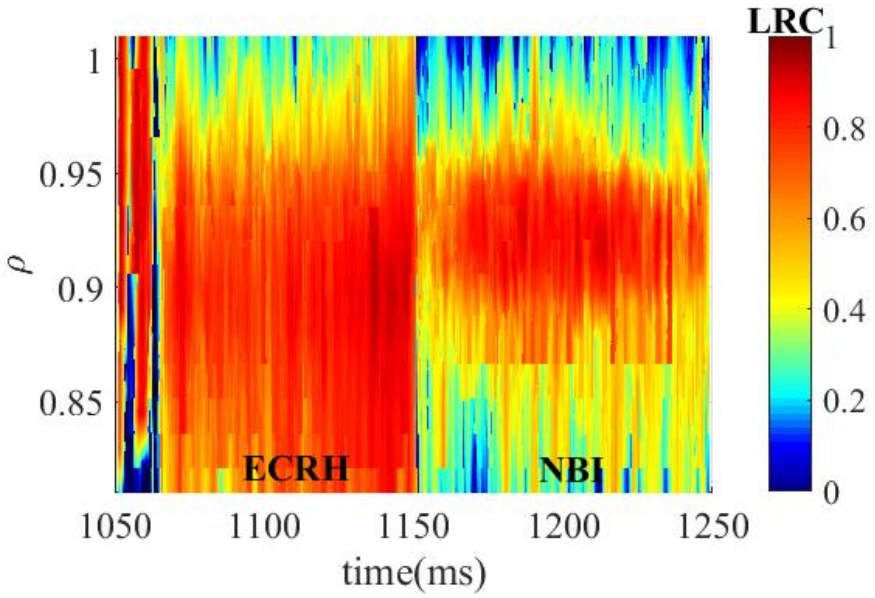

Figure 3.38 Spatiotemporal evolution of LRCs in the plasma edge of Hydrogen plasmas in the TJ-II stellarator. Radial width of LRCs strongly depends on the heating scenario. (ECRH vs NBI).

Figure 3.39 shows the radial profiles of LRC for both Hydrogen and Deuterium dominated plasmas. The radial profiles are time averaged along the duration of ECRH phase. The values of LRC are slightly higher in Deuterium than in Hydrogen in all radial positions. This leads to larger radial amplitude of LRC for Deuterium dominated discharges. In NBI plasmas, the effect of isotope mass is clear than in ECRH case. While the amplitude of LRC (maximum) is almost unaffected by changes in isotope mass, the radial width of LRC in Deuterium dominated plasmas is about a factor 1.5 larger than in the case of Hydrogen plasmas. In NBI regime, the LRC structure in Deuterium dominated plasmas shows a spatial displacement in the inward direction with respect to the structure in Hydrogen plasmas (fig. 3.40).

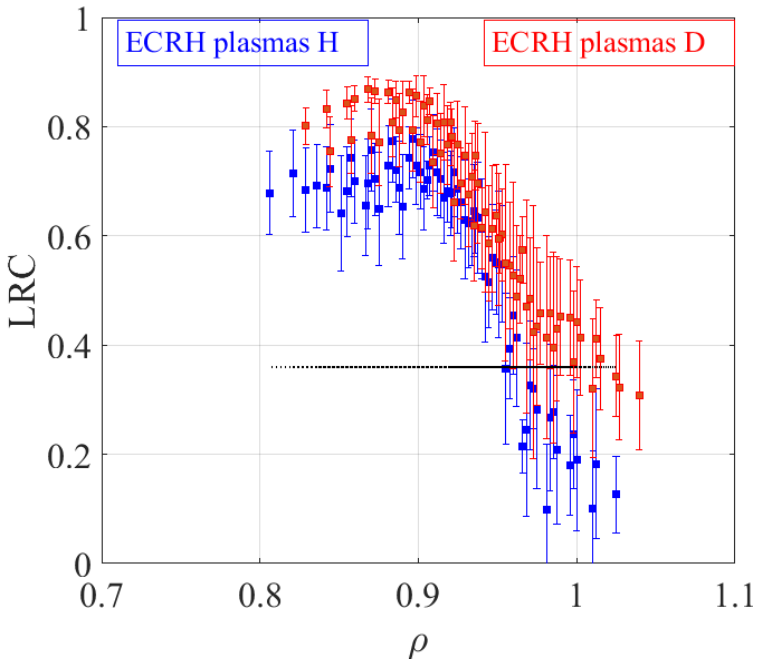

Figure 3.39 Average radial profile of LRCs in ECRH plasmas for both Hydrogen and Deuterium dominated plasmas.

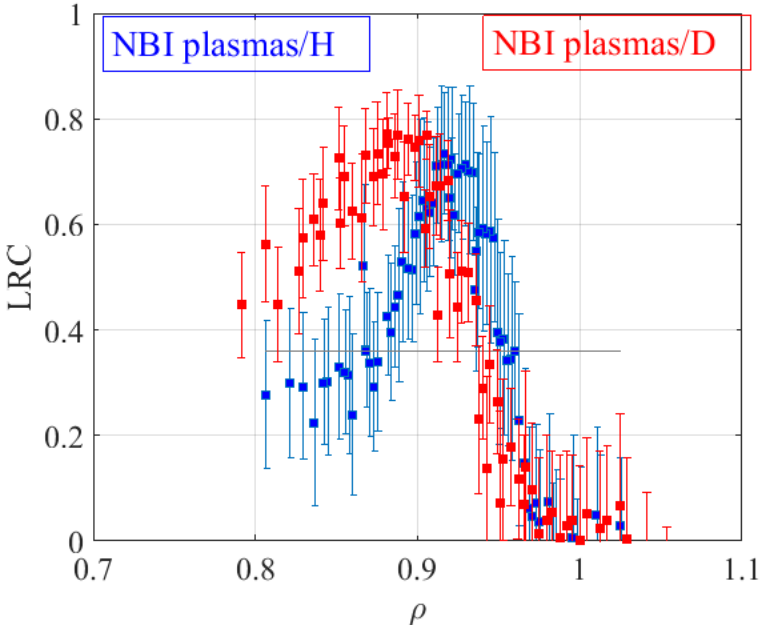

Figure 3.40 Average radial profile of LRC in NBI heated plasmas for the cases of both Hydrogen and Deuterium dominated plasmas.

III.3.3.2. Radial profile of Zonal Flows: dependence on heating regime (ECRH versus NBI)

In figure 3.41 are shown the radial profiles of LRC for both ECRH and NBI Hydrogen. In NBI heating phase the radial width of LRC has been fully characterized in the external edge region and has a value of the order of 1 cm. In ECRH plasmas, while the radially outwards decay tail is fully explored, probes have not been able to measure the complete profile radially inwards.

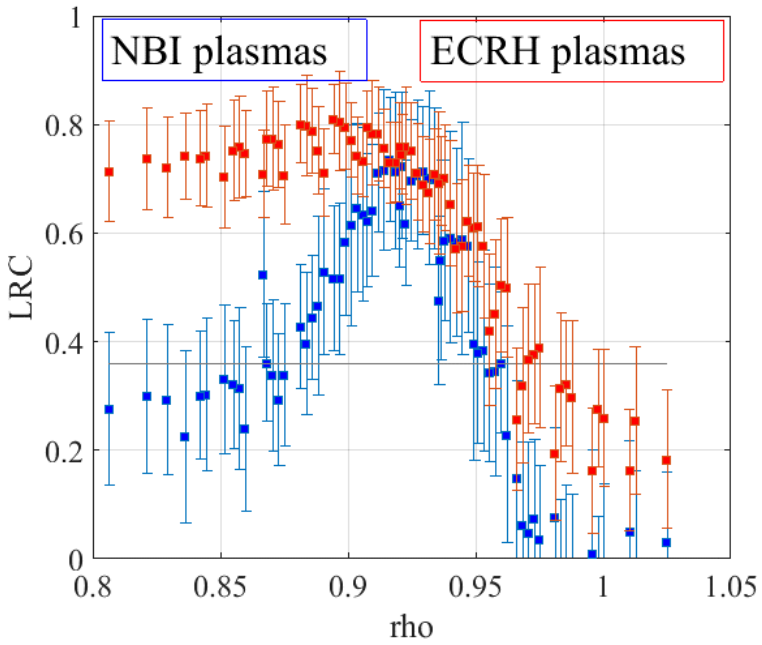

Figure 3.41 In red, average of radial profile of LRCs in ECRH Hydrogen plasmas. In blue is shown the average radial profile of LRCs in deuterium dominated plasmas.

The heating scenario strongly determines and modifies the radial width of Zonal Flow-like structures, much more clearly than the difference in isotope ion mass. For both Hydrogen and Deuterium dominated plasmas, the radial size of LRCs is larger in ECRH plasmas with respect to NBI case. On the other hand, again, the amplitude (maximum of LRC) is not affected by the heating regime.

III.3.3.3. Spatiotemporal characterization of Long Range Correlations

The spatial and temporal characteristics of the LRC have been calculated in the plasma edge ($\rho \approx 0.8 - 1$) for a range of time delays ($\tau \approx 50$ microseconds) between distant floating potential signals measured by probes 1 and 2. Measurements were carried out both in ECRH and NBI plasmas scenarios and in H and D dominated plasmas (Fig. 3.42 and 3.43).

LRCs show a maximum when the time delay is close to zero and decays when τ increases, describing the cross-correlation a Gaussian-like curve with respect to τ. LRC times are comparable in H and D plasmas. In NBI regimes the maximum in the amplitude of LRC is significantly shifted radially inwards (about 0.5 cm) in D plasmas with respect to H plasmas (fig. 3.43 right). The influence of isotope mass on the radial structure of LRC could be due to different mechanisms like the influence of ion mass on Larmor radius, neoclassical particle orbit effects and differences in wall conditioning.

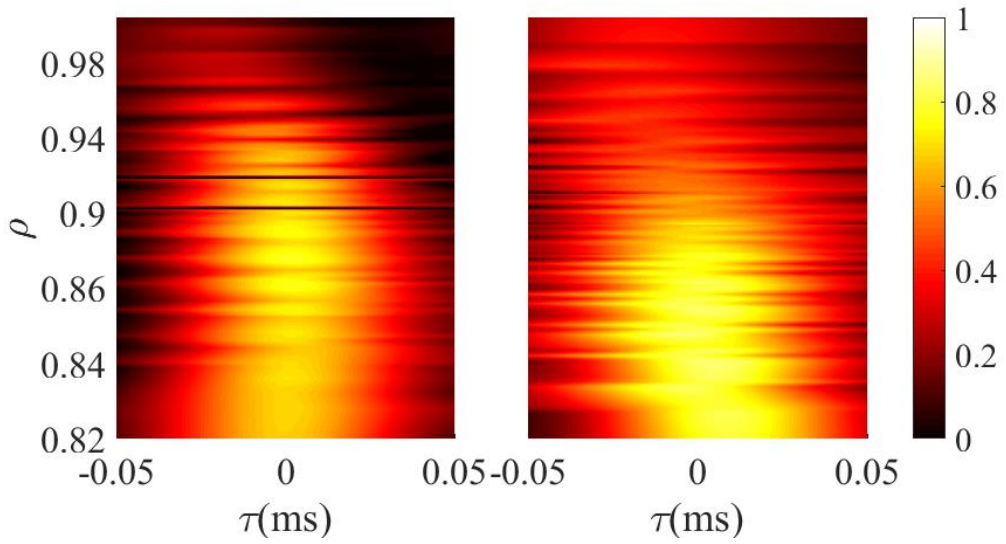

Figure 3.42 Spatiotemporal structure of LRC in ECRH plasmas for both Hydrogen (left) and Deuterium dominated (right) plasmas. Survival time of LRC is similar in both cases but there are differences in the radial width of LRC.

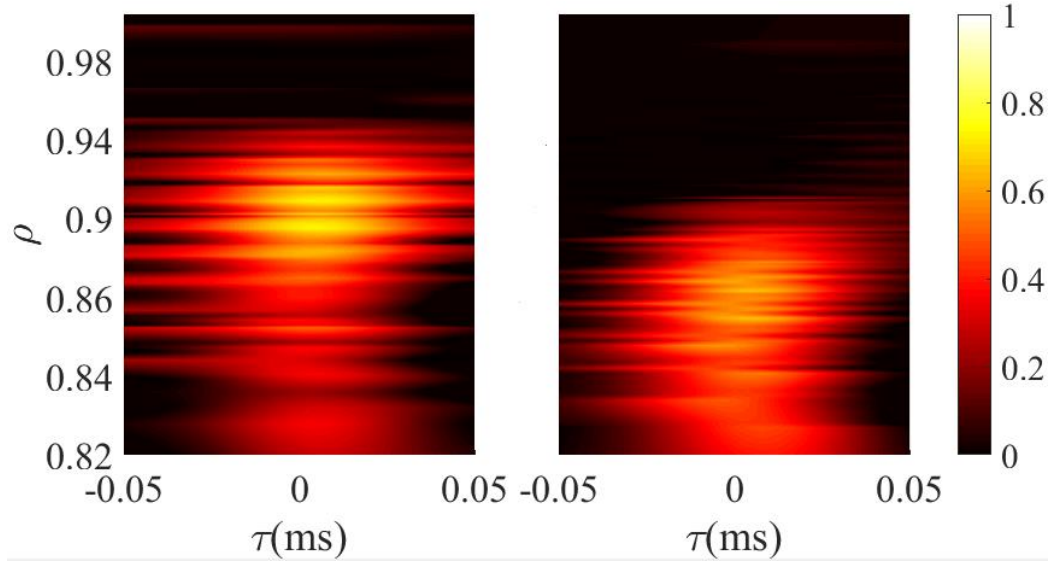

Figure 3.43 Spatiotemporal structure of LRC in NBI heated plasmas for both Hydrogen (left) and Deuterium dominated (right) plasmas. There is a shift in the radial position of the structure of LRCs.

III.3.4. Conclusions

In conclusion, we have investigated how the radial structure of low frequency Zonal Flows depends on plasma scenarios (heating and ion mass). Results reported in here show, for the first time and with unprecedented detail, how sensitive are the properties of zonal flows to plasma conditions, providing a key experimental guidance for model validation. Whether this sensitivity is due to the magnitude or sign of radial neoclassical electric fields affecting Reynolds stress driven ZFs neoclassical mechanisms or/and plasma collissionality remain an open question.

III.4. Transport at the JET plasma boundary region

III.4.1. Introduction

The JET tokamak is currently operating with the so-called ITER-like wall that mimics the one of ITER (ILW), which is meant as the plasma operation with an all-metallic wall. It has been demonstrated that this configuration is compatible with the operation in relevant high power H-mode scenarios, as scheduled for ITER (ITER baseline scenarios). Under these conditions, the wall fuel trapping in the vacuum vessel has been reduced by about one order of magnitude with respect to that in Carbon-based divertor materials [201, 202, 203, 204]. The latter led to a prohibitively large tritium accumulation due to the high reactivity of Carbon with Hydrogen isotopes (The underlying physics of retention is explained in section I.3.4).

Moreover, the high power operation H-mode regimes reached in the last JET experimental campaigns show new particularities which have not been faced during Carbon wall phase. The confinement in H-mode is reduced by at least 20 % in the so-called ITER baseline scenario with respect to the previous Carbon phase [203]. The large amount of puffing necessary to reduce the plasma edge temperature at the divertor, in order to avoid tungsten sputtering and accumulation in the plasma centre, was considered as the responsible mechanism of confinement reduction.

Recent experimental findings obtained at JET in ITER baseline scenarios (high power and best performance) show that, for specific magnetic configurations with the strike points (SP) located at the divertor corners (near the pumping conducts), the global confinement could improve [205, 206, 207]. This observation could help to clarify the role of neutrals on the degrading of the pedestal properties. It is known that the presence of neutrals in the SOL plasma could lead to the generation of a high density cool plasma at the inner divertor, which affects the dynamics of pedestal recovery after ELMs. However, there is not still a clear understanding of the physics behind it.

On the other hand, Carbon (C) and the new all-metallic wall exhibit different characteristics when are exposed to Deuterium and the physics of Recycling considerably varied [208, 209]. The absorption capacity of D in ITER-like tungsten divertor is much lower than in the previous Carbon wall phase with the exception of absorption in Berilium co-deposits, which can lead to local thermal desorption due to the power deposited during ELM's [210]. The re-emission of the neutralized ion flux by the plasma facing material, given by the Recycling coefficient, and fuelling during scenarios with ELMs determine the transport of neutrals in the SOL as well as its link with the recovery of the pedestal. The Recycling, gas injection and volume recombination are the neutral sources. During ELM's, considering that the Recycling coefficient remains close to the unity is generally accepted as a good approximation [211]. However, the time evolution of R (along temporal scales of the order of several miliseconds) has been empirically studied in Carbon wall devices [212] as well as simulated for the case of W divertor [213] and measured specifically in the case of W divertor exposed to ELMs [214].

We present here results that show indications of Recycling coefficient varying along the ELM's instabilities during JET H-mode plasmas.

III.4.2. Results and discussion

III.4.2.1. Relation between Neutral fluxes and Divertor configuration in JET H-mode plasmas

In figure 3.44 are shown two different divertor magnetic configurations to study: vertical (V), with the inner SP at the inner vertical divertor target and corner (C), in which the inner SP is placed in the divertor corner, close to the pumping conducts. During the discharge #86533 (toroidal magnetic field of 2.4 T, toroidal plasma current of 2.5 MA, 17 MW of NBI heating power and 1.5 MW of ICRH heating power) the plasma starts first with the C-configuration and is moved after 2 seconds to the V-configuration during the H-mode.

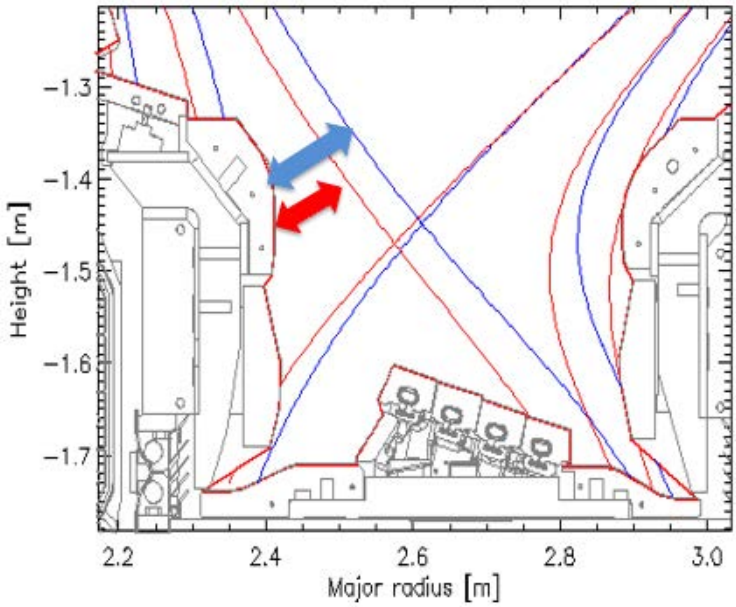

Figure 3.44 JPN 86533. In red, vertical (V) configuration and distance from the LCFS to the inner divertor plate. In blue, the same for the corner (C) magnetic configuration.

In figure 3.45 is shown the influence of magnetic configuration on the time evolution, of some global plasma parameters and characteristics (#86533). Specifically are represented, NBI power P_{NBI}, fuelling Q_0, plasma average density $\langle n_e \rangle$, pedestal electron temperature T_e^p, total BeII emission at the inner divertor, enhanced confinement factor H_{98Y} (indicator of the confinement quality) and integrated inner and outer divertor D_α radiance. The transition of magnetic configuration from corner (C) to vertical (V) is done at t = 49 – 50 seconds. As shown in figure

3.45.a) even when the puffing rate is reduced during V-configuration with respect to C- one, plasma density increases. The confinement is clearly degraded in V-configuration with respect to C- one as shown by a decrease of about 20% in the confinement factor and a reduction in T_e^p of about 30%. Considering only the inter-ELM phase, during the C-configuration the global ion fluxes at the inner divertor are a factor of 2 higher than the fluxes at the outer divertor. Once in the V-configuration, global D_α radiance in the inner divertor are roughly ten times higher than in C-configuration, which suggests that are indications of a stronger neutral flux is reaching the inner part of divertor, while in the outer part of the divertor the flux is increased by a factor of 3 (see figure 3.48).

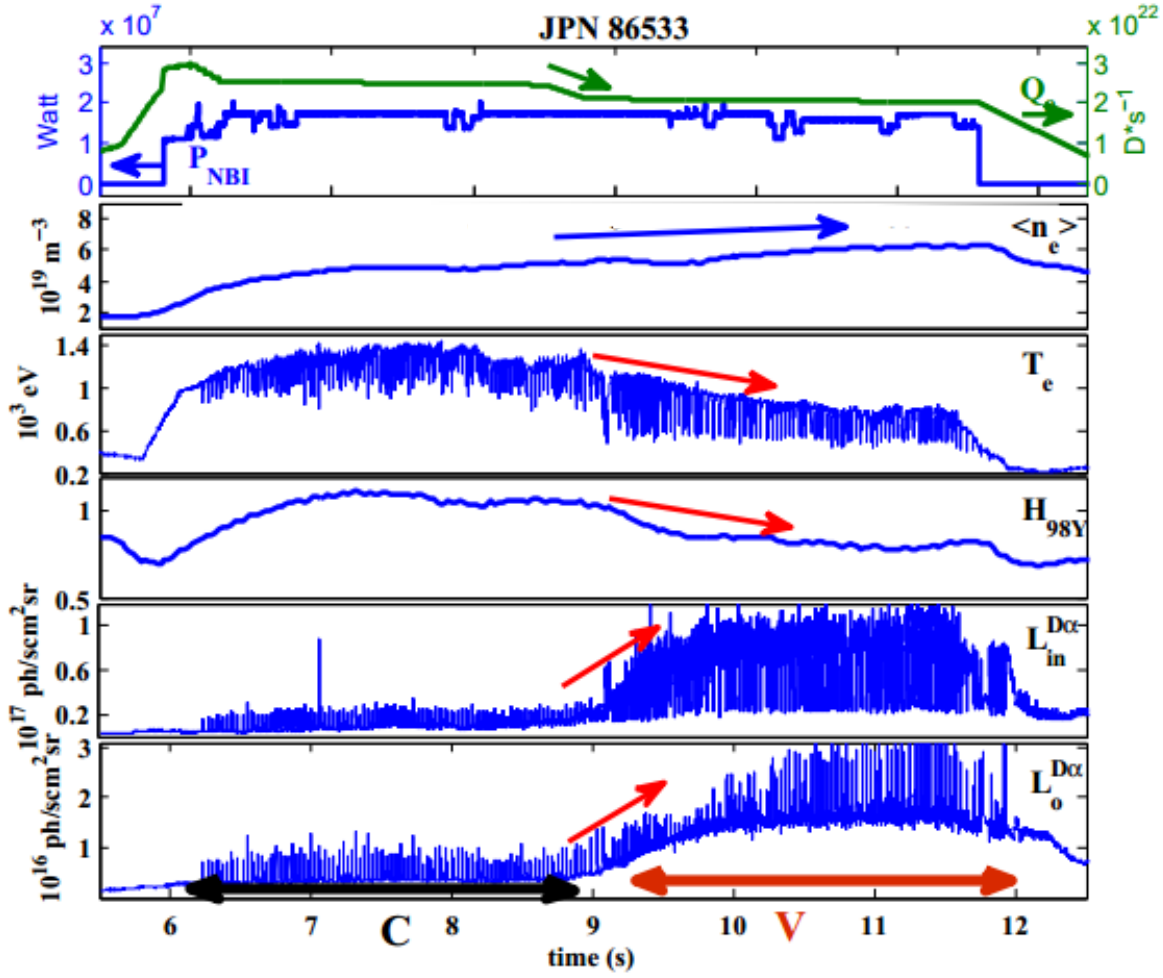

Figure 3.45 Time traces of the main plasma parameters of JPN 86533 (See text).

Figure 3.46 (left hand side) shows two frames of the divertor taken with the KL8 Fast camera during the V-configuration of #86533: left before the ELM and right after the ELM and below the view of the camera to the divertor. The lines indicate schematically the different emission regions showing in red the outer SP, in blue the inner SP and in yellow the upper inner divertor region where a strong emission-cloud appears at the HFS just after the ELM. The spatial localization of these emission regions where done applying the "Cross-correlation technique"

between different ROIs (Region of Interest) of the Fast Camera videos and the spatially-well defined D_α-chords looking from the upper port to the divertor [143]. The camera had no filter for this discharge but the dominant emission at the divertor is by far D_α-line emission. A proof of this is the high cross-correlation yield with the D_α-spectroscopy channels once the correct lines were obtained. Also, videos of similar discharges with and without D_α-filter are nearly equal, except a higher intensity level without the filter by a factor of about two because of the filter transmission losses. The camera was operated with 10 μs exposure time and 25 kHz recording speed. Figure 3.46 (right hand side) shows two video-clips that can be reproduced by clicking on the pictures, above the one of the Corner- and below of the Vertical-configuration. The clips show two ELM cycles, corresponding to about 50 milliseconds of plasma time. The movement of the image is due to the ELMs that produce vibrations on the camera supporting structure fastened to the Tokamak vessel. In the C-configuration the ELMs are faster recovering the inter-ELM equilibrium pattern much rapidly than in the V-configuration, where a strong dominating emission cloud appears at the HFS just after the ELM-crash. This cloud is located at the upper inner divertor region on top of Tiles 0 and 1 as shown in figure 3.46 (left hand side top).

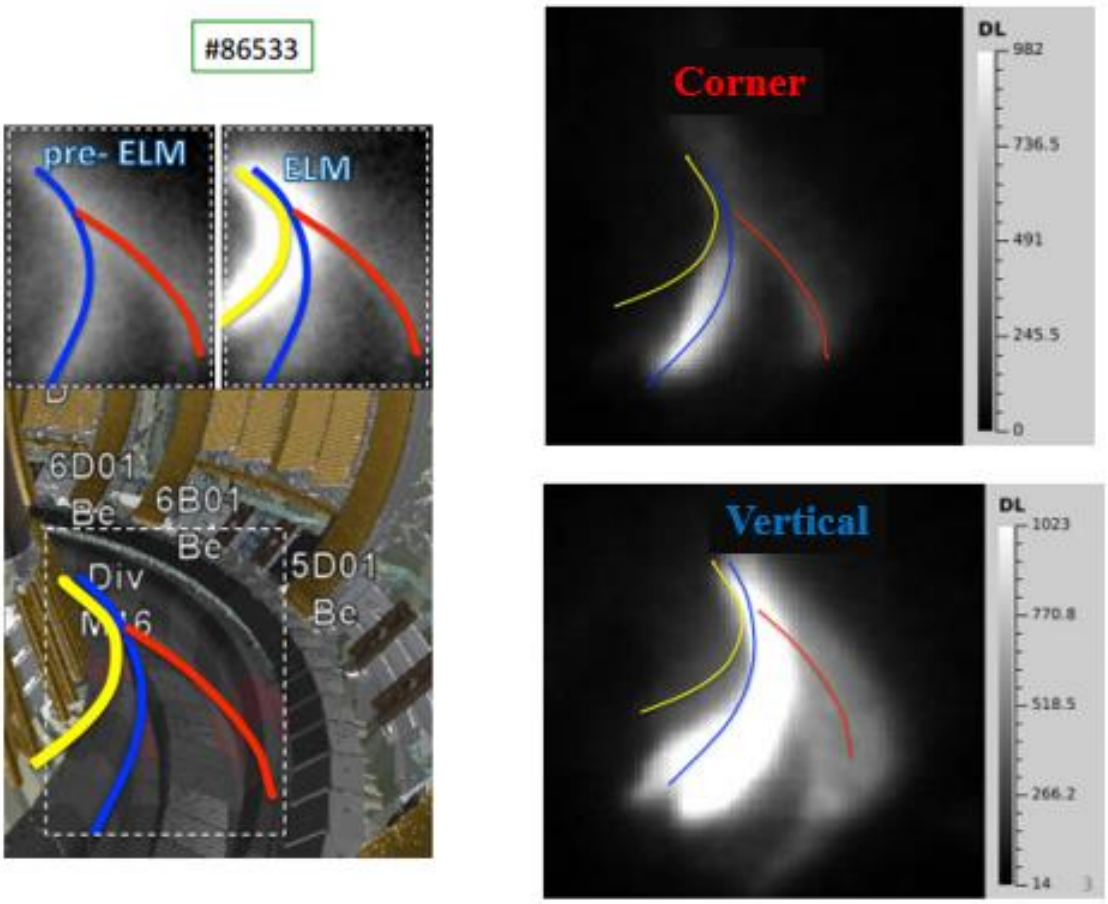

Figure 3.46 Left hand side figure shows the area of the ROI recorded by the KL8A fast visible camera (bottom) and two frames of pre-ELM and ELM phases captured during JPN 86533. The right hand side figure shows two frames recorded during the ELM in both C (top) and V configuration (bottom)

Links to videos:

CORNER:

http://www-fusion.ciemat.es/fileshare/doc_exchange/camaras/JET2018/Fig3b_Corner.mp4

VERTICAL:

http://www-fusion.ciemat.es/fileshare/doc_exchange/camaras/JET2018/Fig3b_Vertical.mp4

The ELM D_α-dynamics during the stationary phases of the C- (t < 49 s) and V- configuration (t > 50 s) is shown in fig. 3.48 (up right) for channels 1, 3, and 5 (see figure 3.47) and below the total inner divertor WI radiance.

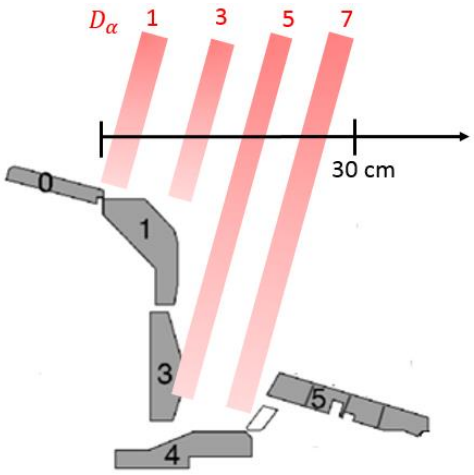

Figure 3.47 Scheme of the position of D_α radiance chords along the inner divertor.

The ELM frequency is of about 40 Hz in both phases. In the C-configuration all D_α-channels have positive peaks during the ELM crash. Also a secondary peak appears for the views that look to the SP. In the V-configuration the emission patterns completely change. The innermost two channels that look to the inner upper horizontal divertor (Tile 1, only Channel 1 is plotted) show a strong and slow emission peak that lasts about 5 ms, similar or even larger in intensity than the primary one corresponding to the ELM-crash. It corresponds to the post-ELM emission cloud seen with the Fast camera. Channel 3 that looks to the inner divertor corner shows no clear peak during the crash but also sees the secondary peak. Near the inner SP, the emission decreases just at the ELM time and during about 8 ms (Channel 5, red arrow). These so-called "negative ELMs" are characteristic of a (partly-) recombining, cool and high-density SOL plasma that develops near the SP [215].

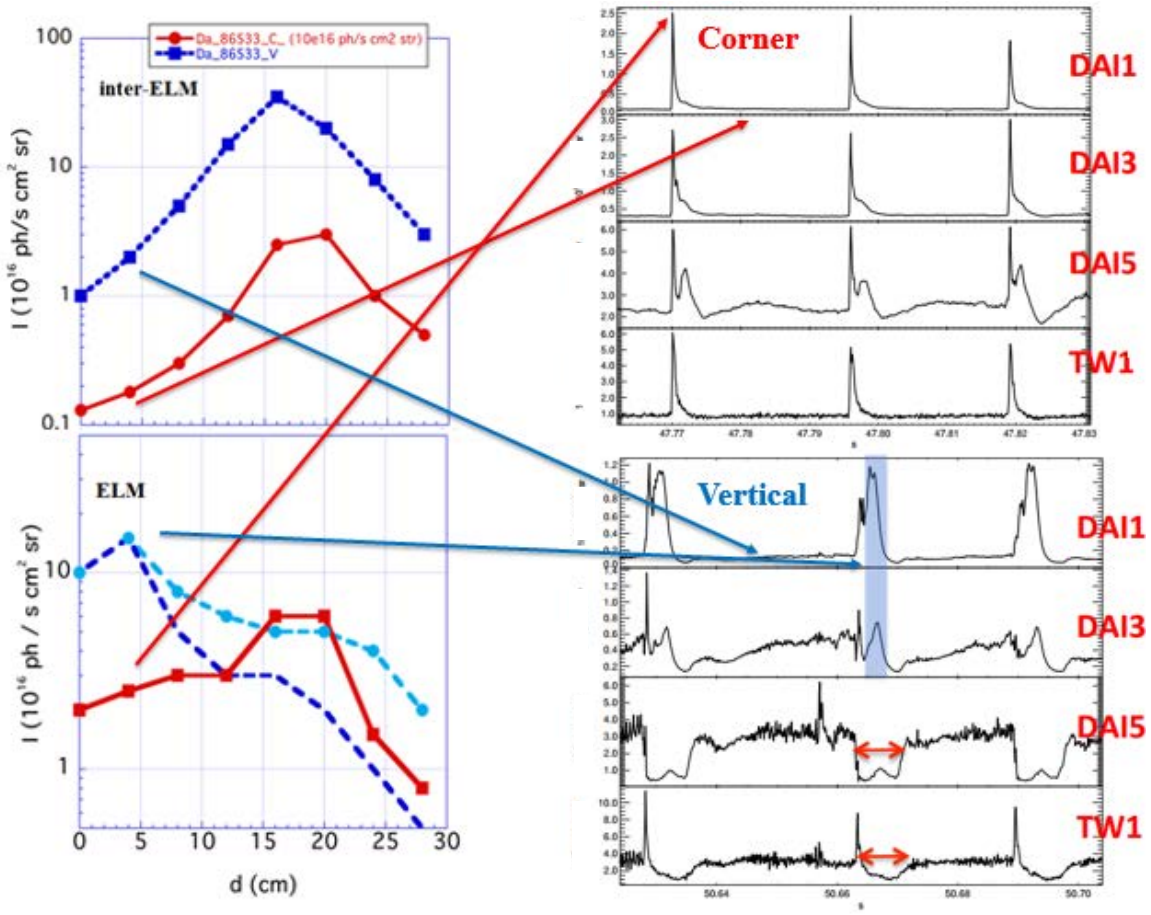

Figure 3.48 Spatial profile of D^{α} emission in Corner (blue) and Vertical (red) magnetic configuration. In the left, the emission during inter-ELM phase, and in the right hand side the emission profile during ELM crash.

The present study indicates that surface heating of Tiles 0 and 1 by high power plasmas with certain divertor magnetic configurations produces significant deuterium desorption there. This additional neutral flux may be an actuator that affects the SOL plasma properties producing at the HFS a high-density, low-temperature plasma that can be the origin of the global confinement degradation, in addition to the neutral pumping efficiency change that is linked to the SP position with respect to the divertor openings as disclosed in prior works [216]. We propose that the Clearance reduction at the upper inner divertor corner of Tile 1 triggers the power load and subsequent surface temperature increase there. This induces the local fuel desorption in this area where thick Deuterium containing Beryllium co-deposits exist. Laboratory analysis showed that these layers emit the trapped Deuterium if threshold temperatures are exceed that have been observed in the analysed plasmas [217]. With the increased neutral fluxes, the SOL plasma increases its density and cools down, making recombination possible (Negative ELMs, fig. 3.48) and even could be detached from the divertor targets.

Neutral Flux estimation and global particle Balance at the inner divertor

Figure 3.49 shows the S/XB coefficient for D_α (number of ionizations of neutral D and D_2 per emitted photon, section II.2) as a function of ne and T_e [95], being the red marked region the typical operation window of JET SOL Divertor plasma for attached conditions in H-mode (10^{19} < n_e (m^{-3}) < 5x10^{19}; T_e > 5 eV). For these plasma parameters, 8 < S/XB < 20 (see red marked region in figure 3.49) and to simplify, we remove the ne- and T_e-dependence and we take an average value **S/XB ≈ 15 and the maximum error is +/- 50**%. This is done because the exact n_e and T_e distributions are not known and therefore only a rough estimation of the fluxes is possible. Then, we assume that under these conditions recombination is insignificant and does not contribute to the neutral fluxes. In the following lines we demonstrate the validity of this hypothesis for the case of the C-configuration.

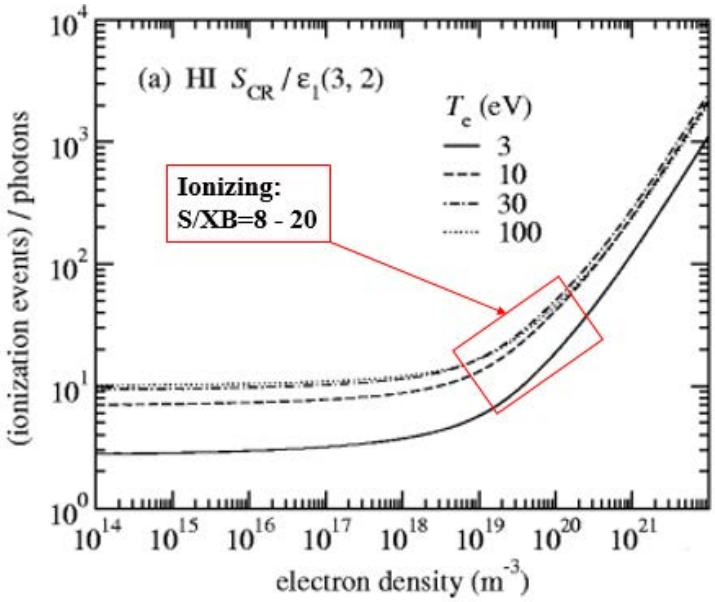

Figure 3.49 S/XB dependence on the electron density and temperature [94]. The red box indicates the range of S/XB of a plasma in attached conditions, dominated by ionizing processes.

Figure 3.50 shows schematically the Neutral and Ion fluxes in the SOL Divertor. F^0_{recy} is the neutral flux from recycling, F^0_{reco} is the neutral flux created by volume recombination, F^0_{puff} is the neutral flux from puffing at the divertor and F^0_{pump} is the pumped neutral flux.

The global neutral flux in the SOL divertor region is given by:

$$F^0 = F^0_{recy} + F^0_{reco} + F^0_{puff} - F^0_{pump} \quad (3.17)$$

As seen in the figure 3.45, during the C-phase, $dn_e/dt \approx 0$, then the discharge is in steady-state and $F^0_{puff} \approx F^0_{pump}$. In consequence, the global neutral flux in the divertor is the summation of the Recycling and recombining neutral fluxes.

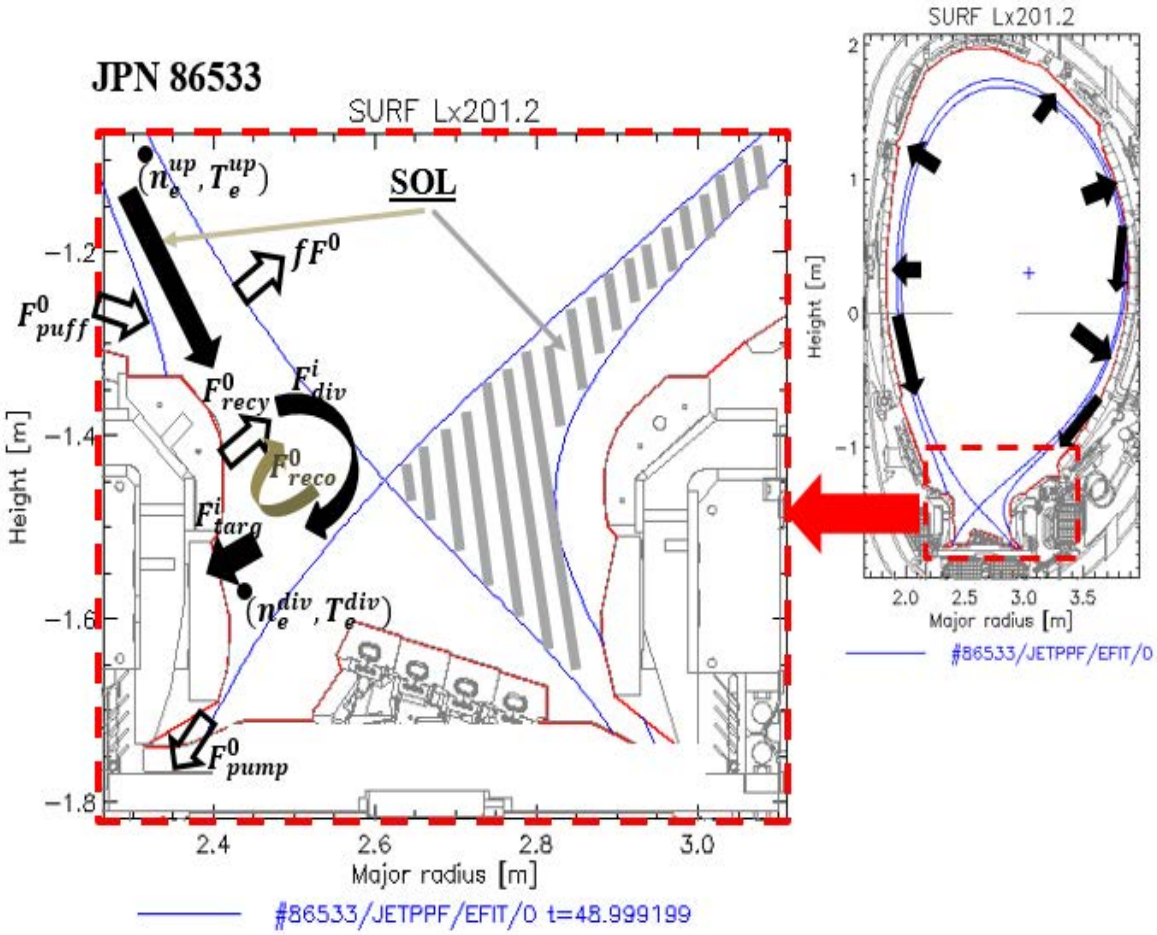

Figure 3.50 Divertor region in High Recycling Regime.

The ion flux arriving at the divertor target F^i_{targ}, is:

$$F^i_{targ} = F^i_{LCFS} + F^i_{div} - F^0_{reco} \tag{3.18}$$

Where F^i_{LCFS} gives the ion flux escaping the confined plasma diffusing out of the separatrix and entering in the divertor SOL(fig. 3.48 right hand side), F^i_{div} is the ion flux created in the divertor SOL plasma by ionization of neutrals and F^0_{reco} counts for the ion losses in the divertor Volume due to recombination.

The total ion plasma flux diffusing out from the confined plasma across the separatrix is given by F^i_{LCFS}:

$$F^i_{sep} = \langle n_e \rangle \frac{V}{\tau_p} \tag{3.19}$$

where V is the plasma volume, $\tau_p$is the particle confinement time (about 300 ms here) and $\langle n_e \rangle$ the average density. In an H-mode plasma, this ion flux is an average over the whole ELM-period. However, it can be demonstrated, that the time integrated inter-ELM period ion flux

dominates over that of the ELM-crash [110]. Further, we can say that roughly one half of this value is directed to each of the divertor targets (inner and outer).

Also, following the general assumption that the Recycling coefficient is $R \approx 1$, we have:

$$F^0_{recy} = RF^i_{targ} \approx F^i_{targ} \tag{3.20}$$

Finally, the fuelling efficiency, labelled as *f*, is defined as the fraction of the total neutral flux, F^0, escaping the SOL and entering into the confined plasma and becomes ionized. Making use again of the stationary conditions ($dn_e/dt \approx 0$), this fraction of the neutrals needs to be balanced by the ion losses of the confined plasma region, given by F^i_{LCFS}:

$$fF^0 = F^i_{LCFS} \tag{3.21}$$

Depending mainly on the electron temperature, T_e, divertor, which is directly linked to the atomic reaction rates, we can identify basically two regimes:

First, if $T_e > 5\ eV$ in the divertor, recombination is negligible and we are in ***Ionizing conditions and the divertor SOL plasma is attached***. In these conditions, the dominant neutral flux term is Recycling. In these conditions we can estimate F^0 using the *S/XB* method (see section II.2)**:**

$$F^0 \approx F^0_{recy} = \frac{L^{D_\alpha}_{exc} A\Omega S}{XB} \tag{3.22}$$

Second, if $T_e \leq 5\ eV$ recombination processes may begin to be significant (depending on the electron density), and we have ***partly Recombining conditions*** and both neutral flux terms F^0_{Recy} and F^0_{reco}, must be considered or even ***completely Recombining conditions***, when no ions at all arrive to the targets ($F^i_{targ} \approx 0$), this being only possible if $T_e < 1eV$. In thee two cases the S/XB method cannot be used and the estimation of neutral flux is much more complicated (out of the scope of this work).

The particular case of JPN 86533

As already said, F^i_{targ} is a known parameter and for JPN 86533 it is $F^i_{targ} > 0$, which ensures that we have Ionizing or partly recombining conditions. We first assume that we are in ionizing conditions and calculate F^0 from equation 3.22. If the estimated value is close to F^i_{targ}, then equation 3.20 is fulfilled, which confirms that we are in Ionizing conditions with no recombination. However, if $F^0 > F^i_{targ}$we have partly recombining conditions and we ca not use the neutral flux estimation from equation 3.22.

In the case of the **C-configuration** we get, from equation 3.22, that $F^0 \approx 5 \cdot 10^{22} s^{-1}$, with the measured $L^{D\alpha} \approx 8 \cdot 10^{15} phs^{-1} cm^{-2} sr^{-1}$. On the other hand we have, in the inter ELM. The measured $F^i_{targ} \approx 5 \cdot 10^{22} s^{-1}$. Then, $F^i_{targ} \approx F^0$, so it is confirmed that we the divertor is under ***ionizing conditions*** (attached divertor). Note that, since $F^0_{puff} \approx 2.5 \cdot 10^{22} s^{-1}$, the neutral recycling flux is larger by a factor of two than the fuel puffing rate. On the other hand,

assuming a particle confinement time of 300 ms and that about half of the confined plasma ion losses crossing the separatrix are directed to the inner divertor target, from 3.19 we get that the ion flux directed to the inner divertor volume is $F^i_{LCFS} \approx 10^{22} s^{-1}$. Then, the ion flux arriving at the target becomes amplified by a factor of 5 with respect to the ion flux lost across the separatrix. This amplification is basically due to the ionization of the recycled neutrals and the subsequent parallel transport of these ions to the targets, which corresponds in equation 3.18 to $F^i_{div} \approx 4 \cdot 10^{22}\ s^{-1}$. These recirculating flow in front of the target generates there a local plasma that has an increased n_e^{div} much higher than the upstream SOL plasma n_e^{up} and a local temperature T_e^{div} much lower than the upstream T_e^{up}. This scenario is known as ***High Recycling Regime.***

Concerning the fuelling efficiency at the inner Divertor, ***f,*** a higher limit can be established. The total neutral fluxes entering inside the LCFS is the summation of the contributions from the inner and outer Divertor plus that of the puffing. In stationary plasma density conditions, which is the case here, the sum of these three terms must balance the ion fluxes escaping the LCFS (see eq. 3.21). Since $\mathbf{F^i_{LCFS} \approx 2.5\ x10^{22}\ s^{-1}}$ and $\mathbf{F^0 \approx 5\ x10^{22}\ s^{-1}}$ we get **f < 0.5**. This is however just a higher limit, since the other two fuelling contributions (outer Divertor and puffing) were not considered.

Finally, in the **V-configuration**, we have a ten times larger $L^{D\alpha}$ radiance ($L^{D\alpha} \approx 8 \cdot 10^{15} phs^{-1}cm^{-2}sr^{-1}$) and only a factor of four larger ion flux to the targets ($F^i_{Targ} = 2x10^{23}\ s^{-1}$). Therefore $F^0 > F^i_{targ}$ and we have partly Recombining conditions so the estimated neutral flux cannot be calculated with the S/XB method. The fact that recombination is important indicates that a cool plasma with high neutral and plasma density is formed at the inner Divertor, a clear signature being the "negative ELMs" in D_α −channels. The origin could be a reduction in the pumping speed caused by the SP change that moves away from the Corner or an increased local outgassing from surface heated regions, e.g. Tiles 0 and 1, as proposed above. The result is a roll-over from the High-Recycling Regime towards so-called **partial Detachment** when going to V-configuration.

III.4.2.2. On the possible temporal variation of Recycling during ELMs

In this section we will analyse in detail the dynamic behaviour of ion and neutral fluxes during the EL-cycle. As demonstrated before, during C-configuration, in the inner divertor SOL plasma is attached and atomic processes in the divertor SOL are dominated by ionization and e^-collision excitations processes and high recycling conditions. The recycling coefficient R, which has been defined as the ratio between the total neutral flux re-emitted from the surface, F^0_{recy}, and the incident D^+ion flux, F^i_{targ}, has been calculated in the time scales in which ELM happens.

F^i_{targ} is directly inferred from Langmuir probes through I_{sat} and F^0_{recy} can be estimated from $L^{D\alpha}$ using equation 3.23, as we are in ionizing conditions:

$$R = \frac{F^0_{recy}}{F^i_{targ}} = \frac{4\pi AS/XB \cdot L^{D\alpha}}{F^i_{targ}} \tag{3.23}$$

where 4π and A are known constant values, and F^i_{targ} and $L^{D\alpha}$ are directly measured quantities. On the other hand, the value S/XB depends on n_e and T_e, whose value is actually unknown. In attached ionizing divertor plasmas, in where this technique is valid, electron density and temperature have values of $n_e \approx 10^{19} m^{-3}$ and $T_e > 5eV$, respectively.

In this section we will analyse in detail the dynamical behaviour of ion and neutral fluxes during the ELM cycle. The observed differences in their time behaviour leaves us to the discussion whether the Recycling coefficient varies within this time scale. There are some recent experimental [212] and theoretical [213] studies that deal with the same question. We present here preliminary results on the evolution of the recycling coefficient during ELMs in JET H-mode plasmas.

Analysis of ELMs: Conditional averaging

In the discharge #86533, during the C-configuration, ELMs have frequency of about 40 Hz. In the figure 3.51 is shown the temporal evolution of the following magnitudes during a period of $\approx 100\ ms$ which contains six ELMs: First, BeII impurity emission line localized at a region locate at the upper divertor corner (Fig. 3.51 top). Second, D_α radiance collected by spectroscopic line which looks to the innermost LP located at the same region (Fig.51 centre). And finally, the ion flux inferred from the ion saturation current collected by a Langmuir probe which is placed in the same region of the divertor (Fig 3.51 bottom). The three quantities are obtained during a time interval of about 500 ms within the C-configuration. The ELM crash is perceptible in the impurity signals such as Berilium (Be II) and Tungsten (not shown here) from the sputtering generated by the energetic particle flux due to ELMs. At the peak of the ELM crash the global ion flux reaches values of $10^{23}\ s^{-1}$ and then it decreases again to its previous value during the pre-ELM phase.

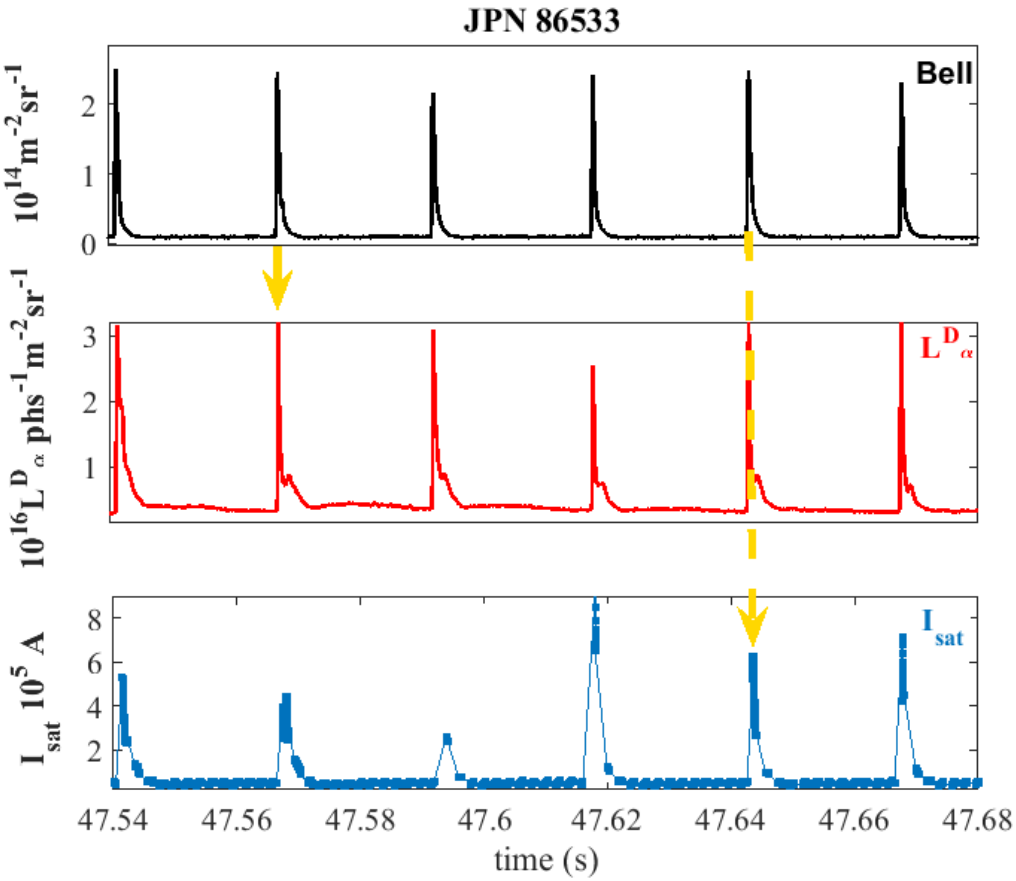

Figure 3.51 In the top, the evolution of BeII impurity emission. In the center, $D_\alpha$radiance evolution from the inner upper divertor during ELMs in corner configuration. The bottom figure shows the evolution of ion saturation current during ELMs. The signal is discontinuous.

As seen in figure 3.51, the BeII signal will be used as time reference for the ELM beginning. While the $L^{D\alpha}$ radiance is a continuous signal, the ion flux time trace (middle figure) is discontinuous because it is obtained from the ion saturation I_{sat} branch of a Langmuir probe, which describes I-V curves with a frequency of 100 Hz (figure 3.51 bottom). In addition, I_{sat} signal contains turbulence information and noise. In addition, ELMs are quasi-periodic events which show, within their respective family or type, some differences when comparing one by one.

In order to reconstruct an average and continuous signal of I_{sat} (F^0) and F^0 of the ELM we use a Conditional Averaging method. This analysis is done as follows:

1) We select a time period with stable plasma parameters (47.5 < t < 48 s) and sufficient number of ELMs, 20 in the present analysis..

2) BeII emission signal in the inner divertor is used to identify the exact instant of each ELM-crash t_{ELM} by imposing a double condition based on the detection of a change on its time

derivative above a certain threshold together with the existence of a maximum within the immediately later time interval of 2 ms.

3) Points placed within an interval from 5 ms before t_{ELM} to 25 ms after t_{ELM} of F^i and $L^{D\alpha}$signals are stored in two matrixes whose number of columns corresponds to the number of ELMs existing within t =47.5 - 48 s.

4) The time traces corresponding to $L^{D\alpha}$ signal are multiplied by S/XB and geometrical factors in order to convert it to neutral flux (equation 3.24). We will assume that S/XB = 14 and is constant over the whole ELM-cycle, so we define F^{o*} as the neutral flux with this assumption. At the end of this section we are going to analyse its possible variation.

$$F^{o*} = L^{D\alpha} \cdot S/XB \cdot 10^4 \cdot 4\pi \quad (3.24)$$

The result of the Conditionally Averaged ion and neutral fluxes is shown in Figure 3.52 a).

Let's look at figure 3.52 in detail, where we have zoomed the first 5 ms (3.52.b) and the subsequent 15 ms (3.52.c). We define the following phases of the ELM-cycle:

- The **ELM-crash**: It lasts about 1 ms and is characterized by the steep peak of F^i and F^{o*}, and also of the BeII (and WI, not shown) emission. It corresponds to the time where the energetic ions from the Pedestal region are expelled and diverted towards the divertor targets (and also to the First Wall). In this period $F^i > F^{o*}$.

- The **post-ELM**: In this period of about 5 ms after the ELM-crash we observe significant changes in the ion and neutral fluxes and $F^i > F^{o*}$. At the end of this phase $F^i \approx F^{o*}$.

- The **Equilibration phase**: It is characterized by small variations of the fluxes (< 20 %) and finishes with the arrival of the next ELM. In this period $F^i < F^{o*}$.

As seen in the figure 3.52.b, in the pre-ELM phase, the local value of ion flux measured at the location of the Langmuir probe is of about $5 \cdot 10^{21} s^{-1}$. On the other hand, the radiance has a value of $L^{D\alpha} = 3 \cdot 10^{15} phcm^{-2} s^{-1} sr^{-1}$(Figure 3.51). This value is converted to neutral flux making use of equation 3.23, resulting is $F^0 \approx 5.4 \cdot 10^{21} s^{-1}$, which is a close value to the received ion flux. This is in agreement with High recycling conditions that have been previously demonstrated, where $F^0_{recy} \approx F^i_{targ}$.

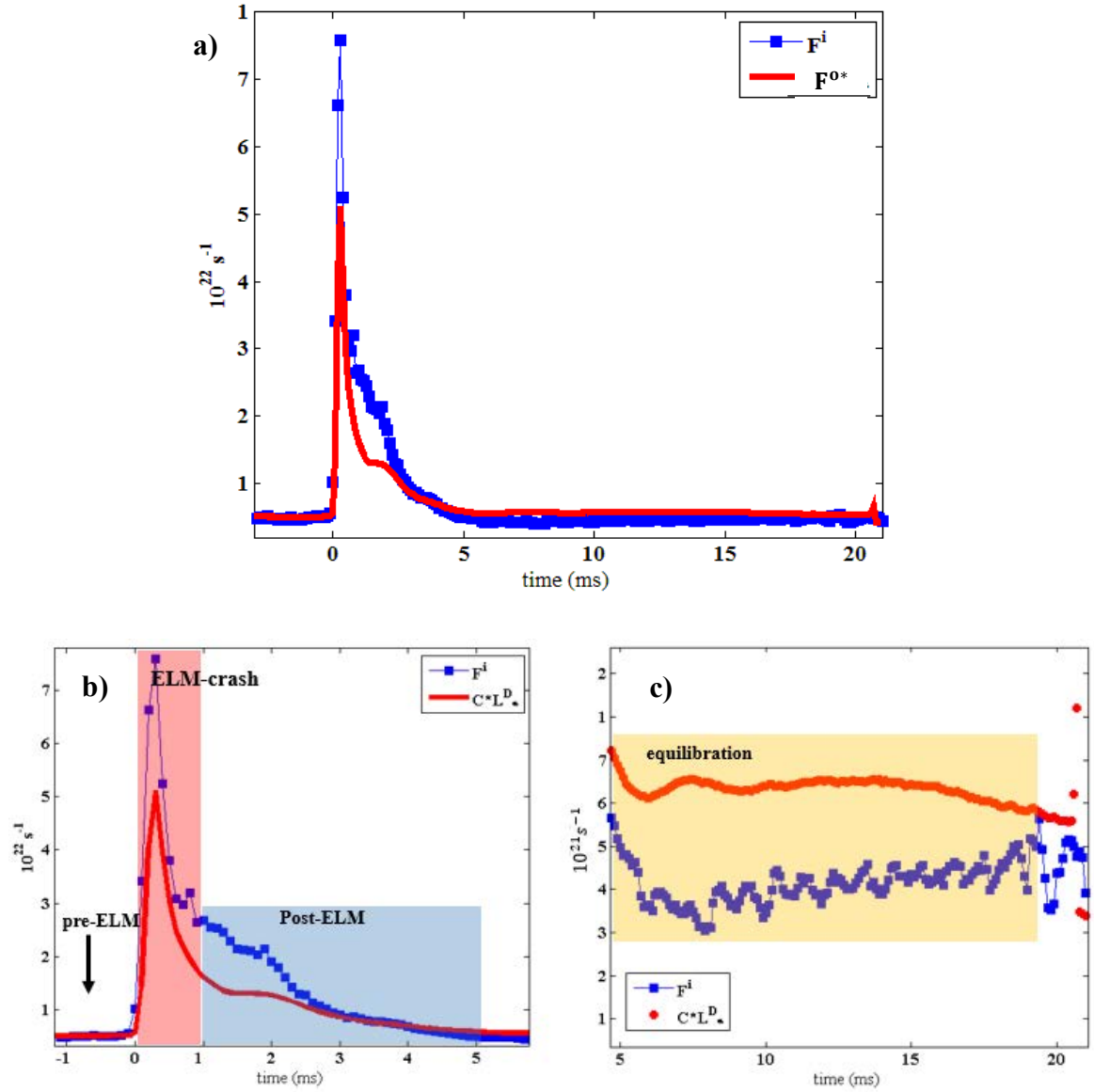

Figure 3.52 Above, evolution of the incident ion flux F^i (blue) and the neutral flux F^0(red) in divertor tile I. Bottom left figure shows the pre-ELM phase, ELM crash phase and the equilibration phase. In the righ hand side bottom figure is shown the post-equilibration phase (shadowed in red), in where the neutral flux is clearly above the ion flux.

Analysis of the Recycling coefficient

Using the neutral flux F^{o*}, where we assumed a constant S/XB=15 during the ELM-cycle we define the following ratio R^*:

$$R^* = \frac{F^{0*}}{F^i} = \frac{4\pi A \cdot 15 \cdot L^{D_\alpha}}{F^i} \tag{3.24}$$

Note that after equation 3.23 we can relate R^* to the Recycling coefficient R in the following way:

$$R^* = R\frac{15}{S/XB} \tag{3.25}$$

Figure 3.53 shows the time evolution of R^* as obtained from the conditionally-averaged fluxes F^i and F^{0*}.

We observe following features during the three ELM-cycle periods as defined before:

- **ELM-crash**: In this phase R^*sharply decreases and stays at a value of $R^* \approx 0.5$ for about 2 ms.

- **Post-ELM**: R^* increases up to a value of $R^* \approx 1$.

- **Equilibration phase**: R^*continues increasing for a few milliseconds up to a value of $R^* \approx 1.3$ and then slowly decreases towards $R^* \approx 1$, which is the pre-ELM value.

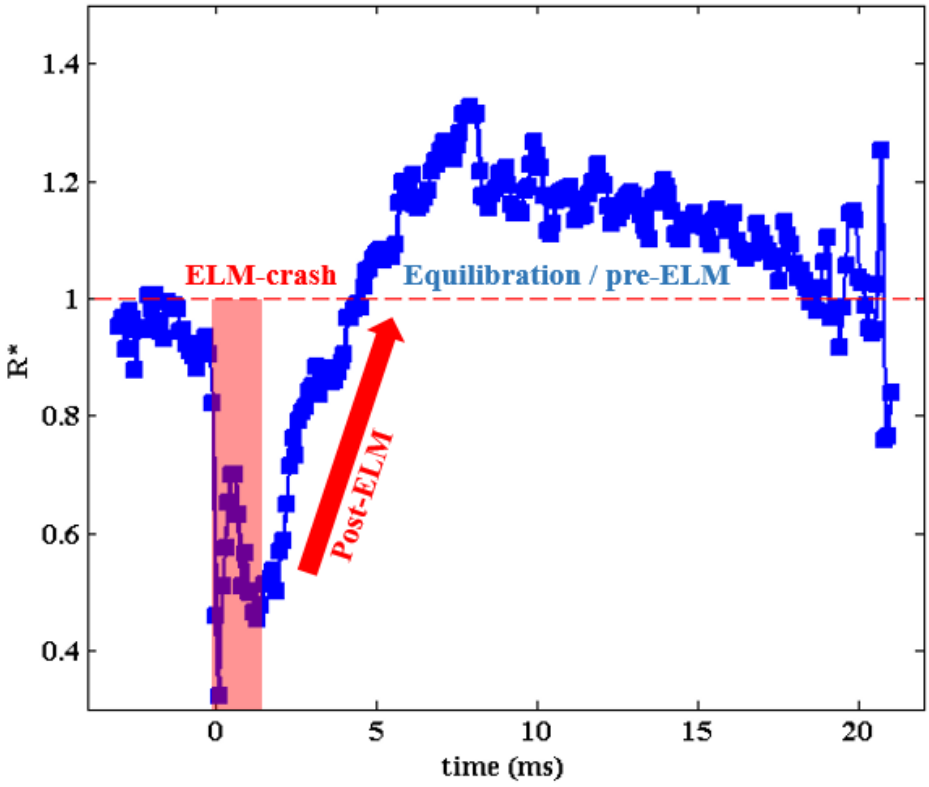

Figure 3.53 Ratio between neutral flux and ion flux. It is known as R^*.

Discussion: Possible change in the S/XB: S/XB depends on electron temperature and density, as explained before. In previous works [110] are described the changes in T_e, T_i and n_e during ELM and it is concluded that the electron temperature remains at about constant value in the SOL (higher than 5 eV so then keeping ionizing conditions). However, T_i has a localized and strong increasing at the ELM crash. On the other hand, electron density depends on ion saturation current and temperature as: $n_e = f(I_{sat}, T_e^{-0.5})$. As shown in the figure 2.54, changes in $T_e$do not lead to strong variations on the value of D/XB [218].

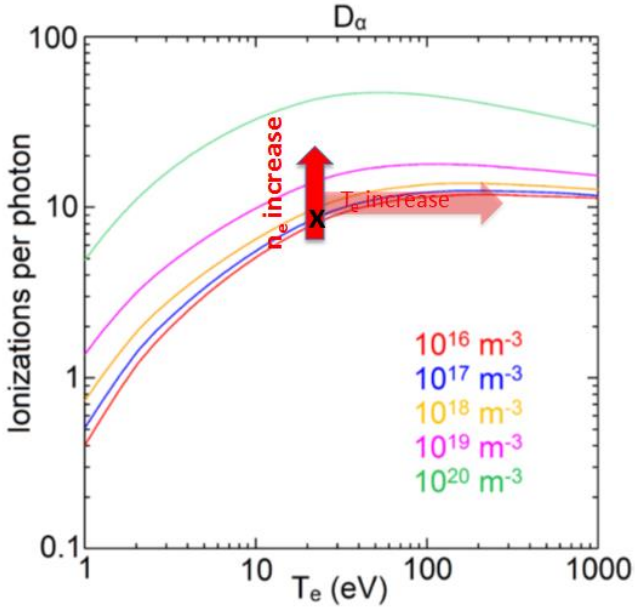

Figure 3.54 Dependence of the S/XB coefficient (number of ionizations per photon) on electron density and temperature. For $T_e > 10\ eV$ S/XB and densities of $\approx 10^{19}\ m^{-3}$does not vary significantly.

We discuss now about the value of S/XB at two different instants during the ELM due to the value of n_e:

- **ELM-crash**: Since T_i is unknown and can strongly influence I_{sat} and we cannot deduce nothing of the n_e-evolution in this period.

- **10 ms after the ELM-crash**: D/XB has a linear dependence on the electron density: $D/XB = 10 + 5n_e/(10^{19}\ m^{-3})$ [218]. In the pre-ELM phase $n_e \approx 10^{19}\ m^{-3}$, then we have that D/XB =15. On the other hand, at $t \approx 10\ ms$, the ion saturation current is of about 0.8 its value during the pre-ELM phase. Then, $n_e(10\ ms) \approx 0.8 n_e(t = 0)$. In consequence *D/XB(t=10 ms) = 14* and from equation 3.25: $R^*(t = 10\ ms) = 1.07 \cdot R$. However, in the figure 3.53.c is shown that $R^*(10\ ms) \approx 1.25$. Then, it is not possible to explain the value of R^*at this instant by a change in D/XB and, following 3.25, there are indications that R is increased of about 20 % in t = 10 ms with respect to the pre-ELM phase.

Possible variation of R during ELM: generally it is assumed that the recycling coefficient R is does not vary at short time scales as here [213]. However, in this case, during the equilibrium phase, the observed $R^* > 1$could be explained by $R > 1$ due to retarded neutral desorption from the surface.

Considerations of an evolving R basing on the Conservation of the Deuterium inventory

We have therefore obtained that in the equilibration time, R > 1, which means that in this period there is a larger neutral recycling flux than the incident ion Flux. In accordance with the model model disclosed in [213] we propose following qualitative picture of the Recycling dynamics: The ELM–cycle can be seen as schematically shown in the figure *(here $F^i = \Gamma_p$ and $F^0 = \Phi_N$).*

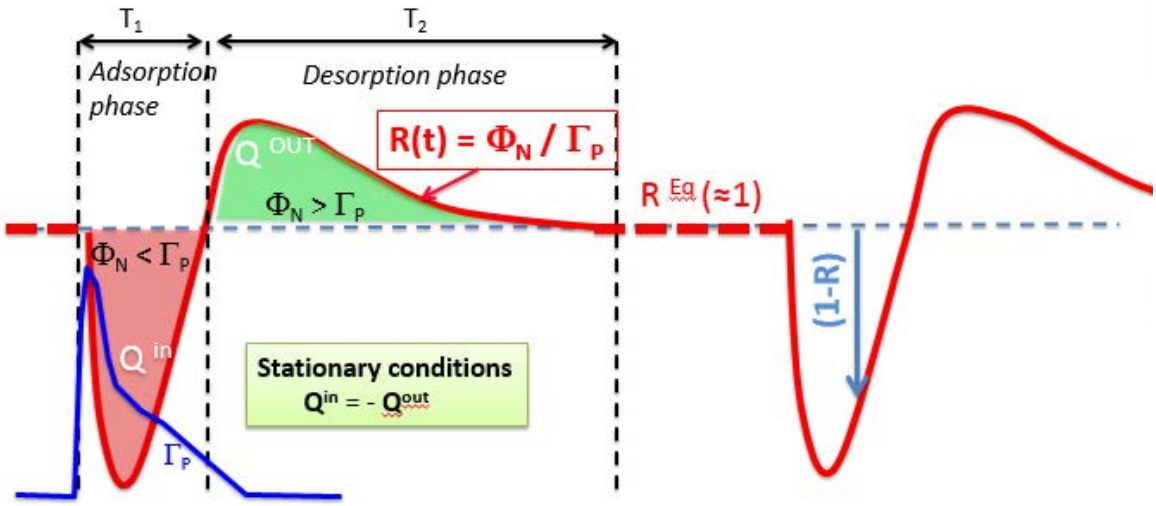

Figure 3.55 Evolution of the Recycling coefficient (red line) during ELM instability. The blue line represents the evolution of the desorbed photon flux. Courtesy of Eduardo de la Cal.

There are two main phases during the ELM: an net absorption phase where R < 1 during the ELM-crash and a posterior net desorption phase with R > 1 that corresponds to the equilibration phase that we have observed experimentally. The absorption phase would correspond to the ELM-crash and the post-ELM phase, which could not be resolved due to the uncertainties in the n_e evolution.

In stationary plasma conditions as here where $\frac{dn_e}{dt} = 0$, during one ELM cycle, the integrated absorbed neutral flux by the surface and the time-integrated fluxes of both phases should compensate.

$$Q(t) = Q^{Eq} + \int_t (\Gamma_p - \Phi_N)dt = \int_t \Gamma_p(1-R)dt \qquad (3.26)$$

where $t = T_1 + T_2$ is the duration of the ELM .

III.4.3. Conclusions

Recent results obtained in different studies in JET-ILW link the global plasma confinement to the magnetic configuration of the divertor. These studies proposed that, through the SP position, the pumping efficiency of neutrals. In the present study we suggest that the distance between the separatrix and the inner divertor (known as Clearance) could also play a role. We have observed that with a reduced Clearance a strong neutral flux is present at the upper inner divertor region after ELMs. This is attributed to the over-heating of the surface there that induces fuel outgassing. We have further demonstrated that, for the cases where the neutral fluxes are not enhanced and global confinement is highest, the divertor is under High-recycling conditions and the ion flux to the divertor target is clearly dominated by the ion flux created in the divertor SOL, without recombination. In addition, the result of the detailed analysis of the temporal evolution of Ion and Neutral fluxes during the ELM-cycle indicates that the Recycling coefficient vary within the ELM time-scale. This could be important for the understanding of the pedestal recovery cycle and thereby for the H-mode performance.

IV. GENERAL CONCLUSIONS AND OUTLOOK

This thesis contributes to the study and understanding of relevant phenomena governing and controlling transport in the plasma boundary region of stellarator and tokamak fusion plasmas.

From the perspective of plasma physics, synergies between stellarators and the main-line tokamak are particularly meaningful to address fundamental open questions like the physics of transport in the plasma boundary region. The experimental research programme reported in this thesis has been developed in Low and High-mode plasma scenarios in the TJ-II stellarator and in the JET tokamak. The most important conclusions are described below following the main research pillars of this thesis work.

Zonal Flows and turbulence control in stellarators:

Zonal Flows (ZFs) in magnetically confined plasmas manifest themselves as global coherent low frequency electrostatic fluctuation. ZFs characterization is important for a critical test of transport models in fusion plasmas.

It has been proved that is possible to identify and characterize ZFs by exploring the properties of long-range-correlations (LRCs) of low frequency electrostatic fluctuations in the TJ-II stellarator. This characterization was possible using a unique experimental set-up based on multiple electrostatic probes and edge biasing system.

A comprehensive characterization of the response of ZFs to the presence of spontaneous and biasing driven radial electric fields has been carried out in the plasma edge region of the TJ-II stellarator. Experimental findings have shown the role of neoclassical radial electric fields to control the amplitude of ZFs resulting in the development of both long (neoclassical) and short (due to ZFs) radial electric field scales. First attempt to unravel the mechanisms underlying the observed interplay between neoclassical radial electric fields and the amplification of low frequency zonal flow-like structures indices the role of Er to reduce the effective damping of zonal flows.

The development of radial electric fields with multiple radial scales involving both neoclassical and anomalous mechanisms would have direct implication in the physics understanding of transport self-regulation and model validation in fusion plasmas.

Zonal Flows during L-H transition in stellarators

Improving confidence in transport predictions for burning plasma conditions and scenario development to access improved confinement regimes is crucial for ITER and stellarator reactor development.

For the first time, the characterization of low frequency fluctuating ZFs and mean radial electric fields has been experimentally studied during the L-H transition in the in Hydrogen and Deuterium plasmas in the stellarator TJ-II. No evidence of isotope effect on the L-H transition

dynamics was observed.

These observations emphasize the critical role of both zero frequency (equilibrium) and low frequency varying large-scale flows for stabilizing turbulence during the triggering of the L-H transition in magnetically confined toroidal plasmas and show that there are different paths to reach the L-H transition with impact on the conditions to access the H-mode regime.

Radial structure of Zonal Flows in stellarators

Despite the intensive investigations on the driving and damping mechanisms of ZFs, the physics mechanisms underlying their spatial structure, which is crucially important to estimate the efficiency of the turbulent transport suppression, is not fully understood and validation studies are still missing.

We have investigated how the radial structure of low frequency Zonal Flows depends on plasma scenarios (heating and ion mass) in the TJ-II stellarator. Results reported in this thesis show, with unprecedented detail, how sensitive are the properties of zonal flows to plasma conditions, providing a key experimental guidance for model validation.

Whether this sensitivity is due to the magnitude or sign of radial neoclassical electric fields affecting Reynolds stress driven ZFs and neoclassical mechanisms or/and plasma collisionality remain an open question.

Particle transport in edge and SOL plasma at JET H-mode plasmas

Following JET-ILW recent results which conclude that the global plasma confinement is affected by the magnetic configuration of the divertor, we have studied the effect of the SP position on the dynamics of neutrals. We conclude that there are evidences of that the distance between the separatrix and the inner divertor (known as Clearance) could also play a role on the enhancement of neutral flux in the inner Divertor region after ELMs. This is attributed to the over-heating of the surface there that induces fuel outgassing. In addition, for the cases where the neutral fluxes are not enhanced and global confinement is highest, the ion flux to the divertor target is clearly dominated by the ion flux created in the divertor SOL, without recombination. This regime is known as “High-recycling regime”. Finally, the result of the detailed analysis of the temporal evolution of Ion and Neutral fluxes during the ELM-cycle indicates that the Recycling coefficient vary within the ELM time-scale. This could be important for the understanding of the pedestal recovery cycle there by H-mode performance.

The main open questions are related to the interpretation of experimental results and improving of instrumental techniques:

1) Diagnostics for Zonal Flows: The present thesis has shown the unique capabilities of Langmuir probes to identify and to characterize ZFs in fusion plasmas. In order to characterize ZF in the high temperature plasmas (like JT60-SA, W7-X) the use of other diagnostics should be addressed (like HIBP and Doppler reflectometry)

2) Physics of Zonal Flows: Whether the sensitivity of ZFs to plasma conditions reported in this thesis is due to the magnitude or/and sign of radial neoclassical electric fields affecting Reynolds stress driven ZFs and neoclassical mechanisms or/and plasma collisionality remain an open question. Further studies are needed to address this issue and validation studies are still missing.

3) Recycling studies in JET: The effort should be focused in the following lines:
   - Continue the studies on the time evolution of the Recycling during ELMs.
   - Analyze the D_α- emission and ion saturation current data used in the present work statistically in order to understand how the turbulence is affected when changing the SOL regime.

References

[1] Andrew D. Hwang (July, 9, 2018) 7.5 billion and counting-how many humans can de Earth support? From https://phys.org/news/2018-07-billion-countinghow-humans-earth.html

[2] United Nations, Department of Economic and Social Affairs (2017) : *Wordl population prospects, The 2017 Revision,* **Volume II:** https://population.un.org/wpp/Publications/Files/WPP2017_Methodology.pdf

[3] U.S. Energy Information Administration. *(*2012) *World Population Data Sheet. Energy data source:* https://www.worldpopulationbalance.org/population_energy

[4] International Energy Agency (2010): *Key World Energy Statistics*, pp. 48-57

[5] A. G. Prognos (2010): *Energieszenarien für ein Energiekonzept der Bundesregierung*, University of Koeln p. 257

[6]International Energy Agency, (2016) *Key World Energy Statistics* 2015, 2014 (2012R as in November 2015 , 2013, 2012, 2011, 2010, 2009, 2006, crude oil p.11, coal p. 13 gas p. 15

[7] UNPD, (2010. 4 November 2010) *Human Development Report* http://hdr.undp.org/sites/default/files/reports/270/hdr_2010_en_complete_reprint.pdf

[8] S. Bonjour et al, (2012) Solid Fuel use for Household Cooking, Country and Regional Estimates for 1980-2010, *Environ. Health Perspect.*

[9] M. H. Forouzanfar *et al* (2016) Global, regional, and national comparative risk assessment of 79 behavioural, environmental and occupational, and metabolic risks or clusters of risks, 1990–2015: a systematic analysis for the Global Burden of Disease Study *Lancet* **388** 1659–724

[10] M Brauer et al., (2016) Ambient air pollution Exposure Estimation for the Global Burden of Disease *Environ. Sci. Technol*, 50 (1), pp 79-88

[11] A. N. Gorban, (2013) Minimizers of all entropies and uncertainty of uncertainty, *Comput. Math. Appl*., 2013, **65**, 1438 – 1456

[12] S. Lawrence et al. (2013) Global inequality in energy consumption from 1980 to 2010, *Entropy*, **15**, 5565 – 5579.

[13] Thomas P.M. Barnett (April 22, 2004). *The Pentagon's New Map*. Putnam Publishing Group. ISBN 0-399-15175-3

[14] T. P. Wallace, (2009), *Wealth, Energy and Human Values,* ISBN: 978-1-4389-7629-7

[15] John M. Greer, (2008) *The Long Descent*, National Library of Canada, ISBN: 978-0-86571-609-4

[16] Serge Latouche (2013): "La décroissance permet de s'affranchir de l'impérialisme économique" *Reporterre, le quotidien de l 'écologie*, https://reporterre.net/La-decroissance-permet-de-s

[17] O. Ellabban et al., (2014). Renewable energy resources: Current status, future prospects and their enabling technology *Renewable and Sustainable Energy Reviews*. **39**: 748–764 [749].

[18] REN21, Global Status Report 2016.

[19] Volker Quaschning, (2013) Regenerative Energiesysteme. Technologie – Berechnung – Simulation. 8th. Edition. Hanser (Munich) , p. 49

[20] E. Lantz et al., (2012) The Past and Future Cost of Wind Energy, *National Renewable Energy Laboratory conference* paper no. 6A20-54526, page 4

[21] Willis C, et al. (2010) Bats are not birds and other problems with Sovacool's (2009) analysis of animal fatalities due to electricity generation. *Energy Policy* **38**(4), 2067-2069.

[22]California Energy Commission (2003) Potential Health and Environmental Impacts Associated With the Manufacture and Use of Photovoltaic Cells, *Public Interest Energy Research Program*

[23] M. Sanguri (2013) Negative Impacts of Hydroelectric Dams, *Bright Hub Engineering*

[24] H. Pero et al., (2013) *Fusion Engineering and Design* **88** 2 pages 70-72

[25] David P. Stern (2009) "NASA: Nuclear Binding Energy" URL: https://www-spof.gsfc.nasa.gov/stargaze/SnucEnerA-2.htm

[26] H A Bethe. (1939) Energy Production in stars *Phys. Rev.* 55.5 434-456.

[27] P. Anselmann et al., (1992) Solar neutrinos observations *Phys. Lett. B*, **285,** 376

[28] J. Sheffield, (1994) "The Physics of Magnetic fusion reactors" *Rev. Mo. Phys.* 66, 1015

[29] J. Whitlock (2010) "Section D: Safety and Liability – How does Ontario Power Generation manage tritium production in its CANDU moderators?" Canadian Nucelar FAQ

[30] H Zerriffi (2010) "Tritium: The environmental, health, budgetary, and strategic effects of the Department of Energy's decision to produce tritium" Institute for Energy and Environmental Research

[31] J. Wesson., (2004) "Tokamaks", Clarendon Press, Oxford, England,

[32] M. A. Martínez, (2016) "Análisis de iones supratérmicos en el TJ-II con una sonda luminiscente e investigación de sus mejoras instrumentales y métodos físicos" PhD thesis.

[33] J. D. Lawson et al., (1957) "Some Criteria for a Power Producing Thermonuclear Reactor" *Phys. Soc. B* **70**, 6

[34] P. A. Davidson, (2001) *An Introduction to Magnetohydrodynamics* Cambridge University Press, Cambridge, England,

[35] S.A. Sabbagh et al, (2006) "Resistive wall stabilized operation in rotating high beta NSTX plasmas" *Nucl. Fusion* **46** 635-644

[36] A. Weller et al., (2009) "High Beta Confinement in Stellarator/Heliotron" *Nucl. Fusion* **49** 065016

[37] B. D. Bondarenko (2001) "Role played by O A Lavrent'ev in the formulation of the problem and the initiation of research into controlled nuclear fusion in the USSR" *Phys. Usp.* **44** 844

[38] K. Nishikawa and M. Wakatani, (2003) "Plasma Physics: Basic Theory with Fusion Applications" Springer-Verlag Berlin Heidelberg, 3 edn

[39] N. J. Peacock (1969) "Measurement of the electron temperature by Thomson scattering in tokamak T3". *Nature*.

[40] T. Sun Pedersen et al. (2017) *Phys. Plasmas* **24** 055503

[41] J. Lyman Spitzer, (1958) "The stellarator concept" Phys. Fluids 1, 253-264

[42] P. Helander (2014) "Theory of plasma confinement in non-axisymmetric magnetic fields." In: *Reports on progress in physics*. Physical Society (Great Britain) **77.8**, 087001

[43] A. H. Boozer, (2015), "Stellarator Design" *J. Plasma Phys.* **81** 515810606

[44] M. D. Kruskal , R. M. Kulsrud (1958) "Equilibrium of a Magnetically Confined Plasma in a Toroid" Phys. Fluids **1**, 265

[45] L. Spitzer (1958) "The Stellarator Concept" *Jr. Phys. Fluids* **1**, 253

[46] M Zarnstorff et al. (2001) "Physics of the Compact Advanced Stellarator NSTX" *Plasma Phys. Control Fusion* 43 A237

[47] F.S.B. Anderson et al., (1995) *Fusion Technol.* 27, 273

[48] J. Nührenberg (2010) "Development of Quasi-isodynamic Stellarators" *Plasma Phys. Control. Fusion* 52 124003

[49] F. Castejón and J. Guasp, (1988) "Microwave injection in heliac device TJ-II" *Plasma Phys. Control. Fusion* 30 907-911

[50] A. Fernández et al, (2007) Gyrotron Radiation Affected by a Controlled Modulated Reflector: High Power Experiment, *International Journal of Infrared and Millimeter Waves* **28**, 9 705-711

[51] J. Guasp, M. Liniers, (1993) "Theoretical Evaluations of Neutral Beam Injection Efficiency for the TJ-II Helical-Axis Stellarator" *Fusion technology* **24**, 3, 251

[52] E. de la Cal et al. (2001) "Plasma Boundary and SOL studies of ECH plasmasin TJ-II stellarator with diagnosed mobile poloidal limiters" *J. Nucl. Mat.* **290-293** pp: 579:583

[53] M. Clever, (2010) *Hydrogen recycling and transport in the helical divertor of TEXTOR*, pages 25 to 29 phD thesis

[54] R. W. Conn et al., (1991) "Pumped divertors and limiters for tokamaks" *Fusion Engineering and Desing,* **14** 81-97

[55] V Philipps et al (2000) “Comparison of tokamak behaviour with Tugsten and low-Z plasma facing materials” *Plasma Phys. Control. Fusion* **42** B293

[56] A. W. Leonard et al. (2014) “Edge Localized Modes in Tokamaks” Physics of Plasmas **21** 090501

[57] E. de la Cal et al. (2008) “Spatially resolved H_α emission simulation with EIRENE in TJ-II to study hydrogen atomic and molecular physics in low density, high temperature fusion edge plasmas” *Nucl. Fusion* **48** 095005

[58] P. Helander and D J Sigmar, Collisional Transport in Magnetized plasmas (Cambridge University Press) ISBN-13: 978-0521807982

[59] S.Chandrasekhar (1943) “Stochastic Problems in Physics and Atronomy” *Rev. Mod. Phys*. **15**, 1

[60] F L Hinton, R D Hazeltine (1976) “Theory of plasma transport in toroidal confinement systems.” *Rev. Mod. Phys.* **48**, 239

[61] R Balescu: *Neoclasssical Transport,* vol2 (North-Holland, Amsterdam, Netherlands 1988)

[62] Bing Liu, (2016) “Electromagnetic properties of edge turbulencein fusion plasma devices” phD thesis, pp 67-71

[63] K. Miyamoto, (2005) *Plasma Physics and Controlled Nuclear Fusion*, Springer-Verlag (2005)

[64] J. P. Freidberg, *Plasma physics and fusion energy,* Cambridge University Press (2007) ISBN 0521851076

[65] J. W. Conner and H.R. Wilson, “Survey of theories of anomalous transport”, *Plasma Phys. Control. Fusion* **36** (1994)

[66] R. H. Kraichnan: *Phys. Fluids* **10**, 1417 (1967)

[67] M. A. Rutgers,” Forced 2D turbulence: Experimental Evicence of Simultaneous Inverse Energy and Forward Enstrophy Cascades” *Phys. Rev. Lett.* **81**, 2244 (1998)

[68] U. Frisch et al., (1995) *Turbulence: The legacy of A. N. Kolmogorov* (Cambridge University Press, Cambridge)

[69] F. Ryter et al., “Experimental studies of electron transport” *Plasma Phys. Control. Fusion* **43**, A323 (2001)

[70] D. E. Newman et al., (1996) “The dynamics of marginality and self-organized criticality as a paradigm for turbulent transport”*Phys. Plasmas* **3**, 1858

[71] L. García and B.A. Carreras, (2005) “Avalanche properties in a transport model based on critical-gradientfluctuation dynamics” *Phys. Plasmas* **12**, 092305

[72] V. P. Starr, Physics of Negative Viscosity Phenomena (McGraw-Hill, New York, 1968)

[73] A. Hasegawa and M. Wakatani, (1987) “Self-organization of electrostatic turbulence in a cylindrical plasma” *Phys. Rev. Lett*. **59**, 1581

[74] P. W. Terry, (2000) “Suppression of turbulence and transport by sheared flow” *Rev. Mod. Physics,* **72** 109

[75] Mott-Smith, H. M.; Langmuir, Irving (1926). "The Theory of Collectors in Gaseous Discharges". *Phys. Rev*. **28** (4): 727–763

[76] *Block, L. P. (May 1978). "A Double Layer Review". Astrophysics and Space Science. NASA/STI. **55** (1): 59–83. Bibcode:1978Ap&SS..55...59B. doi:10.1007/bf00642580.* Retrieved *April 16,* 2013. (Harvard.edu)

[77] *Sin-Li Chen; T. Sekiguchi (1965).* "Instantaneous Direct-Display System of Plasma Parameters by Means of Triple Probe". *J. Applied Phys. **36** (8)*

[78] Tsui, H. Y. W. et al. “A new scheme for Langmuir probe measurement of transport and electron temperature fluctuations”. *Rev. Sci. Instrum*. **63,** 4608–4610 (1992)

[79] Silva, C. et al. “Fluctuation measurements using a five-pin triple probe in the Joint European Torus boundary plasma”. *Rev. Sci. Instrum.* **75**, 4314 (2004)

[80] B.Ph. van Milligen et al, (1995) “Wavelet bicoherence: A new turbulence analysis tool” *Phys. Plasmas* **2**, 8 3017

[81] S. J. Levinson et al. (1984) “R. D. Space/time statistics of the turbulence in a tokamak edge plasma”. *Nucl. Fusion* **24,** 527

[82] M. A. Pedrosa et al. (1999), “Fast movable remotely controlled Langmuir probe system". *Review of Scientic Instruments* 70.1 pp. 415{418

[83] N. Bohr, (1985). "Rydberg's discovery of the spectral laws". In Kalckar, J. *Collected works*. **10**. Amsterdam: North-Holland Publ. Cy. pp. 373–379.

[84] N. Bohr (1913). "On the Constitution of Atoms and Molecules, Part I"*Philosophical Magazine*. **26** (151): 1–24.

[85] Maurizio Giacomin, phD thesis, pp 4-6

[86] Feynman, R; Leighton, R; Sands, M. The Feynman Lectures on Physics, vol. 1, pp. 35-2 – 35 3.

[87] W. J. Chen et al., (1982) *Journal of the Physical Society of Japan,* **51** (5) 1620-1629

[88] J. E. Felten et al., (1966) *Astrophys. J.* **146** 995

[89] T. Fujimoto, (2008) *Plasma Spectroscopy*. Springer Berlin Heidelberg, Berlin, Heidelberg,

[90] A. Fridman, A. Lawrence Kennedy, (2004). *Plasma Physics and Engineering*. CRC Press. p. 560.

[91] L. C. Johnson. (1972) Approximations for collisional and radiative transition rates in atomic hydrogen. *The Astrophysical Journal*, 174:227,

[92] M. Panesi et al., (2013) “Collisional-radiative coarse-grain model for ionization in air ” *Physics of Fluids* **25**, 057101

[93] A. Bultel et al., (2006) "Collisional-radiative model in air for Earth re-entry problems" *Phys. Plasmas* **13**, 043502

[94] B. Der Van Sijde et al., (1984) "Collisional Radiative Models in Plasmas" *Contributions to Plasma Physics* **24** (5) pp 447-473

[95] M. Goto et al., (2002) "Relations between the ionization or recombination flux and the emission radiation for

hydrogen and helium in plasma" *Phys. of Plasmas,* **9** 10

[96] K. Sawada, (1994) thesis, Kyoto University,

[97] T. Fujimoto, (1979) "A Collisional-radiative model for helium and its application to a discharge plasma" *Spectrosc. Radiat. Transf* .**21**,439~197

[98] K H Behringer et al, (1987) "Spectroscopic studies of plasma-wall interaction and impurity behaviour in tokamaks" *J. Nucl. Mater.* 145-147

[99] L. Johnson et al., J. Quant. (1973) "Ionization, recombination, and population of excited levels in hydrogen plasmas " *Spectrosc. Radiat. Transfer.* **13**, 333 358

[100] J L Terry et al. (2001) "Visible imaging of turbulence in the SOL of the Alcator C-Mod tokamak" *Journal of Nuclear Materials* 290-293 pp. 757 762

[101] S J Zweben et al. (2004) "High-speed imaging of edge turbulence in NSTX" *Nucl. Fusion* **44** 04 pp. 134 153

[102] G. Kocsis et al. (2004), "A fast framing camera system for observation of acceleration and ablation of cryogenic hydrogen pellet in ASDEX Upgrade plasmas" *Review of Scientic Instruments* **75** 11 pp. 4754 4762

[103] J. A. Alonso et al. "Fast visible camera installation and operation in JET" *AIP Conference Proceedings* **988** (2008), pp. 185 188.

[104] D. Carralero et al. (2011), "Observation of Filamentary Structures on the Boundary Region of the LHD Stellarator" *Contributions to Plasma Physics* **51** 1 pp. 92-98.

[105] E. de la Cal et al. (2011) "The Visible Intensied Cameras for Plasma Imaging in the TJII Stellarator" *Contrib. Plasma Phys.* **51** 8 742753.

[106] J.A. Alonso et al. (2009) "Fast visible imaging of ELM-wall interactions on JET" *J. Nucl. Mat.* 390-391 797800

[107] J. H. Yu et al. (2013) "Visible imaging and spectroscopy of disrupti in DIII-D". *Phy. of Plasmas* **20** 4 042113.

[108] E. Gauthier et al., (2007) *Fusion Engineering and Design* **82** 1335 - 1340

[109] E De La Cal et al. "The Visible Intensied Fast Camera with wide-angle view ofJET ILW experiment". In: *39th EPS Conference on Plasma Physics 16th International Congress on Plasma Physics.* **31** 124. 8. 2012.

[110] F. Guillemaut et al., (2015) "Ion target impact energy during type I edge localized modes in JET ITER-like wall" *Plasma Phys. Control. Fusion* **57** 085006

[111]D Tskhakaya et al (2011) "Interpretation of divertor Langmuir probe measurements during the ELMs at JET" *J. Nucl. Mater*. 415 S860–4

[112] U. Losada et al. (2016) "Influence of long-scale length radial electric field components on zonal flow-like structures in the TJ-II stellarator" *Plasma Phys. Control. Fusion* **58** 084005

[113] T. S. Hahm et al., (2000) "Zonal Flow Concept I" *Plasma Phys. Control. Fusion* **42** A205

[114] A Fujisawa et al. (2009) "A review of Zonal Flow experiemnts" *Nucl. Fusion* **49** 013001

[115] A. Fujisawa et al*.,* (2004) "Identification of Zonal Flows in a toroidal plasma " *Phys. Rev. Lett.* **93** 165002

[116] G. R. Tynan et al., (2001) "Radially sheared azimuthal flows and turbulent transport in a cylindrical plasma" *Phys. Plasmas* **8** 2691

[117] R. A. Moyer et al., (2001) "Increased Nonlinear Coupling between Turbulent and Low-Frequency Fluctuations at the L-H Transition" *Phys. Rev. Lett.* **87** 135001

[118] S. Coda et al., (2001) "Signature of Turbulent Zonal Flows Observed in the DIII-D Tokamak" *Phys. Rev. Lett.* **86** 4835

[119] G. S. Xu et al., (2003) "Direct Measurement of Poloidal Long-Wavelength ExB Flows in the HT-7 Tokamak" *Phys. Rev. Lett*. **91** 125001

[120] A. Bencze et al., (2006) "Observation of Zonal Flow-like structures using the autocorrelation-width technique" *Plasma Phys. Control. Fusion* **48** S137

[121] V. Sokolov et al., (2006) "Observation and Identification of Zonalf Flows in a basic physics experiment" *Plasma Phys. Control. Fusion* **48** S111

[122] C. Hidalgo et al., (1993) "Experimental evidence of three-wave caoupling on plasma turbulence" Phys. Rev. Lett **71** 3127

[123] B. Gonçalves et al., (2006) "Role of Turbulence on Edge Momentum Redistribution in the TJ-II stellarator" *Phys. Rev. Lett.* **96** 145001

[124] C. Hidalgo et al., (2003) "Experimental Investigation of Dynamical Coupling between Turbulent Transport and parallel Flows in the JET plasma Boundary Region" *Phys. Rev. Lett.* **91** 065001

[125] G.S. Xu et al (2009) "Blob/Hole formation and Zonal Flow generation in the edge of the JET tokamak" *Nucl. Fusion* **49** 092002

[126] M A Pedrosa et al. (2008) "Evidence of Long Distance Correlation of Fluctuations during Edge transitions to Improved-Confinement regimes in the TJ-II stellarator" *Phys. Rev. Lett.* **100** 215003

[127] C Silva et al. (2011) "Coupling between long-rage correlations and radial transport in the TJ-II boundary plasma" *Nucl. Fusion* **51** 063025

[128] J A Alonso et al. (2013) "Dynamics of Zonal Flow structures in the edge of the TJ-Ii stellarator" *Plasma Phys. Control. Fusion* **55** 014001

[129] J A Alonso et al. (2012) "Dynamic transport regulation by Zonal Flow-like structures in the TJ-II stellarator" *Nucl. Fusion* **52** 063010

[130] C Hidalgo IAEA (2015) "Progress regarding magnetic confinement experiments, plasma-materials interactions and plasma performance" *Nucl. Fusion* **55** 104025

[131] Y Xu et al. (2009) "Long distance correlation and Zonal Flow structures induced by mean ExB shear flows in the biasing H-mode at TEXTOR" *Phys. Plasmas* **16** 110704

[132] J A Alonso et al. (2012) *Nucl. Fusion* **52** 063010

[133] C Hidalgo IAEA (2015) *Nucl. Fusion* **55** 104025

[134] P Helander et al. (2008) "Intrinsic ambipolarity and rotation in stellarators" *Phys. Rev. Lett.* **101** 145003

[135] G Dif-Pradalier et al. (2015) "Finding the elusive ExB Staircase in Magnetized Plasmas" *Phys. Rev. Lett.* **114** 085004

[136] J C Hillesheim et al. (2016) "Stationary Zonal Flows during the formation of the Edge Transport Barrier in the JET tokamak" *Phys. Rev. Lett.* **116** 065002

[137] T Watanabe et al. (2008) "Reduction of turbulent transport with Zonal Flows Enhanced in Helical Systems" *Phys. Rev. Lett.* **100** 195002

[138] J L Velasco et al. (2012) "Vanishing Neoclassical Viscosity and Physics of the Shear Layer in Stellarators" *Phys. Rev. Lett.* **109** 135003

[139] A Mishchenko and R Kleiber (2012) "Zonal Flows in stellrators in an ambient radial electric field" *Phys. Plasmas* **19** 072316

[140] E Sánchez et al. (2014) *41st EPS,*-Conference on Plasma Physics, Berlin, Germany,, **P2.079**

[141] H. Lamela et al., (2001) "Laser interferometric experiments for the TJ-II stellarator electron-density measurements" Review of Scientific Instruments **72**, 96

[142] S. P. Hirshman and Whitson J.C. (1983) "Steepest-descent moment method for three-dimensional magnetohydrodynamic equilibria" *Phys. Fluids* **26** 3553–68

[143] Adriana M. de Aguilera et al., (2015) "Magnetic well scan and confinement in the TJ-II stellarator" *Nucl. Fusion* **55** 113014 (10pp)

[144] B. Ph. van Milligen et al., (2011) "MHD mode activity and the velocity shear layer at the TJ-II"*Nucl. Fusion* **52** 013006

[145] P. Ch. Ritz et al., (1990) "Evidence for Confimenement improvement by velocity shear suppression of edge turbulence" *Phys. Rev. Lett.* **20** 2543

[146] C. Hidalgo et al., (2004) "Experimental evidence of coupling between sheared-flow development and an increase in the level of turbulence in the TJ-II stellarator" *Phys. Rev. E* **70** 067402

[147] A. P. Witkin, "Scale-space filttering", *Proc. 8th Int. Joint Conf. Art. Intell.,* 1019-1022, Karlsruhe, West Germany (1983)

[148] T. Lindeberg, (1994) "Space-scale theory: a basic tool for analyzing structures at different spatial scales" *Journal of Applied Statistics* **21** 2 pp: 225-270

[149] B. Ph. Van Milligen et al. (2011) "Integrated data analysis at TJ-II: The density profile" *Rev. Sci. Instrum*. **82** 073503

[150] J. L. Velasco et al., (2012) *Phys. Rev. Lett.* **109** 135003

[151] B. Carreras et al., (1998) *Phys. Rev. Lett.* **80** 4439

[152] K. Itoh et al., Transport and Structural Formation in Plasmas (Bristol: IOP Publishing) (1999)

[153] H. Biglari et al., (1990) "Theory of mean poloidal flow generation by turbulence" *Phys. Fluids* **B21** 2–4

[154] P. Helander et al., (2002)Collisional Transport in Magnetized Plasmasvol 87 (Cambridge: Cambridge University Press)

[155] M. Wakatani, (1998) Stellarator and Heliotron Devices(Oxford: Oxford University Press)

[156] P. H. Diamond et al., (1994) "Self-regulating Shear Flow Turbulence: A paradigm for the L to H transition" Phys. Rev. Lett.**72** 2565

[157] Lotka, A. J. (1910). "Contribution to the Theory of Periodic Reaction". *J. Phys. Chem.* **14**(3): 271-274.

[158] H. L. Pécseli et al., (1989) *Phys. Fluids* **1** 1616

[159] Grulke et al., (2001) "Radially ppropagating fluctuating structures in the Scrape-off Layer of Alcator C-Mod " *Phys. Plasmas* **8** 12

[160] C. Silva et al., (2005) 32 EPS Conference on Plasma Physics, Tarragona, 2005: ECA Vol. 29C p-2037

[161] U. Losada et al., (2016) 43rd EPS Conference on Plasma Physics, P1.007

[162] A. Dinklage et al. (2013) "Inter-machine validation study of neoclassical transport modelling in medium – to high-density stellarator-heliotron plasmas" *Nucl. Fusion* **53** 063022

[163] R. Gerrú et al., (2019) "On the interplay between turbulent forces and neoclassical particle losses in Zonal Flow dynamics" to be submitted

[164] B. Schmid et al (2017) "Spatio-temporal structure of turbulent Reynolds stress zonal flow drive in 3D magnetic configuration" *New J. Phys.* 19 055003

[165] U Losada *et al* (2018) "Role of isotope mass and evidence of fluctuating Zonal Flows during the L-H transition in the TJ-II stellarator" *Plasma Phys. Control. Fusion* **60** 074002

[166] K. H. Burrell et al., (1997) "Effects of ExB velocity shear and magnetic shear on turbulence and transport in magnetic confinement devices "*Phys. Plasma* **4** 1499

[167] F. Wagner et al., (1982) "Regime of Improved Confinement and High Beta in Neutral-Beam-Heated Divertor Discharges for ASDEX Tokamal" *Phys. Rev. Lett.* **49** 1408

[168] K. Kamiya et al., (2016) "Experimental validation of non-uniformity effect of the radial electric field on the edge transport barrier formation in the JT-60 UH-mode plasmas" *Sci. Rep.* **6** 30585

[169] F. Ryter et al., (2013) "Survey of the H-moe power threshold and transition physics studies in ASDEX Upgrade" *Nucl. Fusion* **53** 113003

[170] I. Cziegler et al., (2014) "Zonal flow production in the L-H transition in ALcator C-mode" *Plasma Phys. Control. Fusion* **56** 075013

[171] P. Manz et al., (2012) "Zonal Flow triggers the L-H transition in the Experimental Advanced Superconducting Tokamak" *Phys. Plasmas* **19** 072311

[172] G. S. Xu et al., (2011) *Phys. Rev. Lett.* **10** 7125001

[173] G. S. Xu et al., (2012) "First observation of a new zonal-flow cycle state in the H-mode transport barrier of the experimental advanced superconducting Tokamak" *Phys. Plasmas* **19** 122502

[174] T. Estrada et al., (2011) "Spatiotemporal Structure of the Interaction between Turbulence and Flows at the L-H transition in a toroidal plasma" *Phys. Rev.Lett.* **107** 245004

[175] H. G. Shen et al., (2016) "Observation of zonal flows in elecrode biasing experiments on the Joint Texas Experimental Tomakamak" *Phys. Plasmas* **23** 042305

[176] J. Cheng et al., (2013) "Dynamics of the Low-Intermediate-High Confinement Transitionsin Toroidal Plasmas" *Phys. Rev. Lett*. **110** 265002

[177] E. J. Kim et al., (2003) *Phys. Rev. Lett* .**90** 185006

[178] E. Viezzer et al., (2013) "High-accuracy characterization of the edge radial electric field at ASDEX upgrade " *Nucl. Fusion* **53** 053005

[179] F. Wagner et al., (2006) "H-mode and transport barriers in helical systems" *Plasma Phys. Control. Fusion* **48** A217

[180] M. Hirsch et al*.,* (2008) "Major results from the stellarator W7-X" *Plasma Phys. Control. Fusion* **50** 053001

[181] T. Estrada et al., (2009) "Sheared flows and transition to improved confinement regime in the TJ-II stellarator" *Plasma Phys. Control. Fusion* **51** 124015

[182] C. Hidalgo et al., (2009) "Multi-scale mechanisms and spontaneous edge transport bifurcations in fusion plasmas" *Europhys. Lett*. **87** 55002

[183] U Stroth et al. (1998) "A comparative study of transport in stellarators and tokamaks" *Plasma Phys. Control. Fusion* **40** 9

[184] F. Ryter et al., (2013) *Nucl. Fusion* **53** 113003

[185] C. F. Maggi et al., (2018) "Isotope effects on L-H threshold and confinement in tokamak plasmas" *Plasma Phys. Control. Fusion* **60** 014045

[186] T. Happel et al., (2009) "Doppler reflectometer system in the TJ-II stellarator" *Rev. Sci. Instrum*. **80** 073502

[187] J. Herranz et al., (2003) *Fusion Eng. Des*. **65** 525

[188] Rabiner, Lawrence R., Theory and Application of Digital Signal Processing NJ: Prentice-Hall, 1975.

[189] T. Estrada et al., (2010) *Contrib. Plasma Phys.* **50** No. 6-7 501-506

[190] F. Castejón et al., (2017) "3D effects on transport and plasma control in the TJ-II stellarator" *Nucl. Fusion* **57** 102022

[191] P. H. Diamond et al., (2000) *Phys Rev Lett.* May 22;84(21):4842-5

[192] B.Ph. van Milligen *et al* (2011) "MHD activity and velocity shear layer in the TJ-II stellarator" *Nucl. Fusion* **52** 013006

[193] E. J. Powers et al., (1974) "Spectral techniques for experimental investigation of plasma diffusion due to polychromatic fluctuations" *Nucl. Fusion* **14** 749

[194] B. A. Carreras et al (1993) " Effect of a poloidal shear flow on the probability of accessing the multiple saturated states in the resistive interchange instability" *Phys. Fluids* B **5** 1795

[195] A. V. Melnikov *et al* (2013) " Changes in plasma potential and turbulent particle flux in the core plasma measured by heavy ion beam probe during L-H transitions in the TJ-II stellarator" *Nucl. Fusion* **53** 092002

[196] T. Kobayashi et al. (2019) "*Frequency and plasma condition dependent spatial structure of low frequency global potential oscillations in TJ-II stellarator*" Nuclear Fusion (Accepted, in Press) https://doi.org/10.1088/1741-4326/ab0122

[197] M. Nakata et al., (2017) "Isotope effects on Trapped-Electron-Mode driven Turbulence and Zonal Flows in Helical and Tokamak Plasmas" *Phys. Rev. Lett.* **118** 165002

[198] Y Xu et al., (2013) "Isotope Effect and Multiscale Physics in Fusion Plasmas " *Phys. Rev. Lett.* **110** 265005

[199] B. Liu *et al.,* (2015) "Isotope effect physics, turbulence and long-range correlation studies in the TJ-II sttellarator" *Nucl. Fusion* **55** 112002

[200] B. Liu et al., (2016) "Multi-scale study of the isotope effect in ISTOKK" *Nucl. Fusion* **56** 056012

[201] F. Romanelli on behalf of JET Contributors (2015) "Overview of the JET results" *Nucl. Fusion* **55** 104001

[202] G. F. Matthews et al, (2014) "The second phase of JET operation with the ITER-like wall" *Phys. Scr.* 014015

[203] X. Litaudon et al, (2017) "Overview of the JET results in support to ITER" *Nucl. Fusion* **57** 102001

[204] S. Brezinsek et al (2013) "Fuel retention studies with the ITER-like Wall in JET" *Nucl. Fusion* **53** 083023

[205] E. de la Luna et al, (2014) " Comparative Study of High Triangularity H-Mode Plasma Performance in JET with Be/W Wall and CFC Wall" IAEA FEC

[206] E. Joffrin et al, (2014) "Impact of Divertor Geometry on ITER Scenarios Performance in the JET Metallic Wall" IAEA FEC

[207] P. Tamain et al, (2015) "Investigation of the influence of the divertor recycling on global plasma confinement in JET ITER-like wall" *J. of Nucl. Mat.* **463** 450–454

[208] S. Brenzisek et al, (2016) "Quantification of tunsgten sputtering at W/C twin limiters in TEXTOR with the aid of local WF6 injection" *Phys. Scr. T* **145** 014016

[209] D. M. Harting et al, (2015) "Intra-ELM phase modelling o f a JET ITER-like wall H-mode discharge with EDGE2-EIRENE" *J. Nucl. Mat.* **463** 493

[210] S. Wiessen et al (2017) "Impact of the JET ITER-like wall on H-mode plasma fueling" *Nucl. Fusion* 57 066024

[211] C. Guillemaut et al (2018) "Experimental validation of an analytical kinetic model for edge-localized modes in JET-ITER-like wall" *Nucl. Fusion* **58** 066006

[212] E. de la Cal et al (2015) "Edge localised model-like instability driven plasma edge burst study in the TJ-II stellarator" *Plasma Phys. Control. Fusion* **57** 075001

[213] K Schmid et al., (2016) "Diffusion-trapping modelling of hydrogen recycling in tungsten under ELM-like heat loads" *Phys. Scr*. T167 014025

[214] M. Mayer et al, (2016) "Erosion and deposition in the JET divertor during ILW campaign" *Phys. Scr.* T167 014051

[215] A. Loarte et al. (1998) "Plasma detachment in JET Mark I divertor experiments" *Nucl. Fusion* **38** 331

[216] E. de la Cal et al. (2019) "On the relation of neutral fluxes and Divertor configuration in JET-like-wall H-mode plasmas " *Nuclear Fusion (to be published)*

[217] D. Alegre et al. (2017) "A parametric study of helium retentionin beryllium and its effect on deuterium retention" *Physica Scripta,* **T170** 014028

[218] H. P. Summers (2007), Atomic Data and Analysis Structure: users manual URL http://www.adas.ac.uk/man/contents.pdf